Modelling and Control of Silicon and Germanium Thin Film Chemical Vapor Deposition

by

Scott Anderson Middlebrooks

A dissertation submitted in partial fulfillment

of the requirements for the degree of

Doctor of Philosophy

(Chemical Engineering)

at the

UNIVERSITY OF WISCONSIN–MADISON

2001

To Hubert Middlebrooks, for letting me take things apart.

Acknowledgments

Well, I just had breakfast at Lane's bakery for probably the last time this morning and fond memories of my graduate career began to surface. So, I decided that I had better come straight to the office and acknowledge all those that have influenced my Ph.D. experience, before the recollections become fuzzy. I hope that I do not forget anyone.

First, I would like to acknowledge my thesis advisor, James B. Rawlings. His ability to understand large problems and distill them down to the essential components is uncanny. Dr. Rawlings raised the bar high. He gave me freedom to pursue any crazy idea that I had but held me completely accountable and I am a better engineer for it. Dr. Rawlings said that the value of a Ph.D. is the path that one takes and not the end result. I must agree and I am eternally grateful for having worked under his tutelage.

Next, I would like the thank the members of my academic committee, Paul Nealey, Nicholas Abbott, Thad Walker, and Thomas Kuech, for their time and effort in evaluating my work.

I consider myself fortunate that I was involved in a collaborative research effort with the University of Texas at Austin. Thus, I spent a great deal of time in Austin during my graduate career. At Texas I owe thanks to John Ekerdt for his excellent managerial skills and his unfailing confidence that we would eventually close this damn loop. I also owe thanks to Michael Downer for the many discussions on optics and for his unparalleled patience. I am also indebted to Sanjay Banerjee for giving me time on his chemical vapor deposition reactor and for teaching me a great deal about device physics and manufacturing.

I also need to acknowledge the many graduate students at Texas that helped me with the reactor. First, I would like to thank Soji John and Ed Quinones for showing me the ropes and for helping me adjust to working in a clean room environment. I owe a *huge* debt of gratitude to Lucymarie Mantese, Jiang Yingying, David Onsongo, and Sankaran Jayanarayanan. These saints installed the optics, cleaned and loaded the wafers, maintained the reactor, and watched patiently with me as I ruined wafer after wafer, until we got the controller to work. The experimental results in this dissertation are just as much a product of their efforts as of mine.

Next, I need to acknowledge the Rawlings' group. In addition to being an excellent advisor, Dr. Rawlings also selected and maintained an eclectic research group full of dynamic personalities. Interactions with the Rawlings' group comprises most of the fond memories of my graduate experience.

Let me begin by acknowledging Scott Meadows, Tony Mullins, Ken Muske and John Eaton. Tony was always up for a heated political discussion and always proved to be an instant and mobile integral table. I enjoyed the short time that I worked with Ken and Scott and I must also thank Ken for not punching me in the face when I interrupted his thesis writing to ask him how to save my data in Octave. I must thank John Eaton for answering all my naive computer questions and for providing me with a Makefile to generate this dissertation.

Next I want to thank John Campbell and Rock Matthews. The first day that I arrived in Austin, John came over and helped me unload the moving van. He then brought me over to his house where he and his wife Vicki cooked me dinner. John, I will never forget this and a rare day went by when *you* couldn't make me laugh. Rock, I must thank you for teaching me what integrity is and for pretty much teaching me how to ski.

I want to next acknowledge Rahul Bindlish. In addition to being a good-hearted man, Rahul is also an excellent engineer. I am amazed at Rahul's ability to essentially freeze time and be as methodical as death when it comes to debugging computer programs. Whenever I had a pesky bug I could always count on Rahul to help me find it. Rahul, rebuilding the 470 control lab with you was pure joy.

I also need to acknowledge Daniel Patience and Chris Rao. Thanks Dan for all the beers and for teaching me how to play cricket. I still don't see the difference between it and baseball. Chris, you are a good friend and I owe you thanks for proving emphatically to me that natural gas is indeed flammable.

I must also acknowledge the other members of the group, Jenny Wang, Matt Tenny, Bryan Odelson, Eric Haseltine, Sankash Venkatesh, and Gabriele Pannocchia. Jenny, I have a feeling that I will see you at microelectronics conferences soon. Thanks to Matt, Bryan, Eric and Gabriele for all the dart games.

Lastly, I must thank friends and family who made the last 7 or so years enjoyable. Thanks to Don and Joan McConley for all the dinners that you had me over for and for all the intense Cribbage games that we played. Thanks to Mom, Dad, Tommie, Kirsten, Clint, Charlie, Patricia, and Urban, for all the support and encouragement as well as rides to and from airports. I conclude by acknowledging Jill Myers. Your love, guidance, support, and smiling face has made the last year wonderful.

SCOTT ANDERSON MIDDLEBROOKS

University of Wisconsin–Madison
February 2001
A Scottaye Odyssey

Modelling and Control of Silicon and Germanium Thin Film Chemical Vapor Deposition

Scott Anderson Middlebrooks
Under the supervision of Professor James B. Rawlings
At the University of Wisconsin–Madison

This study integrates *in situ* robust and efficient fundamental models and non-invasive optical sensors with state-of-the-art estimation and model predictive control techniques in order to grow unusual and aggressive $Si_{1-x}Ge_x$ alloy films.

Fundamental kinetic models are developed that describe the complicated behavior of the silicon/germanium deposition system. The kinetic models are incorporated into material balances yielding a physical model of the film growth rate as a function of reactor environment variables. The model is validated by comparison to experimental data.

An on–line spectral ellipsometer is installed on the deposition reactor and a dynamic sensor model that characterizes the optical properties of the growing film is presented. The sensor model is integrated with the kinetic and process models that describe the reactor and predicts the ellipsometric parameters Ψ and Δ during film growth.

An extended Kalman filter is developed that utilizes the process model and the sensor model and estimates uncertain system states given ellipsometric measurements. Application of state estimation theory to spectroscopic ellipsometry is a new contribution of this research. The filter provides state estimates of film growth rate and composition in real time. These measurements are utilized to update the optimization problem solved by the regulator.

A model predictive controller is presented that regulates the various reactor variables, such as precursor gas flow rates, substrate temperature, and reactor pressure, in order to grow an aggressive $Si_{1-x}Ge_x$ alloy film with precise control over film growth rate and composition. Feedback from the optical sensors rejects unmeasured disturbances and eliminates run–to–run variability allowing for precise control over the film qualities and for the fabrication of novel devices with exact specifications.

The model predictive controller is tested by growing aggressive $\mathrm{Si}_{1-x}\mathrm{Ge}_x$ alloy composition profiles in which flow rates of several component gases and the reactor temperature are varied simultaneously in order to achieve the profile of interest. The experimental results presented in this work provide the first demonstration of feedback control using online optical film measurements to grow aggressive alloy composition profiles in which flow rates of several component gases and reactor temperature must be varied simultaneously in order to achieve the profile of interest.

The films grown utilizing feedback from the optical sensor are compared to the films grown using open–loop recipes, which is the current industrial practice. These films are compared quantitatively utilizing off-line characterization techniques, such as auger spectrometry and secondary–ion–mass–spectrometry (SIMS) analysis.

Contents

List of Tables

List of Figures

Chapter 1

Introduction

> *A whole is that which has a beginning, middle, and end.*
>
> — Aristotle

Judging from the number of beeps, whistles, and "La Cucoracha"s, heard in restaurants and theaters, mobile communication devices are ubiquitous in today's electronic market. As technology advances these devices require higher speed, higher packing density, less power consumption, and lower cost. Recently, a new $\mathrm{Si}_{1-x}\mathrm{Ge}_x$ heterojunction technology has emerged that greatly enhances silicon device performance without increasing the cost tremendously. The heteroepitaxial growth of strained $\mathrm{Si}_{1-x}\mathrm{Ge}_x$ on Si(100) substrates permits bandgap engineering, which allows for tailored, high-performance devices. In addition, $\mathrm{Si}_{1-x}\mathrm{Ge}_x$ heterojunction technology can be integrated with existing silicon technology rather than replacing it [12]. In heterojunction bipolar transistors(HBTs), the presence of germanium exponentially alters the device characteristics(e.g., the collector current). It is also possible to obtain $\mathrm{Si}_{1-x}\mathrm{Ge}_x$ channel metal-oxide-semiconductor field effect transistors(MOSFETs), which is displayed in Figure 1.1, that have larger hole surface mobilities than bulk Si thus minimizing asymmetry in complementary metal-oxide-semiconductor(CMOS) devices [95].

An integrated circuit consists of several layers of meticulously patterned thin films, each chemically altered to achieve the desired electrical characteristics. These devices are manufactured through a series of physical and chemical batch operations. The unit operations can be divided into four classes: bulk crystal growth, thin film deposition, which includes chemical vapor deposition, patterning, which includes lithography and etch, and dopant incorporation(doping).

Chemical vapor deposition(CVD) is a process whereby precursor gases react on the surface of a substrate to deposit a thin solid film [33, 65, 66, 67, 81, 100, 105].

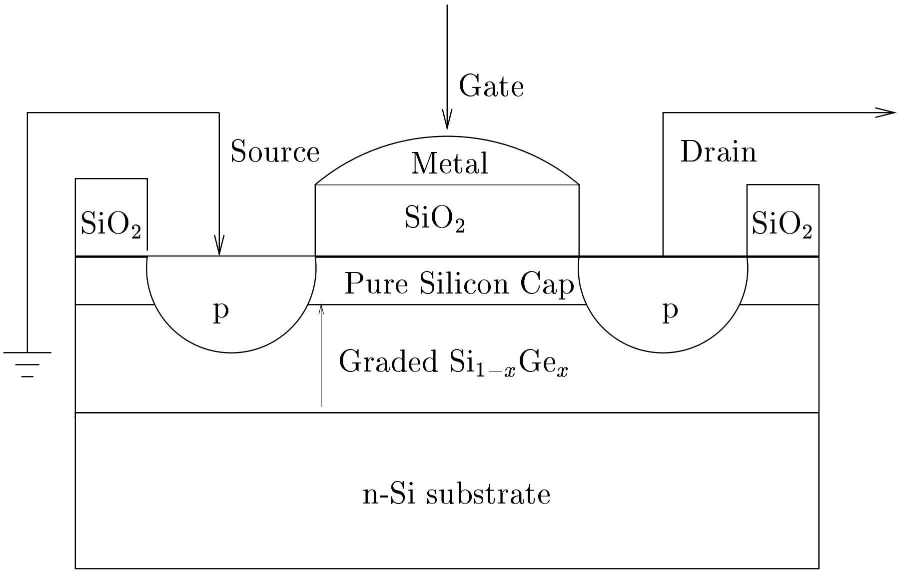

Figure 1.1: p-type metal-oxide-semiconductor field effect transistor(p-MOSFET)

CVD is among the most widely used film growth methods in the microelectronics industry. By CVD, Si and Ge can be deposited as alloy layers from a few hundred angstroms thick up to several microns thick. Trace amounts of dopants can also be added to the film during deposition to modify the electrical properties of the layer. The composition and thickness of the layer must be controlled precisely to achieve the desired electrical device properties.

The current industrial practice used to manufacture $Si_{1-x}Ge_x$ films is to follow an empirical recipe. The recipe is generated off–line based on past experience and trial and error. The complexity of the composition profiles required for bandgap engineering makes this approach intractable.

Another manufacturing approach is to follow a recipe that is generated with a fundamental model. A first–principles model is much more flexible than an empirical model and is able to represent the arbitrary complexity in components and alloy profiles. With this method, which is referred to as open–loop control, there is no feedback.

The technical challenge of this study is to grow $Si_{1-x}Ge_x$ alloy films with precise control over film thickness, germanium composition, and film uniformity. This study integrates *in situ* robust and efficient fundamental models and non-invasive optical sensors with state-of-the-art estimation and model predictive control techniques in order to grow unusual and aggressive $Si_{1-x}Ge_x$ alloy films. The model predictive controller presented in this work utilizes feedback from the optical sensors and the dynamic process model to reconstruct the current state of the growing film in real time. Feedback from the optical sensors rejects unmeasured disturbances and eliminates run–to–run variability allowing for precise control over the film qualities and for the fabrication of novel devices with exact specifications.

1.1 Dissertation overview

The model–predictive control algorithm used in this study to control $\mathrm{Si}_{1-x}\mathrm{Ge}_x$ thin film chemical vapor deposition is shown in Figure 1.2. The chapters that describe each of the major blocks in the algorithm are summarized below.

Chapter 3 describes the ultra–high vacuum chemical vapor deposition growth chamber used in this study. The reactor is basically a stainless–steel chamber that is pumped down to very low pressures. The growth chamber is equipped with a two–zone, boron–nitride substrate heater. Mass flow controllers (MFCs) regulate the flow of the precursor gases disilane and germane into the reactor. A variable conductance valve connected between the growth chamber and the downstream pumps maintains constant pressure in the growth chamber. On–line process measurements are provided by an *in situ* high-speed spectral ellipsometer that observes and characterizes optical properties at the growing film interface.

Chapter 4 describes the formulation of a first–principles model that quantitatively represents $\mathrm{Si}_{1-x}\mathrm{Ge}_x$ chemical vapor deposition. Fundamental kinetic models are developed that describe the complicated behavior of the silicon/germanium deposition system. The kinetic models are incorporated into material balances yielding a physical model of the film growth rate as a function of reactor environment variables. A dynamic model of the ellipsometric sensor, which characterizes the optical properties of the growing film, is also presented. The ordinary differential equations(ODEs) describing the process model and the optical model are then characterized succinctly in state-space form. The state-space model is numerically integrated and the validation results are compared with experimental data.

Solving the estimation problem is the key step in the control of $\mathrm{Si}_{1-x}\mathrm{Ge}_x$ chemical vapor deposition as film composition and growth rate cannot be measured directly. They must be inferred from optical measurements. Chapter 5 presents the extended Kalman filter estimation algorithm that infers the system states by balancing the contribution made by the dynamic process model with that given by the optical measurement. The filter counteracts the effects of measurement noise and provides a smooth estimate of the system states in real time.

The feedback controller presented in this work performs two separate functions,

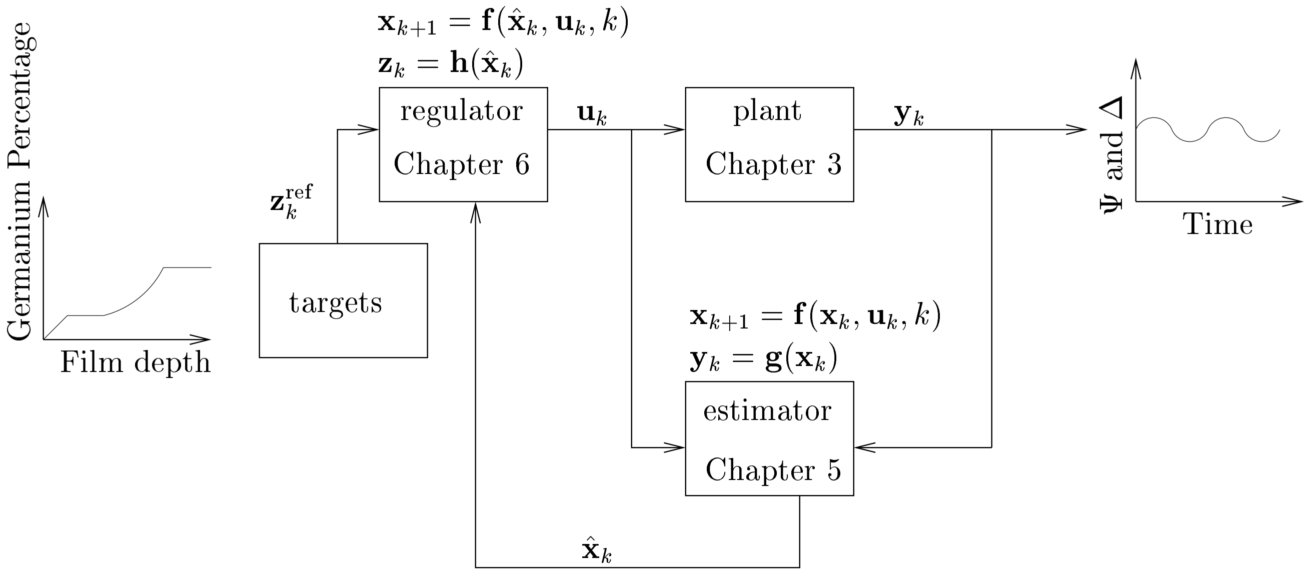

Figure 1.2: Regulation and estimation functions of the controller

one of which is estimating the current value of system states. The other function is regulation. It is the task of the regulator to drive the best estimate of the film and reactor state to desired targets. Chapter 6 presents a model predictive controller that regulates the various reactor variables, such as precursor gas flow rates, substrate temperature, and reactor pressure, in order to grow a $\mathrm{Si}_{1-x}\mathrm{Ge}_x$ alloy film with precise control over film growth rate and composition.

The model predictive controller is tested by growing aggressive $\mathrm{Si}_{1-x}\mathrm{Ge}_x$ alloy composition profiles in which flow rates of several component gases and the reactor temperature are varied simultaneously in order to achieve the profile of interest. In Chapter 7 the films grown utilizing feedback from the optical sensor are compared to the films grown using open–loop recipes.

Chapter 8 summarizes the estimation and control results of this study and presents a general design procedure that may be useful for future work.

Chapter 2

Review of Previous Work

To what purpose is this waste?

— Matthew 26:8

2.1 Chemical Vapor Deposition for Epitaxial Film Growth

Various techniques have been used to grow $Si_{1-x}Ge_x$ epilayers, including molecular beam epitaxy (MBE)[15, 51, 58, 63, 71] and chemical vapor deposition (CVD)[50, 65, 66, 67, 68]. MBE is a physical deposition method where a source emits atoms to a substrate at which point the adatoms form a physical bond. In the case of $Si_{1-x}Ge_x$ deposition, separate sources are used to supply Si and Ge to the substrate surface. The flux of each species as well as wafer temperature control the resulting mole fraction of germanium incorporated into the epitaxial film. MBE reactors are generally considered research tools and are not as commercially relevant as chemical vapor deposition reactors.

Chemical vapor deposition techniques are widely used in manufacturing because of their relative simplicity. CVD is a process where precursor gases react on the surface of a substrate to form an epitaxial film. These precursor gases can be halides, chlorides, hydrides, metallorganic gases and other organic gases such as methyl silane. The precursor gases are typically diluted in an inert carrier gas such as nitrogen, hydrogen, helium, or argon. CVD techniques are classified on the basis of the pressure regime in which they operate, such as atmospheric pressure(APCVD), low pressure(LPCVD), very low pressure (VLPCVD) or ultra-high vacuum (UHVCVD). CVD can be further classified as a furnace heated, batch processing system or a single–wafer system. Reviews of the various CVD systems are provided in [34, 70].

Ultra–high vacuum chemical vapor deposition(UHVCVD) techniques have been used extensively to grow epitaxial layers for device applications. The ultra–high vacuum conditions provide the cleanest environment for growth of high quality epitaxial layers. UHVCVD was developed primarily by Meyerson [65] and has been modified and used by several other groups [47, 87], including the group that built and maintains the reactor used in this study [57].

2.2 UHVCVD Reactor Modelling

Accurate models that predict the behavior of the UHVCVD system are necessary for the estimation and control algorithms used in this work. The reactor model consists of kinetic reaction expressions coupled with material balances to yield a physical model of the film growth rate and the fraction of incorporated germanium as a function of the reactor's manipulated variables, which are the molar flow rates of the precursor gases, the reactor pressure, and the substrate temperature. A complete elementary mechanism describing disilane and germane adsorption and incorporation into epitaxial $\mathrm{Si}_{1-x}\mathrm{Ge}_x$ films and the corresponding kinetic models are the heart of the reactor model. Kuech [53] provides an excellent overview of the various models describing chemical vapor deposition for epitaxial growth.

Several groups have proposed kinetic models describing low pressure deposition of Si films via silane adsorption, [22, 28, 29, 30, 100] as well as disilane adsorption [15, 40, 60, 62, 88, 92]. These studies concur that there are two growth regimes: a low temperature regime and a high temperature regime. In the low temperature regime, film growth is rate-limited by hydrogen desorption from the silicon monohydride. The desorption of hydrogen from the surface allows for subsequent adsorption and decomposition of the gas precursor. Film growth rate is an exponential function of substrate temperature in this regime [31, 38, 59, 90]. At higher temperatures the growth rate is impingement–flux limited and the gas–phase concentration of the precursor species controls the growth rate.

Silicon–germanium alloys are readily deposited by UHVCVD. However the kinetic model needed to describe the deposition becomes much more complex as both disilane and germane compete for the adsorption sites on the growing surface. Several groups have studied the heteroepitaxial growth of $\mathrm{Si}_{1-x}\mathrm{Ge}_x$ alloys on silicon substrates [23, 27, 33, 43, 45, 46, 50, 51, 66, 74, 81, 82, 94, 103, 104]. The studies observed that the growth rate of the alloy system is greater than that of Si alone for the same total pressures. It is clear from these growth studies that the addition of germane significantly enhances the film growth rate, even when the germane is present at low levels. At low temperatures the rate-limiting step for film growth is removal of hydrogen from the growing surface. The presence of germanium on the film surface opens up a more facile route for monohydride decomposition and hydrogen desorption leading to an enhanced hydrogen desorption rate. Hydrogen attached to germanium sites is easily desorbed, freeing new adsorption sites. Additional precursor gases can now be adsorbed and the growth rate increases. Several groups have presented non-elementary mechanisms that model the major effects of $\mathrm{Si}_{1-x}\mathrm{Ge}_x$ alloy deposition, the most notable being [39, 63, 84, 85, 86].

2.3 Use of Ellipsometry for Monitoring and Control of Chemical Vapor Deposition

Accurate, real-time measurement of the properties of the deposited film is essential for monitoring and feedback control. Ellipsometry is an indirect sensor used in this work to characterize the optical properties of thin films. The principles of ellipsometry are based on the change in the polarization state of reflected light from the sample. This change can be related to the optical properties of the growing film and is reported in terms of the ellipsometric parameters Ψ and Δ. Various experimental configurations and methods [1, 4, 5, 9, 25, 49] have been designed that measure the polarization state of the reflected light. Excellent summaries of the various methods are given in [10, 11].

Inferring both film growth rate and composition simultaneously from Ψ and Δ measurements in real time is crucial for closed–loop control. Determining the outer layer dielectric function ϵ from ellipsometric measurements is the first step. The $\mathrm{Si}_{1-x}\mathrm{Ge}_x$ alloy composition is encoded in this complex–valued dielectric function [21, 55, 76, 77, 80].

The standard analysis is to assume that the growing film can be modeled as a series of laminar films, each with a specific height and dielectric function [10, 26, 35, 98]. The method assumes that the films are deposited in a steady and known rate and varying composition profiles are approximated by a sequence of laminar structures. Fresnel equations are then employed sequentially, establishing the dielectric function at the surface of the film in terms of the dielectric functions and thicknesses of all preceding layers. This method is highly sensitive to errors, especially cumulative errors that are propagated through each successive layer.

Another popular approach for determining the outer layer dielectric function of the growing film from ellipsometric measurements is given by Aspnes [6, 7, 8]. This approach, known as the virtual–interface method, hypothesizes that the growing film can be modeled as a very thin, homogeneous over-layer on top of an infinitely thick homogeneous “virtual substrate.” The presupposition of the virtual–interface method is that the film deposition rate is known and steady. Employing this assumption and letting the thickness of the over layer approach zero, the outer layer dielectric function can be obtained directly from ellipsometric measurements.

The obvious shortcoming of both methods is that they presume that the deposition rate is known and constant. As a consequence, information about only the film composition is available for feedback. Furthermore, if the assumed growth rate is erroneous or if it drifts during the growth due to an unmeasured disturbance, the calculated outer layer dielectric will be affected. The inferred film composition will then be in error, misrepresenting the true composition of the outer layer and rendering the sensor useless.

There have been several successful attempts to estimate growth rate as well from ellipsometric or reflectometry data [41, 79, 97, 102]. However, their techniques were applied to constant composition films. The methods presuppose that the dielectric function of the deposited film is constant and known. Again, if this supposition is in error or drifts during deposition, the estimated growth rate will be erroneous and its feedback will be futile.

The algorithm presented in this work simultaneously deduces from the ellipsometric measurements *both* the film growth rate and composition in real time. The heart of the algorithm is a dynamic, first–principles model of the ellipsometric sensor. The sensor model is integrated with the kinetic and process models describing the reactor and predicts the ellipsometric parameters Ψ and Δ during film growth. Based on the dynamic sensor model and the ellipsometer’s output, a time–varying, non–linear state estimator infers both the film growth rate and surface composition. Ultimately, the estimates of film growth rate and composition are utilized for closed–loop control of $\mathrm{Si}_{1-x}\mathrm{Ge}_x$ chemical vapor deposition.

Chapter 3

Experimental Apparatus

> *I'm very impressed with our ellipsometer*
>
> — Andy Kuehne, Verity Instruments

3.1 Ultra-High Vacuum Chemical Vapor Deposition Reactor Description

The chemical vapor deposition reactor used in this study for epitaxial growth differs from that described previously [67] in that the chamber walls are kept cold. Cooling the chamber walls reduces the amount of contaminants that outgas during subsequent depositions. Figure 3.1 shows a schematic of the chamber used for deposition.

The reactor consists of two chambers constructed out of 304L stainless steel, which is low in carbon. The secondary chamber, known as the load lock, protects the growth chamber from exposure to atmosphere during the wafer loading. The load-lock chamber is equipped with a quick-access port, which allows for the loading of up to 3 wafers onto holding shelves. An Alcatel turbo pump backed by an Alcatel mechanical pump brings the load lock down to 10^{-7} torr. A sentry valve and micro-maze trap placed upstream of the mechanical pump prevents back streaming of hydrocarbons into the load-lock chamber. Two sorption pumps placed in parallel with the turbo pump quickly pump down the load lock before wafer loading. An 8 inch gate valve isolates the load lock from the growth chamber. A convectron gauge and an ion gauge monitor the chamber and load-lock pressure.

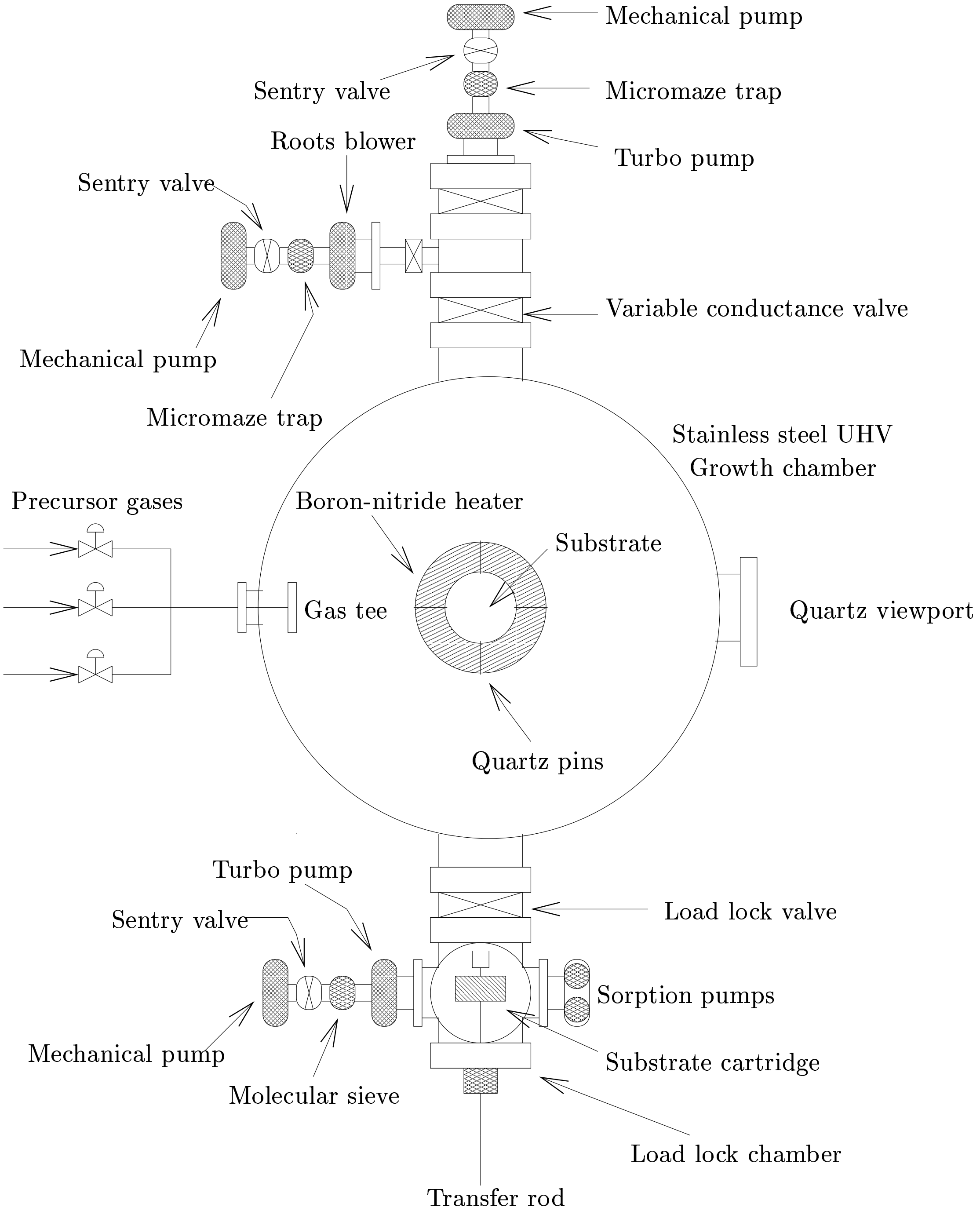

Figure 3.1: Ultra–high vacuum chemical vapor deposition reactor schematic

The wafer-holding shelves attached to a linear feed through allow access to all 3 wafers via the transfer rod. The transfer rod assembly consists of a magnetically coupled, linear motion feed through with a range of 36 inches, as well as an x-y manipulator for precise wafer positioning. A fork attached to the end of the transfer rod transports the wafer in and out of the growth chamber.

A boron-nitride substrate heater is attached to a linear feed through on the lid of the chamber. The feed through consists of two thimbles that allow the wafer and heater location to vary with respect to each other and the chamber. A rotator installed on the feed through positions the wafer for ellipsometric measurements as well as reflection-high-energy-electron-diffraction (RHEED) measurements. A residual gas analyzer (RGA) attached to the chamber characterizes and quantifies gas-phase concentrations.

A Balzers turbo pump backed by a dual-stage Diebold mechanical pump evacuates the large growth chamber to a base pressure of 10^{-10} torr. An Alcatel roots blower operates in parallel with the turbo pump, also backed by a dual-stage Alcatel mechanical pump. Sentry valves and micro-maze traps placed upstream of the mechanical pumps prevent hydrocarbon back streaming into the growth chamber. Gate valves isolate the turbo and roots pumps from the chamber and from each other.

3.2 Manipulated Variables

Figure 3.2 shows the manipulated variables for the UHVCVD reactor used in this study. Disilane and germane molar flow rates, reactor pressure, and substrate temperature are the manipulated variables used in this work for $\mathrm{Si}_{1-x}\mathrm{Ge}_x$ epitaxial growth. The manipulated variables of the reactor are not directly manipulated. Rather, a set point is sent to a cascaded controller, which then regulates the variable to the requested value.

3.2.1 Disilane and germane molar flow

Mass flow controllers (MFCs) regulate the flow of the precursor gases disilane and germane into the reactor. The disilane feed gas is 99.98% pure disilane, and the germane feed gas is 20% germane and 80% helium. The MFCs regulate both gas flows from 0 to 20 standard $\frac{\mathrm{cm}^3}{\mathrm{min}}$ (sccm).

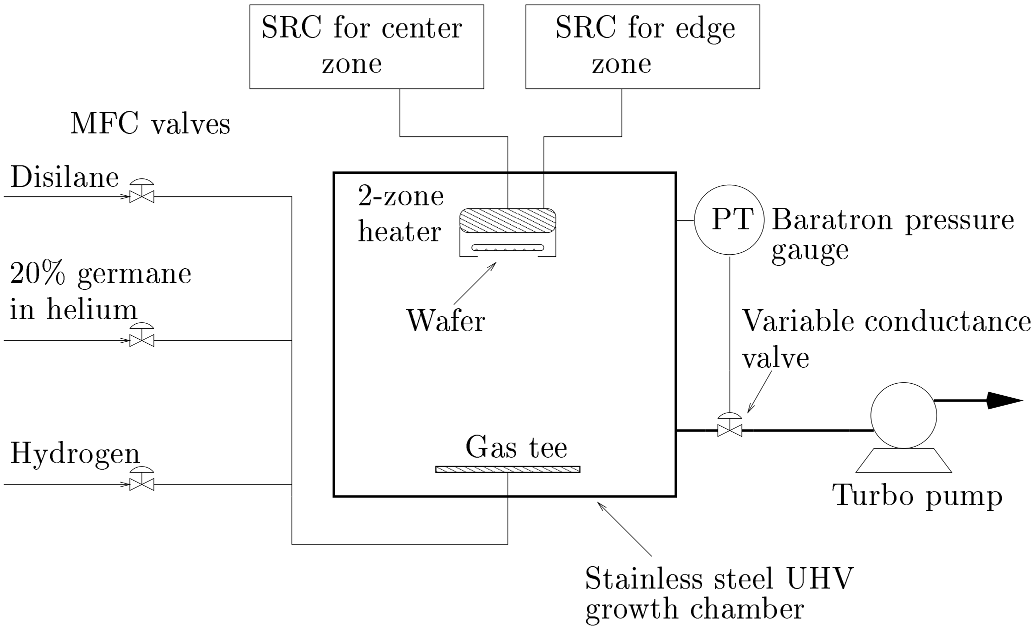

Figure 3.2: Reactor schematic showing manipulated variables

3.2.2 Reactor pressure

A variable conductance valve connected between the growth chamber and the downstream pumps maintains constant pressure in the growth chamber. The valve is manipulated by a VAT controller, which maintains chamber pressure at a desired set point.

3.2.3 Substrate temperature

The UHVCVD reactor is equipped with a two–zone, boron–nitride heating system. Each zone is controlled independently via two 120–volt power sources(SRC). The temperature of the wafer is measured with a Quantum Logic pyrometer and existing linear model predictive control theory based on an infinite quadratic regulator [73, 89] is utilized to regulate the wafer temperature. The two–zone heating system provides excellent temperature uniformity, and therefore growth uniformity, across the wafer. Further details of the boron–nitride heating system are presented in Appendix A.

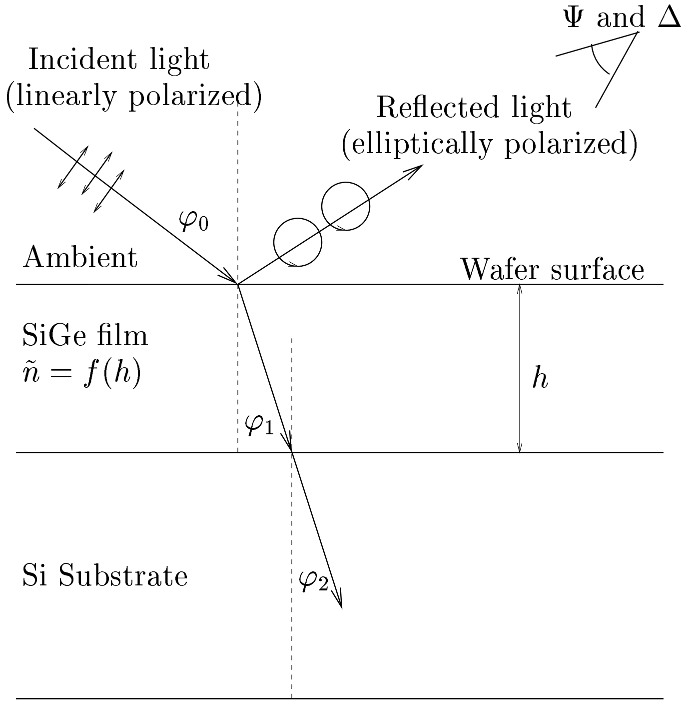

Figure 3.3: Spectroscopic ellipsometry for film thickness and composition monitoring

3.3 Spectroscopic Ellipsometry for Film Thickness and Composition Monitoring

Accurate, real-time measurement of film properties is essential for feedback control. A high-speed spectral ellipsometer is employed to observe and characterize, *in situ*, events that take place at the growing film interface. Ellipsometry is an experimental method that measures the polarization transformation that occurs when a beam of polarized light is reflected from a surface. The polarization state can be related to the complex reflectance ratio of the Fresnel coefficients of the sample

$$\rho = \frac{\mathcal{R}_p}{\mathcal{R}_s} \tag{3.1}$$

where $\mathcal{R}_p$ and $\mathcal{R}_s$ are the reflection coefficients of light polarized parallel to (p) or perpendicular to (s) the plane of incidence. For convenience, this ratio is written as

$$\rho = \tfrac{\mathcal{R}_p}{\mathcal{R}_s} = \tan(\Psi)\exp(i\Delta) \tag{3.2}$$

where the values of $\tan(\Psi)$ and Δ are the amplitude and phase of the complex-valued ratio. Equation 3.2 may be broken into two real equations for Ψ and Δ

$$\Psi = \arctan(|\rho|) \tag{3.3}$$
$$\Delta = \arg(\rho) \tag{3.4}$$

where $|\rho|$ and $\arg(\rho)$ are the absolute value and argument(angle) of the complex-valued function, ρ. The ellipsometric parameters Ψ and Δ are sensitive to changes in the surface conditions, over-layer thicknesses, and refractive indices of the sample [10, 14].

Figure 3.4 shows the Verity, phase modulated spectroscopic ellipsometer used in this work. It consists of a polarizer-modulator-sample-analyzer (PMSA) arrangement. A Xe arc lamp light source is delivered via fiber optics to polarization components. Light is passed through the photo-elastic modulator and then reflected off the sample and delivered via fiber optics to a grating monochromator and photo-diode array detector. The ellipsometric parameters Ψ and Δ are reported for each wavelength.

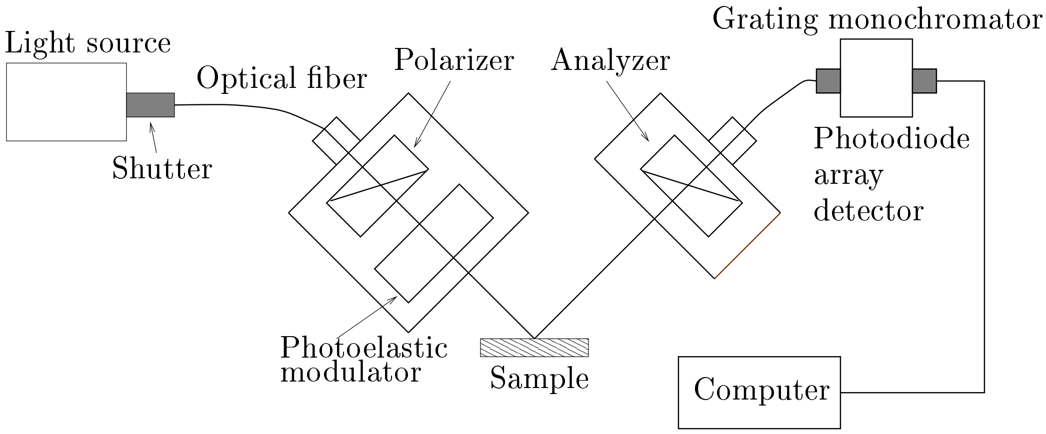

Figure 3.4: Optical setup of the ellipsometer

3.4 Data Acquisition

The hardware used to acquire measurement data and control the reactor consists of a signal conditioning(SCXI) system that communicates with a data acquisition(DAQ) board. The signal conditioning hardware used for this work was purchased from National Instruments and consists of a 16 channel isolated transducer multiplexer(SCXI–1122), a 6 channel isolated digital to analog(DAC) converter(SCXI–1124), a 32 channel optically isolated digital output module(SCXI–1163), and a 32 channel solid–state relay(SSR) module(SCXI–1163R), all bolted to a 12 slot chassis(SCXI–1001). A National Instruments E–Series board(AT–MIO–16E–1), which provides data sampling up to 1.25MHz, is used for data acquisition. The data acquisition and control software(LabView) and the driver software(NI–DAQ) for the DAQ board were also provided by National Instruments.

The host computer used for this work is a 500MHz Intel Pentium with Windows NT as the operating system. The host computer is the primary link between the operator and the UHVCVD reactor. In addition to collecting, storing, and displaying the real–time data, the computer also runs the model predictive controller described in Chapters 5 and 6. The estimation and regulation algorithms are coded and solved using MATLAB. Real–time data is communicated between LabView and MATLAB via dynamic–data exchange(DDE).

Chapter 4

Model Formulation

> *God the wind as windless as the world behind a computer screen*
>
> — Jane Miller, *High Holy Days*

A realistic and robust model is the cornerstone of any monitoring and model predictive control scheme. In this chapter a physical model based on first principles is proposed to quantitatively represent $Si_{1-x}Ge_x$ chemical vapor deposition. In Section 4.1 chemical reaction mechanisms are presented that describe the complicated behavior of the silicon/germanium deposition system. The kinetic models are incorporated into differential material balances in Section 4.2 yielding a physical model of the film growth rate and composition as a function of the reactor environment variables. In Section 4.4 a dynamic model of the ellipsometric sensor, which characterizes the optical properties of the growing film, is presented. The ordinary differential equations(ODEs) describing the process model and the optical model are then characterized succinctly in state-space form in Section 4.5. The state-space model is numerically integrated and the model prediction is compared with experimental data in Section 4.6.

4.1 Kinetics of $Si_{1-x}Ge_x$ Epitaxial Growth via Disilane and Germane Decomposition

At low pressures molecular collisions in the gas phase are negligible and surface collisions dominate. An elementary mechanism describing the decomposition of disilane and germane into epitaxial $Si_{1-x}Ge_x$ is proposed below. The mechanism includes pure disilane and germane deposition reactions as well as reactions that allow for the possibility of adsorption of Si_2H_6 on germanium sites and GeH_4 on silicon sites.

4.1.1 Disilane Adsorption and Decomposition

Si_2H_6 dissociatively adsorbs on $Si(s)$ or $Ge(s)$ surface dimers as two $SiH_3(s)$ radicals. The adsorbed $SiH_3(s)$ species further dissociate to form the dihydride $SiH_2(s)$ and the monohydride $SiH(s)$ [62, 92, 60, 31]. The mechanism further enunciates that adsorption of disilane is second order in surface site vacancy concentration [99].

$$\mathrm{Si_2H_6(g) + 2Si(s) \underset{k_{-1}}{\overset{k_1}{\rightleftharpoons}} 2SiH_3(s) + 2Si(b)} \tag{r_1}$$

$$\mathrm{Si(s) + SiH_3(s) \underset{k_{-2}}{\overset{k_2}{\rightleftharpoons}} SiH_2(s) + SiH(s)} \tag{r_2}$$

$$\mathrm{Si(s) + SiH_2(s) \underset{k_{-3}}{\overset{k_3}{\rightleftharpoons}} 2SiH(s)} \tag{r_3}$$

$$\mathrm{Si_2H_6(g) + 2Ge(s) \underset{k_{-4}}{\overset{k_4}{\rightleftharpoons}} 2SiH_3(s) + 2Ge(b)} \tag{r_4}$$

$$\mathrm{Si_2H_6(g) + Si(s) + Ge(s) \underset{k_{-5}}{\overset{k_5}{\rightleftharpoons}} 2SiH_3(s) + Si(b) + Ge(b)} \tag{r_5}$$

$Si(s)$ and $Ge(s)$ refer to silicon and germanium surface dangling bond sites and $Si(b)$ and $Ge(b)$ refer to subsurface or bulk atoms.

4.1.2 Germane Adsorption and Decomposition

Similar to disilane adsorption, GeH_4 is dissociatively adsorbed on $Si(s)$ or $Ge(s)$ surface sites via an activated precursor state that occupies only one site. The adsorbed species further dissociate to form $GeH_2(s)$ and GeH. The adsorption of germane is first order in surface site vacancy concentration.

$$\mathrm{GeH_4(g) + Ge(s) \underset{k_{-6}}{\overset{k_6}{\rightleftharpoons}} [GeH_4 \cdot Ge]} \tag{r_6}$$

$$\mathrm{[GeH_4 \cdot Ge] + Ge(s) \underset{k_{-7}}{\overset{k_7}{\rightleftharpoons}} 2GeH_2(s) + Ge(b)} \tag{r_7}$$

$$\mathrm{GeH_2(s) + Ge(s) \underset{k_{-8}}{\overset{k_8}{\rightleftharpoons}} 2GeH(s)} \tag{r_8}$$

$$\mathrm{GeH_4(g) + Si(s) \underset{k_{-9}}{\overset{k_9}{\rightleftharpoons}} [GeH_4 \cdot Si]} \tag{r_9}$$

$$\mathrm{[GeH_4 \cdot Si] + Si(s) \underset{k_{-10}}{\overset{k_{10}}{\rightleftharpoons}} GeH_2(s) + SiH_2(s) + Si(b)} \tag{r_{10}}$$

4.1.3 Hydrogen Desorption and Hydrogen Exchange

It is evident from growth studies that the presence of surface hydrogen during growth has a major effect on the overall kinetics at low growth temperatures [52, 84, 104, 94]. Following Sinniah, et al. [90], thermal desorption of molecular hydrogen from the silicon monohydride SiH(s) proceeds through the de-localized adatom H^* and is first order in SiH(s). The excited adatom H^* then reacts with a localized monohydride to produce H_2. The hydrogen molecule then desorbs, freeing a Si(s) surface site, which is available for subsequent adsorption. The thermal desorption of molecular hydrogen from the germanium monohydride GeH(s) is also first order in GeH(s), proceeding through the de-localized adatom H^*, producing H_2, and freeing a Ge(s) surface site [93].

It has been noted in CVD and MBE studies that the addition of germane to the incident flux not only permits $Si_{1-x}Ge_x$ alloys but also significantly enhances the film growth rate [103, 74, 27]. It can be concluded that the presence of surface germanium allows for a more facile route for hydrogen desorption. Thus, an equilibrium reaction that allows surface hydrogen transport between silicon and germanium sites is included in the mechanism [85]. The activation energy for this hydrogen exchange is lower than that of hydrogen desorption from a silicon site and higher than that of hydrogen desorption from a germanium site.

$$\mathrm{SiH(s)} \underset{k_{-11}}{\overset{k_{11}}{\rightleftharpoons}} \mathrm{Si(s)} + \mathrm{H^*} \qquad (r_{11})$$

$$\mathrm{GeH(s)} \underset{k_{-12}}{\overset{k_{12}}{\rightleftharpoons}} \mathrm{Ge(s)} + \mathrm{H^*} \qquad (r_{12})$$

$$\mathrm{H^*} + \mathrm{SiH(s)} \underset{k_{-13}}{\overset{k_{13}}{\rightleftharpoons}} \mathrm{Si(s)} + \mathrm{H_2(g)} \qquad (r_{13})$$

$$\mathrm{H^*} + \mathrm{GeH(s)} \underset{k_{-14}}{\overset{k_{14}}{\rightleftharpoons}} \mathrm{Ge(s)} + \mathrm{H_2(g)} \qquad (r_{14})$$

$$\mathrm{SiH(s)} + \mathrm{Ge(s)} \underset{k_{-15}}{\overset{k_{15}}{\rightleftharpoons}} \mathrm{Si(s)} + \mathrm{GeH(s)} \qquad (r_{15})$$

4.1.4 Reduced Kinetic Model

Assuming that the reactions r_2, r_3, r_7, r_8, r_{10}, r_{13}, and r_{14}, are fast and irreversible [29, 28, 92, 90, 30, 15, 23, 93], the preceding elementary mechanism reduces to the following non-elementary stoichiometry.

$$\mathrm{Si_2H_6(g)} + \mathrm{6Si(s)} \xrightarrow{\hat{\mathrm{k}}_1} \mathrm{6SiH(s)} + \mathrm{2Si(b)} \tag{$\hat{\mathrm{r}}_1$}$$

$$\mathrm{Si_2H_6(g)} + \mathrm{4Si(s)} + \mathrm{2Ge(s)} \xrightarrow{\hat{\mathrm{k}}_2} \mathrm{6SiH(s)} + \mathrm{2Ge(b)} \tag{$\hat{\mathrm{r}}_2$}$$

$$\mathrm{Si_2H_6(g)} + \mathrm{5Si(s)} + \mathrm{Ge(s)} \xrightarrow{\hat{\mathrm{k}}_3} \mathrm{6SiH(s)} + \mathrm{Si(b)} + \mathrm{Ge(b)} \tag{$\hat{\mathrm{r}}_3$}$$

$$\mathrm{GeH_4(g)} + \mathrm{4Ge(s)} \xrightarrow{\hat{\mathrm{k}}_4} \mathrm{4GeH(s)} + \mathrm{Ge(b)} \tag{$\hat{\mathrm{r}}_4$}$$

$$\mathrm{GeH_4(g)} + \mathrm{3Si(s)} + \mathrm{Ge(s)} \xrightarrow{\hat{\mathrm{k}}_5} \mathrm{2GeH(s)} + \mathrm{2SiH(s)} + \mathrm{Si(b)} \tag{$\hat{\mathrm{r}}_5$}$$

$$\mathrm{2SiH(s)} \xrightarrow{\hat{\mathrm{k}}_6} \mathrm{2Si(s)} + \mathrm{H_2(g)} \tag{$\hat{\mathrm{r}}_6$}$$

$$\mathrm{2GeH(s)} \xrightarrow{\hat{\mathrm{k}}_7} \mathrm{2Ge(s)} + \mathrm{H_2(g)} \tag{$\hat{\mathrm{r}}_7$}$$

$$\mathrm{SiH(s)} + \mathrm{Ge(s)} \underset{\hat{\mathrm{k}}_{-8}}{\overset{\hat{\mathrm{k}}_8}{\rightleftharpoons}} \mathrm{Si(s)} + \mathrm{GeH(s)} \tag{$\hat{\mathrm{r}}_8$}$$

4.1.5 Production Rates

Production rates for the nine species follow as

$$\begin{aligned}
R_{\mathrm{Si_2H_6}} &= -\hat{r}_1 - \hat{r}_2 - \hat{r}_3 && (4.1)\\
R_{\mathrm{GeH_4}} &= -\hat{r}_4 - \hat{r}_5 && (4.2)\\
R_{\mathrm{Si(s)}} &= -6\hat{r}_1 - 4\hat{r}_2 - 5\hat{r}_3 - 3\hat{r}_5 + 2\hat{r}_6 + \hat{r}_8 && (4.3)\\
R_{\mathrm{Ge(s)}} &= -2\hat{r}_2 - \hat{r}_3 - 4\hat{r}_4 - \hat{r}_5 + 2\hat{r}_7 - \hat{r}_8 && (4.4)\\
R_{\mathrm{SiH(s)}} &= 6\hat{r}_1 + 6\hat{r}_2 + 6\hat{r}_3 + 2\hat{r}_5 - 2\hat{r}_6 - \hat{r}_8 && (4.5)\\
R_{\mathrm{GeH(s)}} &= 4\hat{r}_4 + 2\hat{r}_5 - 2\hat{r}_7 + \hat{r}_8 && (4.6)\\
R_{\mathrm{Si(b)}} &= 2\hat{r}_1 + \hat{r}_3 + \hat{r}_5 && (4.7)\\
R_{\mathrm{Ge(b)}} &= 2\hat{r}_2 + \hat{r}_3 + \hat{r}_4 && (4.8)\\
R_{\mathrm{H_2}} &= \hat{r}_6 + \hat{r}_7 && (4.9)
\end{aligned}$$

represented in matrix form as

$$\begin{bmatrix} R_{\mathrm{Si_2H_6}} \\ R_{\mathrm{GeH_4}} \\ R_{\mathrm{Si(s)}} \\ R_{\mathrm{Ge(s)}} \\ R_{\mathrm{SiH(s)}} \\ R_{\mathrm{GeH(s)}} \\ R_{\mathrm{Si(b)}} \\ R_{\mathrm{Ge(b)}} \\ R_{\mathrm{H_2}} \end{bmatrix} = \begin{bmatrix} -1 & -1 & -1 & 0 & 0 & 0 & 0 & 0 \\ 0 & 0 & 0 & -1 & -1 & 0 & 0 & 0 \\ -6 & -4 & -5 & 0 & -3 & 2 & 0 & 1 \\ 0 & -2 & -1 & -4 & -1 & 0 & 2 & -1 \\ 6 & 6 & 6 & 0 & 2 & -2 & 0 & -1 \\ 0 & 0 & 0 & 4 & 2 & 0 & -2 & 1 \\ 2 & 0 & 1 & 0 & 1 & 0 & 0 & 0 \\ 0 & 2 & 1 & 1 & 0 & 0 & 0 & 0 \\ 0 & 0 & 0 & 0 & 0 & 1 & 1 & 0 \end{bmatrix} \begin{bmatrix} \hat{r}_1 \\ \hat{r}_2 \\ \hat{r}_3 \\ \hat{r}_4 \\ \hat{r}_5 \\ \hat{r}_6 \\ \hat{r}_7 \\ \hat{r}_8 \end{bmatrix} \tag{4.10}$$

and summarized as

$$\mathbf{R} = \nu^T \mathbf{r} \tag{4.11}$$

where ν^T denotes the transpose of the stoichiometric matrix. Reaction $\hat{r}_8$ is at equilibrium yielding

$$[\mathrm{GeH(s)}] = \frac{K_8[\mathrm{SiH(s)}][\mathrm{Ge(s)}]}{[\mathrm{Si(s)}]} \tag{4.12}$$

providing one of nine equations needed to solve for the nine species concentrations. Linear combinations of the stoichiometric matrix ν that eliminate any dependence of $\mathbf{R}$ on $\hat{r}_8$ keeps the problem well posed and provides the eight remaining equations. Partitioning the stoichiometric matrix that consists of the reactions assumed at equilibrium yields

$$\nu_{eq}^T \triangleq \begin{bmatrix} 0 \\ 0 \\ 1 \\ -1 \\ -1 \\ 1 \\ 0 \\ 0 \\ 0 \end{bmatrix} \tag{4.13}$$

Defining $\mathcal{N}_{\nu_{eq}}$ as the orthonormal basis of the null space of ν_{eq} and multiplying it with the production rates provides the eight remaining equations.

$$\mathcal{N}_{\nu_{eq}}^T \mathbf{R} = \mathcal{N}_{\nu_{eq}}^T \nu^T \mathbf{r} \tag{4.14}$$

4.1.6 Reaction Rates and Model Parameters

Reaction rates for the reduced mechanism are given by

$$\hat{r}_1 = \hat{k}_1 C_{\mathrm{Si_2H_6}}[\mathrm{Si(s)}]^2 \quad (4.15)$$

$$\hat{r}_2 = \hat{k}_2 C_{\mathrm{Si_2H_6}}[\mathrm{Ge(s)}]^2 \quad (4.16)$$

$$\hat{r}_3 = \hat{k}_3 C_{\mathrm{Si_2H_6}}[\mathrm{Ge(s)}][\mathrm{Si(s)}] \quad (4.17)$$

$$\hat{r}_4 = \hat{k}_4 C_{\mathrm{GeH_4}}[\mathrm{Ge(s)}] \quad (4.18)$$

$$\hat{r}_5 = \hat{k}_5 C_{\mathrm{GeH_4}}[\mathrm{Si(s)}] \quad (4.19)$$

$$\hat{r}_6 = \hat{k}_6[\mathrm{SiH(s)}] \quad (4.20)$$

$$\hat{r}_7 = \hat{k}_7[\mathrm{GeH(s)}] \quad (4.21)$$

$$\hat{r}_8 = 0 \quad (4.22)$$

The kinetic rate constants for the above reactions are of the Arrhenius type

$$\hat{k}_i = A_i e^{(-E_i/RT_s)} \quad (4.23)$$

where T_s is the substrate temperature. The values of the pre-exponential factors A_i and the activation energies E_i can be either obtained from literature or inferred from experimental data. The kinetic parameters used for this work are listed in Table 4.1. Reaction $\hat{r}_8$ is at equilibrium and its reaction constant is given as

$$\hat{K}_8 = e^{(\Delta S_8/R)} e^{(-\Delta H_8/RT_s)} \quad (4.24)$$

with ΔS_8 and ΔH_8 listed in Table 4.2. The physical parameters for the reactor used in this study are listed in Table 4.3.

Pre-exponential factor			Activation energy			Source(if applicable)
A_1	7.26×10^{-3}	$\frac{\mathrm{cm}^5}{\mathrm{mol \cdot s}}$	E_1	0	$\frac{\mathrm{kcal}}{\mathrm{mol}}$	[15]
A_2	1.0×10^{-2}	$\frac{\mathrm{cm}^5}{\mathrm{mol \cdot s}}$	E_2	0	$\frac{\mathrm{kcal}}{\mathrm{mol}}$	Inferred
A_3	1.0×10^{-2}	$\frac{\mathrm{cm}^5}{\mathrm{mol \cdot s}}$	E_3	0	$\frac{\mathrm{kcal}}{\mathrm{mol}}$	Inferred
A_4	1.0×10^{10}	$\frac{\mathrm{cm}^3}{\mathrm{mol \cdot s}}$	E_4	2.0×10^3	$\frac{\mathrm{kcal}}{\mathrm{mol}}$	[85]
A_5	1.0×10^{11}	$\frac{\mathrm{cm}^3}{\mathrm{mol \cdot s}}$	E_5	2.0×10^3	$\frac{\mathrm{kcal}}{\mathrm{mol}}$	[85]
A_6	1.0×10^{12}	s^{-1}	E_6	47.0×10^3	$\frac{\mathrm{kcal}}{\mathrm{mol}}$	[90]
A_7	9.99×10^{14}	s^{-1}	E_7	37.0×10^3	$\frac{\mathrm{kcal}}{\mathrm{mol}}$	[86]

Table 4.1: Kinetic parameters for disilane and germane decomposition.

Entropy			Enthalpy			Source
ΔS_8	5.97	$\frac{\text{cal}}{\text{mol}\cdot\text{K}}$	ΔH_8	16.0×10^3	$\frac{\text{kcal}}{\text{mol}}$	[86]

Table 4.2: Equilibrium parameters for the hydrogen exchange reaction $\hat{r}_8$.

Physical parameter	Value
Reactor volume (V_R)	7.0×10^4 cm^3
Wafer area (A_w)	81.1 cm^2
Reactor gas temperature (T_g)	673 K

Table 4.3: Physical parameters of the reactor

4.2 Material Balances

The reactor operates at a low pressure and is modeled as a well-mixed, continuous-stirred-tank reactor(CSTR). Material balances around the reactor yield

$$\frac{d(C_{\mathrm{Si_2H_6}}V_R)}{dt} = \dot{N}_{\mathrm{Si_2H_6}} - \dot{Q}C_{\mathrm{Si_2H_6}} + A_w R_{\mathrm{Si_2H_6}} \tag{4.25}$$

$$\frac{d(C_{\mathrm{GeH_4}}V_R)}{dt} = \dot{N}_{\mathrm{GeH_4}} - \dot{Q}C_{\mathrm{GeH_4}} + A_w R_{\mathrm{GeH_4}} \tag{4.26}$$

$$\frac{d(C_{\mathrm{H_2}}V_R)}{dt} = -\dot{Q}C_{\mathrm{H_2}} + A_w R_{\mathrm{H_2}} \tag{4.27}$$

$$\frac{d(C_{\mathrm{He}}V_R)}{dt} = \dot{N}_{\mathrm{He}} - \dot{Q}C_{\mathrm{He}} \tag{4.28}$$

$$\frac{d([\mathrm{Si(s)}])}{dt} = R_{\mathrm{Si(s)}} \tag{4.29}$$

$$\frac{d([\mathrm{Ge(s)}])}{dt} = R_{\mathrm{Ge(s)}} \tag{4.30}$$

$$\frac{d([\mathrm{SiH(s)}])}{dt} = R_{\mathrm{SiH(s)}} \tag{4.31}$$

$$\frac{d([\mathrm{GeH(s)}])}{dt} = R_{\mathrm{GeH(s)}}, \tag{4.32}$$

where V_R is the reactor volume and A_w is the substrate surface area. The production rates R_i are given in Section 4.1. The volumetric flow rate $\dot{Q}$ exiting the reactor is established by satisfying an additional equation of state. Since the reactor operates at very low pressures, the ideal gas law is assumed.

$$0 = \sum C_j - \frac{P}{RT_g} \tag{4.33}$$

T_g is the temperature of the gas in the reactor and P is the total reactor pressure. The mass flow controllers(MFC) regulate the molar flow rates of the precursor gases $\dot{N}_i$ into the reactor. Each MFC valve is calibrated to a standard. The product of this standard with the fractional opening yields the molar flow rate into the reactor. Table 4.4 gives the maximum molar flow rate for each gas when the MFC valves are completely open. Helium is also listed considering that the precursor gas germane is diluted in helium.

Disilane	Germane	Helium
$1.72 \times 10^{-5} \quad \frac{\text{mol}}{\text{s}}$	$6.13 \times 10^{-6} \quad \frac{\text{mol}}{\text{s}}$	$2.45 \times 10^{-5} \quad \frac{\text{mol}}{\text{s}}$

Table 4.4: Maximum molar flow rates of the precursor gases

4.3 Film Growth Rate and Composition

The growth rate for the alloy deposition is the rate of change of the film height h

$$\mathcal{G} \equiv \frac{dh}{dt} \tag{4.34}$$

The film growth rate is simply the sum of the production rates of Si(b) and Ge(b) scaled by their respective atomic densities, ρ_{Si} and ρ_{Ge}.

$$\frac{dh}{dt} = \frac{R_{\text{Si(b)}}}{\rho_{\text{Si}}} + \frac{R_{\text{Ge(b)}}}{\rho_{\text{Ge}}} \tag{4.35}$$

The percentage of germanium on the surface, the x in $\text{Si}_{1-x}\text{Ge}_x$, is given by the ratio of production

$$x = \frac{R_{\text{Ge(b)}}}{R_{\text{Si(b)}} + R_{\text{Ge(b)}}} \tag{4.36}$$

the expressions for $R_{\text{Si(b)}}$ and $R_{\text{Ge(b)}}$ are given in Section 4.1.

4.4 Optical Model

An ellipsometer is an indirect sensor used to characterize the optical properties of the growing thin film. A dynamic model predicting the response of the optical sensor is necessary for the state estimation techniques described in Chapter 5. Fresnel's equations are the foundation of the ellipsometry models described in this section and are reviewed in Section 4.4.1. A matrix method that can be used to approximate the underlying film structure is presented in Section 4.4.2. The matrix method is then applied to infinitesimally thin layers, producing a continuous and dynamic model of the optical response of the growing film.

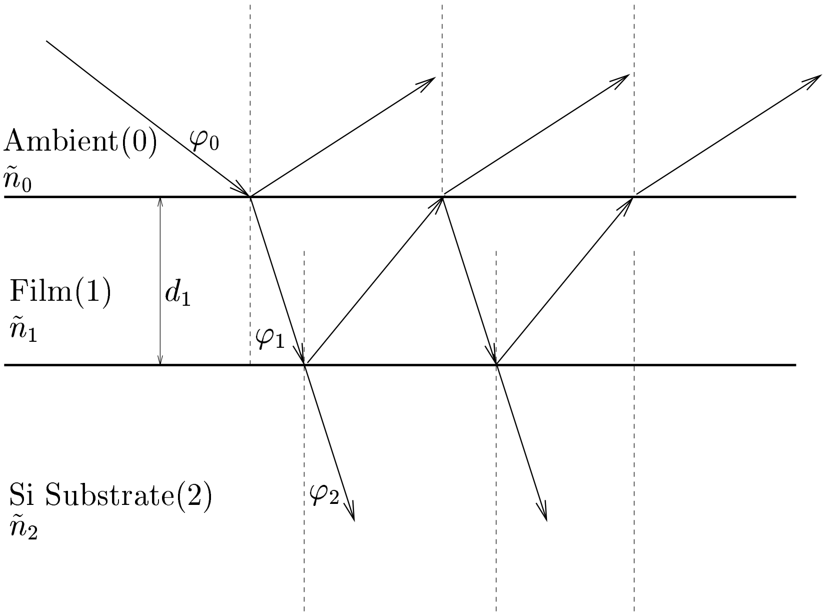

Figure 4.1: Reflection and transmission of a plane wave by an ambient(0)-film(1)-substrate(2) system.

4.4.1 Background Optics

Consider reflection from an optically–isotropic, three–phase, ambient–film–substrate system, which is shown in Figure 4.1. A plane wave incident at angle φ_0 in medium(0) produces a reflected wave in the same medium as well as a transmitted waves at angle φ_1 in medium(1) and a transmitted wave at angle φ_2 in medium(2). Presuming that the lateral dimension of the film is many times its thickness, the multiply-reflected and transmitted waves combine coherently, and the film material is non-amplifying, the Fresnel reflection and transmission coefficients at the ambient-film$(0-1)$ and film-substrate$(1-2)$ interfaces are given by [61, 35, 10]

$$r_{01p} = \frac{\tilde{n}_1\cos(\varphi_0) - \tilde{n}_0\cos(\varphi_1)}{\tilde{n}_1\cos(\varphi_0) + \tilde{n}_0\cos(\varphi_1)} \tag{4.37}$$

$$r_{12p} = \frac{\tilde{n}_2\cos(\varphi_1) - \tilde{n}_1\cos(\varphi_2)}{\tilde{n}_2\cos(\varphi_1) + \tilde{n}_1\cos(\varphi_2)} \tag{4.38}$$

$$r_{01s} = \frac{\tilde{n}_0\cos(\varphi_0) - \tilde{n}_1\cos(\varphi_1)}{\tilde{n}_0\cos(\varphi_0) + \tilde{n}_1\cos(\varphi_1)} \tag{4.39}$$

$$r_{12s} = \frac{\tilde{n}_1\cos(\varphi_1) - \tilde{n}_2\cos(\varphi_2)}{\tilde{n}_1\cos(\varphi_1) + \tilde{n}_2\cos(\varphi_2)} \tag{4.40}$$

$$t_{01p} = \frac{2\tilde{n}_0\cos(\varphi_0)}{\tilde{n}_1\cos(\varphi_0) + \tilde{n}_0\cos(\varphi_1)} \tag{4.41}$$

$$t_{12p} = \frac{2\tilde{n}_1\cos(\varphi_1)}{\tilde{n}_2\cos(\varphi_1) + \tilde{n}_1\cos(\varphi_2)} \tag{4.42}$$

$$t_{01s} = \frac{2\tilde{n}_0\cos(\varphi_0)}{\tilde{n}_0\cos(\varphi_0) + \tilde{n}_1\cos(\varphi_1)} \tag{4.43}$$

$$t_{12s} = \frac{2\tilde{n}_1\cos(\varphi_1)}{\tilde{n}_1\cos(\varphi_1) + \tilde{n}_2\cos(\varphi_2)} \tag{4.44}$$

where the s and p subscripts indicate the polarization states of the reflected and transmitted waves. The three angles φ_0, φ_1, and φ_2 between the directions of propagation of the plane waves in media (0), (1), and (2) and the normal to the film boundaries are related through application of Snell's law.

$$\tilde{n}_0\sin(\varphi_0) = \tilde{n}_1\sin(\varphi_1) = \tilde{n}_2\sin(\varphi_2) \tag{4.45}$$

The complex-valued indices of refraction $\tilde{n}_0$, $\tilde{n}_1$, and $\tilde{n}_2$ of the ambient, film, and substrate, respectively, are expressed as

$$\tilde{n} = n - i\kappa \tag{4.46}$$

where n is the index of refraction and κ is the extinction coefficient of the medium. The parameter κ, also known as the absorption index, quantifies the attenuation of the plane wave traveling through the medium. The complex–valued index of refraction is dependent on the wavelength of the incident light as well as the composition of germanium in the film. It is this composition dependence that allows the percentage of germanium on the film surface to be inferred from ellipsometric measurements.

Pure component values for the complex indices of refraction for Si and Ge are given in standard references [75, 2]. However, the database for the indices of refraction for $\mathrm{Si}_{1-x}\mathrm{Ge}_x$ alloys is quite incomplete. Chen, et al. [21] identified an empirical mapping that relates the dielectric function of strained $\mathrm{Si}_{1-x}\mathrm{Ge}_x$ layers to the fraction of germanium in the film. This mapping, which is utilized in this work, is given as

$$\epsilon(x, E) = \epsilon(0, E + 0.4805x) + \frac{10.575x}{(3.050 - 0.6556x)^2 - E^2 + i0.5028E} \tag{4.47}$$

The first term on the right-hand side is the dielectric function of crystalline silicon with energy shifted linearly with the percentage of germanium x. The photon energy E is related to the wavelength by

$$E = \frac{\hbar c}{\lambda} \tag{4.48}$$

where $\hbar$ is Planck's constant and c is the speed of light. The dielectric function is related to the complex index of refraction by

$$\epsilon = \tilde{n}^2 \tag{4.49}$$

Figures 4.4.1 and 4.4.1 show the dependence of the index of refraction of $\mathrm{Si}_{1-x}\mathrm{Ge}_x$ alloys on the germanium composition x for several wavelengths. It is clear from the figures that at some wavelengths the indices of refraction are not dependent on the alloy composition.

The overall complex-valued reflection ($\mathcal{R}$) and transmission ($\mathcal{T}$) coefficients for the ambient-film-substrate system in terms of the Fresnel coefficients are given by [10]

$$\mathcal{R}_p = \frac{r_{01p} + r_{12p}\exp(-i2\beta)}{1 + r_{01p}r_{12p}\exp(-i2\beta)} \tag{4.50}$$

$$\mathcal{R}_s = \frac{r_{01s} + r_{12s}\exp(-i2\beta)}{1 + r_{01s}r_{12s}\exp(-i2\beta)} \tag{4.51}$$

$$\mathcal{T}_p = \frac{t_{01p}t_{12p}\exp(-i2\beta)}{1 + r_{01p}r_{12p}\exp(-i2\beta)} \tag{4.52}$$

$$\mathcal{T}_s = \frac{t_{01s}t_{12s}\exp(-i2\beta)}{1 + r_{01s}r_{12s}\exp(-i2\beta)} \tag{4.53}$$

where the s and p subscripts again indicate the polarization states of the reflected or transmitted waves. The film phase thickness, also known as the phase angle is given by

$$\beta = \frac{2\pi d_1}{\lambda}\tilde{n}_1\cos(\varphi_1) \tag{4.54}$$

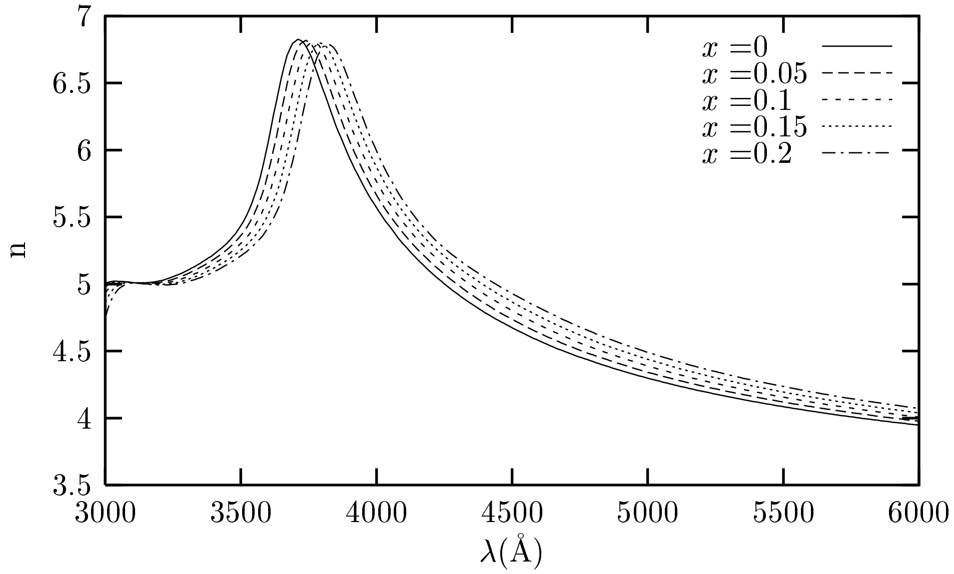

Figure 4.2: Refractive index spectra of strained $Si_{1-x}Ge_x$ alloys grown on Si calculated from Equation 4.47

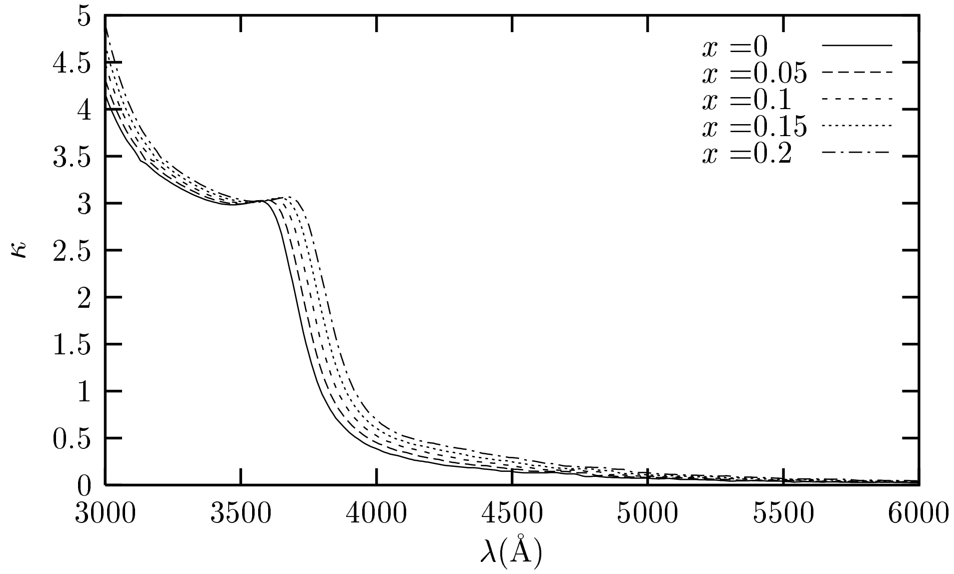

Figure 4.3: Extinction coefficient spectra of strained $Si_{1-x}Ge_x$ alloys grown on Si calculated from Equation 4.47

where λ is the wavelength of light in vacuum and d_1 is the film-layer thickness. Thus, given trial or known reference values for the independent parameters, $\tilde{n}_0, \tilde{n}_1, \tilde{n}_2, d_1, \varphi_0, \lambda$, values of the ellipsometric parameters Ψ and Δ for an ambient–film–substrate model can be calculated.

$$\begin{aligned} \rho &\equiv \frac{\mathcal{R}_p}{\mathcal{R}_s} && (4.55) \\ \Psi &= \arctan\left(|\rho|\right) && (4.56) \\ \Delta &= \arg\left(\rho\right) && (4.57) \end{aligned}$$

4.4.2 Matrix Method Using Fresnel Coefficients

The matrix method assumes that the growing film is composed of sequential layers of homogeneous films each with its own thickness and index of refraction. Consider the k_{th} film of a system of stratified multiple layers, which is shown in Figure 4.4. Each layer has a thickness d_k and complex index of refraction $\tilde{n}_k$. Following [61], the tangential components of the electric and magnetic vectors, E and H, on each side of the film are related through a linear recursion. The linear dependence of E_{k-1} and H_{k-1} at the $k-1$ plane on E_k and H_k at the k boundary may be written in matrix form as

$$\begin{bmatrix} E_{k+1} \\ H_{k+1} \end{bmatrix} = \begin{bmatrix} \cos(\varkappa_k d_k) & i\frac{\sin(\varkappa_k d_k)}{\eta_k} \\ i\frac{\sin(\varkappa_k d_k)}{\eta_k} & \cos(\varkappa_k d_k) \end{bmatrix} \begin{bmatrix} E_k \\ H_k \end{bmatrix} \qquad (4.58)$$

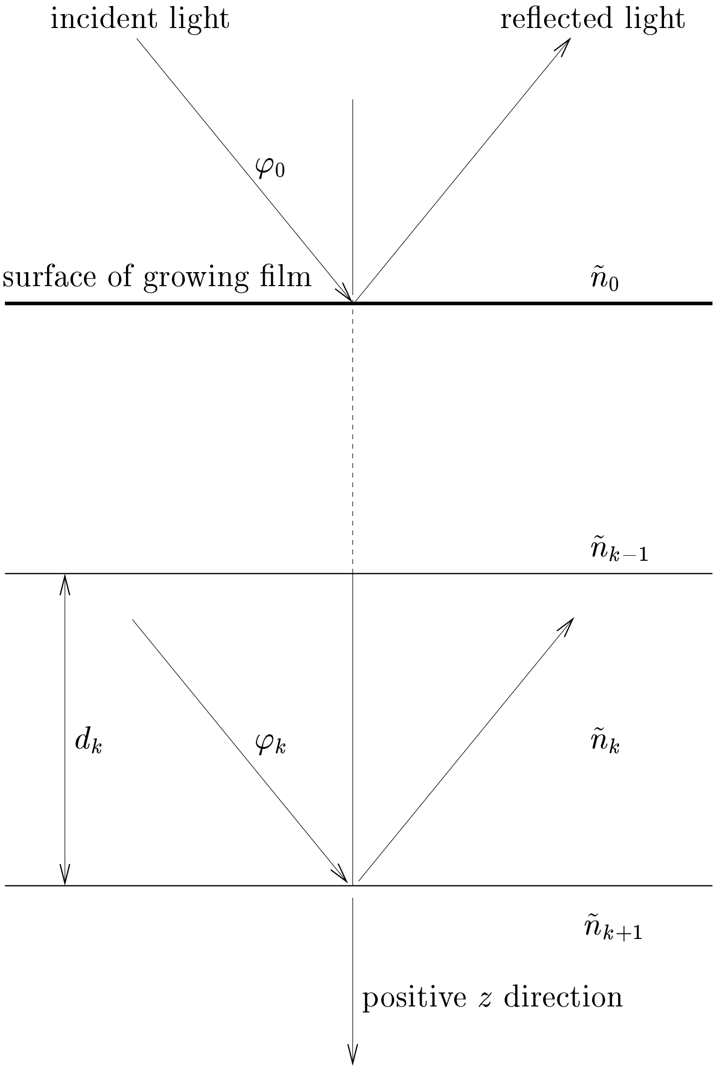

Figure 4.4: The k_{th} layer of a system of multiple layers.

Equation 4.58 is valid for the two possible cases of polarization; the electric vector polarized parallel(p) or perpendicular(s) to the plane of incidence. The effective indices of refraction for parallel(p) and perpendicular(s) polarized fields are defined as

$$\eta_{pk} = \frac{\tilde{n}_k}{\cos\varphi_k} \tag{4.59}$$

$$\eta_{sk} = \tilde{n}_k \cos\varphi_k. \tag{4.60}$$

The parameter $\varkappa_k$ is a function of the wavelength of the incident light λ, the layer angle φ_k, as well as the layer material's complex index of refraction $\tilde{n} = n - i\kappa$.

$$\varkappa_k = \frac{2\pi\tilde{n}_k\cos(\varphi_k)}{\lambda} \tag{4.61}$$

The angle of incidence at each layer φ_k is determined through repeated application of Snell's law

$$\tilde{n}_0 \sin(\varphi_0) = \tilde{n}_k \sin(\varphi_k), \tag{4.62}$$

where φ_0 is the angle of the incident wave to normal and $\tilde{n}_0$ is the refractive index of the vacuum. Following [35] the optical admittance is defined as

$$\Upsilon \equiv \frac{H_{tangential}}{E_{tangential}} \tag{4.63}$$

Thus from Equation 4.58 the admittance at each boundary for a system of homogeneous layers is given for both polarizations by

$$\Upsilon_{p_{k-1}} = \eta_{p_k}\frac{\Upsilon_{p_k}\cos\varkappa_k d_k + i\eta_{p_k}\sin\varkappa_k d_k}{\eta_{p_k}\cos\varkappa_k d_k + i\Upsilon_{p_k}\sin\varkappa_k d_k} \tag{4.64}$$

$$\Upsilon_{s_{k-1}} = \eta_{s_k}\frac{\Upsilon_{s_k}\cos\varkappa_k d_k + i\eta_{s_k}\sin\varkappa_k d_k}{\eta_{s_k}\cos\varkappa_k d_k + i\Upsilon_{s_k}\sin\varkappa_k d_k} \tag{4.65}$$

The complex-valued reflection coefficients follow as

$$\mathcal{R}_p = \frac{\Upsilon_p - \eta_p}{\eta_p + \Upsilon_p} \tag{4.66}$$

$$\mathcal{R}_s = \frac{\eta_s - \Upsilon_s}{\eta_s + \Upsilon_s} \tag{4.67}$$

with the ellipsometric parameters Ψ and Δ determined by

$$\rho \equiv \frac{\mathcal{R}_p}{\mathcal{R}_s} \tag{4.68}$$

$$\Psi = \arctan(|\rho|) \tag{4.69}$$

$$\Delta = \arg(\rho) \tag{4.70}$$

Notice that Equations 4.64 and 4.65 are recursive and can be modeled as evolving states.

4.4.3 Dynamic Ellipsometric Sensor Model

Equations 4.64 and 4.65 may be readily expressed as continuous functions in which the material's refractive index varies in the direction of propagation. Suppose at a point in the system of layers, which has an admittance Υ, a thin layer dh, with an effective refractive index η, is added. The value of Υ changes to $\Upsilon + d\Upsilon$ and Equations 4.64 and 4.65 are expressed as

$$\frac{d\Upsilon_p}{dt} = -i\eta_p \varkappa \left(\frac{\Upsilon_p^2}{\eta_p^2} - 1 \right) \mathcal{G} \tag{4.71}$$

$$\frac{d\Upsilon_s}{dt} = -i\eta_s \varkappa \left(\frac{\Upsilon_s^2}{\eta_s^2} - 1 \right) \mathcal{G} \tag{4.72}$$

where the growth rate $\mathcal{G}$ is defined in Equation 4.35. The above differential equation can be integrated with the material balances, Equations 4.25 through 4.32, yielding the admittance Υ at the surface of the film. The admittance at the surface of the growing film is now modeled as a dynamically evolving state. The dynamic, complex-valued reflection coefficients follow as

$$\mathcal{R}_p(t) = \frac{\Upsilon_p(t) - \eta_p(t)}{\eta_p(t) + \Upsilon_p(t)} \tag{4.73}$$

$$\mathcal{R}_s(t) = \frac{\eta_s(t) - \Upsilon_s(t)}{\eta_s(t) + \Upsilon_s(t)} \tag{4.74}$$

The dynamic ellipsometric parameters $\Psi(t)$ and $\Delta(t)$ are determined by

$$\rho(t) \equiv \frac{\mathcal{R}_p(t)}{\mathcal{R}_s(t)} \tag{4.75}$$

$$\Psi(t) = \arctan\left(|\rho(t)|\right) \tag{4.76}$$

$$\Delta(t) = \arg\left(\rho(t)\right) \tag{4.77}$$

4.4.4 Choice of wavelength

The ellipsometer is able to report Ψ and Δ for several wavelengths. However, for $\mathrm{Si}_{1-x}\mathrm{Ge}_x$ deposition only two are really necessary. Figure 4.5 shows the 2–wavelength sensor that is envisioned. The ellipsometric parameter Δ that corresponds to the "short" wavelength attenuates rapidly and detects the composition variation at the surface of the film. The longer wavelength of light must be able to penetrate the growing film and reach the substrate in order for the corresponding Δ to carry any information about the film growth rate. The model is able to assist in choosing these wavelengths. The penetration depth for absorbing media is given by

$$d = \frac{\lambda}{4\pi\kappa} \tag{4.78}$$

where κ is given by the mapping in Equation 4.47. The longer wavelength must be chosen so that the penetration depth for that wavelength is larger than the total film that is to be deposited.

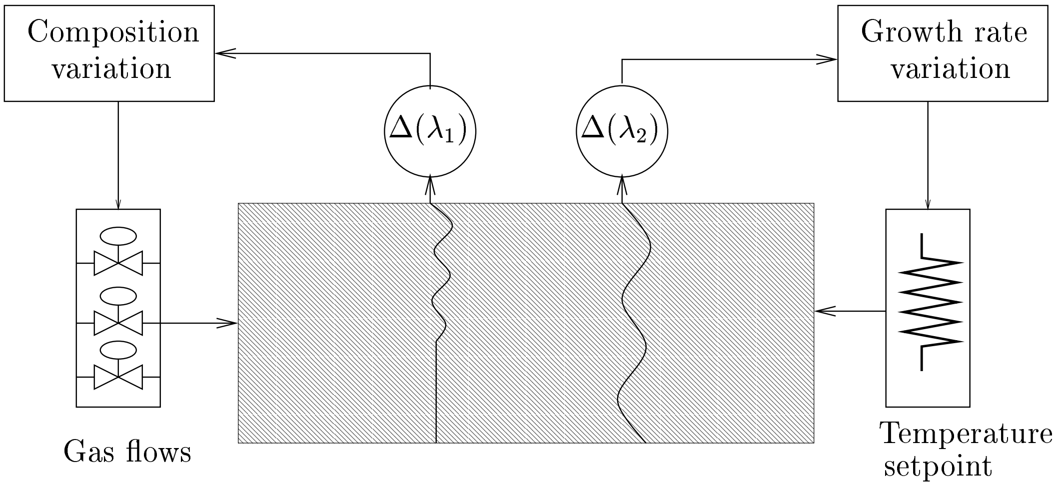

Figure 4.5: Spectral sensor and information decoupling

4.5 State Space Representation

The process model described in this chapter can be characterized succinctly in state-space form as

$$\frac{d\mathbf{x}}{dt} = \mathbf{f}(\mathbf{x}, \mathbf{u}, t) \tag{4.79}$$
$$\mathbf{y} = \mathbf{g}(\mathbf{x}) \tag{4.80}$$
$$\mathbf{z} = \mathbf{h}(\mathbf{x}) \tag{4.81}$$

with the inputs, states, and outputs defined as follows:

- Inputs $\mathbf{u}$: MFC set points for disilane and germane, reactor pressure set point, substrate temperature set point

$$\mathbf{u} = \begin{bmatrix} M^{\mathrm{sp}}_{\mathrm{Si_2H_6}} \\ M^{\mathrm{sp}}_{\mathrm{GeH_4}} \\ P^{\mathrm{sp}} \\ T^{\mathrm{sp}}_s \end{bmatrix} \tag{4.82}$$

- States $\mathbf{x}$: Gas phase concentrations, substrate surface concentrations, molar flows for disilane and germane, reactor pressure, substrate temperature, film height, optical admittance for both wavelengths

$$\mathbf{x} = \begin{bmatrix} C_{\mathrm{Si_2H_6}} \\ C_{\mathrm{GeH_4}} \\ C_{\mathrm{H_2}} \\ C_{\mathrm{He}} \\ [\mathrm{Si(s)}] \\ [\mathrm{Ge(s)}] \\ [\mathrm{SiH(s)}] \\ [\mathrm{GeH(s)}] \\ \dot{N}_{\mathrm{Si_2H_6}} \\ \dot{N}_{\mathrm{GeH_4}} \\ P \\ T_s \\ h \\ \Upsilon_p(\lambda_1) \\ \Upsilon_s(\lambda_1) \\ \Upsilon_p(\lambda_2) \\ \Upsilon_s(\lambda_2) \end{bmatrix} \tag{4.83}$$

- Measured outputs $\mathbf{y}$: Ellipsometric data for each wavelength

$$\mathbf{y} = \begin{bmatrix} \Delta(\lambda_1) \\ \Delta(\lambda_2) \end{bmatrix} \tag{4.84}$$

  Notice that only Δ for each wavelength is considered a measured output. Ellipsometers are not able to precisely differentiate both Ψ and Δ. In addition, the information contained in both parameters is essentially redundant. Thus the ellipsometric parameter Ψ is dropped from the output vector and Δ is retained.

- Regulated outputs $\mathbf{z}$: Film growth rate and germanium composition at the surface of the film

$$\mathbf{z} = \begin{bmatrix} \mathcal{G} \\ x \end{bmatrix} \tag{4.85}$$

4.6 Model Validation

Several experiments were performed in order to validate the model and the parameters listed in Table 4.1 and Table 4.2. Experimental inputs were generated off-line and the time-varying manipulated variables were then applied to the UHVCVD reactor. The resulting films were then analyzed off-line using either secondary ion mass spectrometry (SIMS) or Auger characterization. Figures 4.6 through 4.10 show one such validation run. The disilane and germane MFC valve positions during the experimental run are shown in Figure 4.6. The pressure in the reactor was held constant at 26 mTorr during the run. Figure 4.7 shows the substrate temperature set point sent to the cascaded temperature controller during the run as well as the temperature response measured by the pyrometer. In Figures 4.8 and 4.9 predicted values of Ψ and Δ for $\lambda = 5520\text{Å}$ are compared to the measured values reported by the ellipsometer in real time. The resulting film prediction and its verification by SIMS are shown in Figure 4.10. The model predicts the real–time ellipsometric response as well as the film profile. However, there is some disagreement, which may be caused by an unmeasured disturbance or a simple model mismatch, thus motivating the exigencies for state estimation and feedback control.

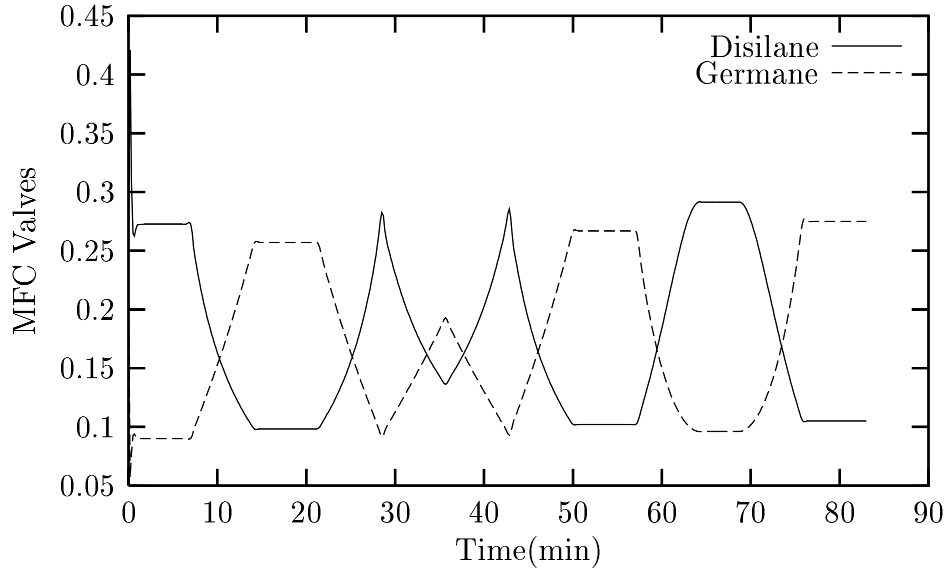

Figure 4.6: Model validation: Disilane and germane MFC valve positions

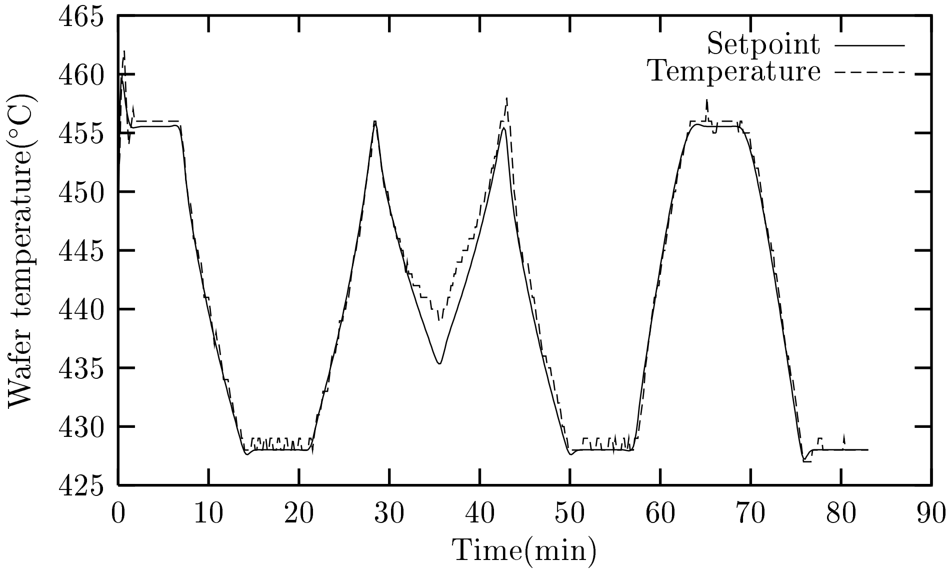

Figure 4.7: Model validation: Wafer temperature

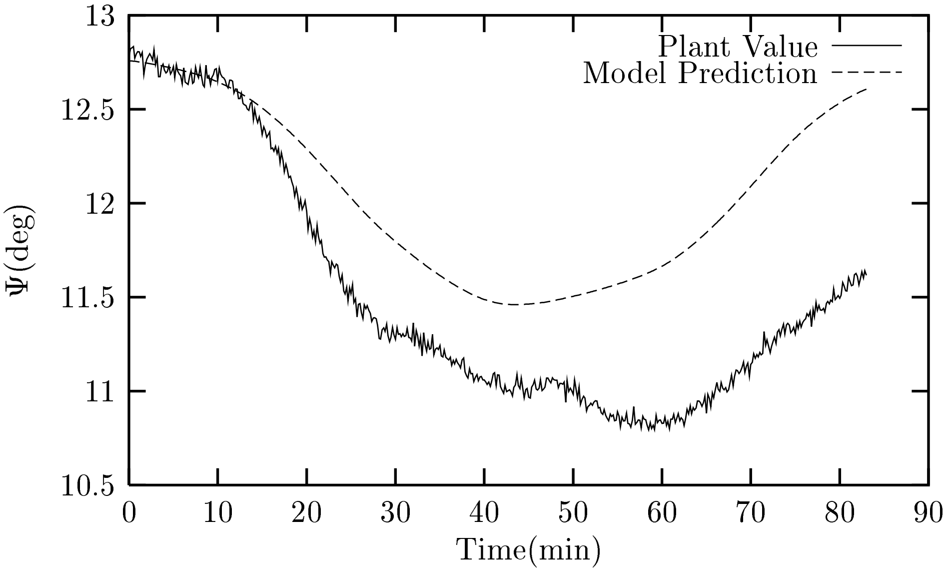

Figure 4.8: Model validation: Measured and predicted Ψ for $\lambda = 5520\text{Å}$

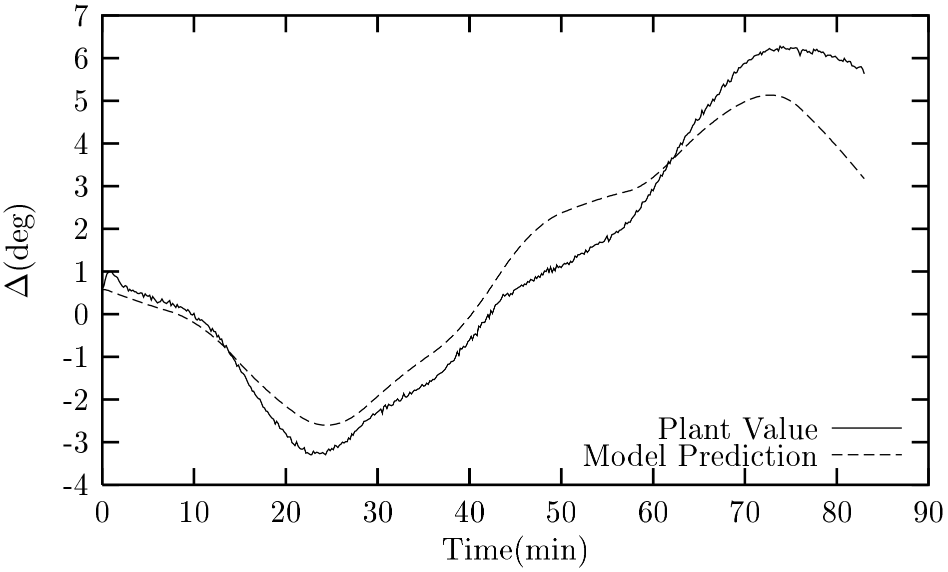

Figure 4.9: Model validation: Measured and predicted Δ for $\lambda = 5520\text{Å}$

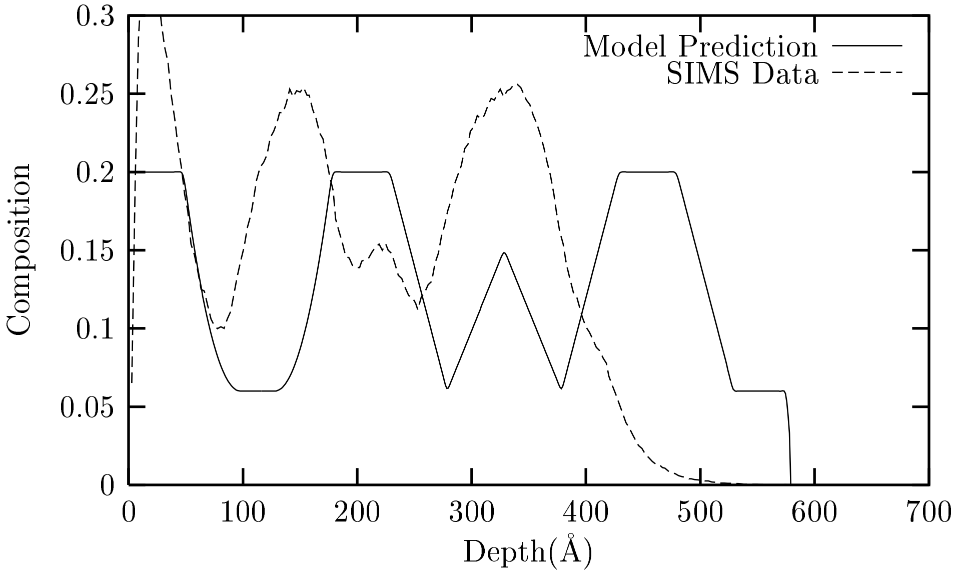

Figure 4.10: Model validation: Resulting film

Chapter 5

State Estimation

> *It is only the scholar who appreciates that all history consists of successive excursions from a single starting point, to which man returns again and again to organize yet another search for a durable scale of values*
>
> — Aldo Leopold, *A Sand County Almanac*

The feedback controller utilized in this work performs two separate functions, one of which is estimating the current value of system states $\mathbf{x}$ given an output measurement $\mathbf{y}$. The other function is regulation, which will be discussed in Chapter 6. Solving the estimation problem is the key step in the control of $\mathrm{Si}_{1-x}\mathrm{Ge}_x$ chemical vapor deposition because film composition and growth rate cannot be measured directly. They must be inferred from optical measurements. It is the task of the state estimator to infer, or reconstruct the system states by balancing the contribution made by the dynamic process model with that given by the measurement. In Section 5.1 a state disturbance model is presented and appended to the process models described in the previous chapter. The addition of a constant disturbance model to the state-space process model is used to obtain offset-free control. In Section 5.2 the extended Kalman filter(EKF) is presented. The filter counteracts the effects of measurement noise and provides a smooth estimate of the system states in real time. In order for state estimation to be effective the measurement outputs $\mathbf{y}$ must contain information about the states $\mathbf{x}$. In other words, the states $\mathbf{x}$ must be observable from the measurements $\mathbf{y}$. In Section 5.3 observability is defined and quantified. Finally, in Section 5.4 simulations are presented that demonstrate the effectiveness of the extended Kalman filter for various scenarios.

5.1 State Disturbance Model Formulation

A state disturbance model is employed to remove steady-state offset due to the mismatch between the model prediction and reality [54]. This mismatch or bias can arise from nonzero disturbances in process inputs, states, and outputs. A state disturbance model assumes that the error between the output measurement and the model's prediction of the output measurement is due to an integrated disturbance in one or more of the process states. For this work two state disturbances are employed. Integrating state disturbances are added to the germane MFC valve position and to the wafer temperature. The temperature disturbance accounts for the variation in the film growth rate. The disturbance added to the germane MFC valve position accounts for the variation in the film composition. The state disturbances are modeled as integrating white noise processes.

$$\mathbf{p}_{k+1} = \mathbf{p}_k + \boldsymbol{\xi}_k \tag{5.1}$$

By considering $\mathbf{p}$ to be a continuation of the state the process model can be written in discrete time as

$$\begin{aligned} \mathbf{x}_{k+1} &= \mathbf{f}(\mathbf{x}_k, \mathbf{u}_k, \mathbf{p}_k, k) + \boldsymbol{\omega}_k & (5.2) \\ \mathbf{y}_k &= \mathbf{g}(\mathbf{x}_k) + \boldsymbol{\nu}_k & (5.3) \\ \mathbf{z}_k &= \mathbf{h}(\mathbf{x}_k) & (5.4) \end{aligned}$$

where $\boldsymbol{\omega}$ and $\boldsymbol{\nu}$ are zero-mean Gaussian white noise variables with covariances $\mathbf{Q}_\omega$ and $\mathbf{R}_\nu$. Updating $\mathbf{p}_k$ given an output measurement $\mathbf{y}$ provides offset-free control [24, 54, 72]

5.2 Extended Kalman Filter

The state estimation problem is defined as finding the most likely value of the state given measured outputs and a dynamic process model. Estimation theory [48, 56] is presented as a problem of updating the conditional probability distribution $p(\mathbf{x}|\mathbf{y})$ for the variable $\mathbf{x}$ given measurements $\mathbf{y}$. The state variable $\mathbf{x}$ is governed by a dynamic differential equation, which was developed in Chapter 4. The outputs $\mathbf{y}$ are linear combinations of the states. In systems where all the random variables are normally distributed and the dynamics are linear, the density of the conditional probability distribution is also normal and can be updated according to equations that have the predictor-corrector structure of an observer, known as the Kalman filter. In systems described by non-linear differential equations, the conditional probability

$p(\mathbf{x}|\mathbf{y})$ cannot be readily determined. Approximations have therefore been developed. An approximate method for estimating states in non-linear systems is the extended Kalman filter(EKF) [18, 32, 44, 91].

Employing a Taylor series expansion [37], Equations 5.2 through 5.4 can be approximated as a linear, time–varying, discrete–time model as

$$\begin{aligned} \mathbf{x}_{k+1} &= \mathbf{f}(\hat{\mathbf{x}}_{k|k}, \mathbf{u}_k) + \mathbf{A}_k x_k + \mathbf{B}_k \mathbf{u}_k && (5.5) \\ \mathbf{y}_k &= \mathbf{g}(\hat{\mathbf{x}}_{k|k}) + \mathbf{C}_k^m \mathbf{x}_k && (5.6) \\ \mathbf{z}_k &= \mathbf{h}(\hat{\mathbf{x}}_{k|k}) + \mathbf{C}_k^c \mathbf{x}_k && (5.7) \\ & && (5.8) \end{aligned}$$

where $\hat{\mathbf{x}}_{k|k}$ is the estimate of the state at time k given measurements up to time k. The discrete process model Jacobians are defined as

$$\begin{aligned} \mathbf{A}_k &= \left.\frac{\partial \mathbf{f}(\mathbf{x}, \mathbf{u})}{\partial \mathbf{x}}\right|_{\mathbf{x}=\hat{\mathbf{x}}_{k|k}, \mathbf{u}=\mathbf{u}_k} && (5.9) \\ \mathbf{B}_k &= \left.\frac{\partial \mathbf{f}(\mathbf{x}, \mathbf{u})}{\partial \mathbf{u}}\right|_{\mathbf{x}=\hat{\mathbf{x}}_{k|k}, \mathbf{u}=\mathbf{u}_k} && (5.10) \\ \mathbf{C}_k^m &= \left.\frac{\partial \mathbf{g}(\mathbf{x})}{\partial \mathbf{x}}\right|_{\mathbf{x}=\hat{\mathbf{x}}_{k|k-1}, \mathbf{u}=\mathbf{u}_k} && (5.11) \\ \mathbf{C}_k^c &= \left.\frac{\partial \mathbf{h}(\mathbf{x})}{\partial \mathbf{x}}\right|_{\mathbf{x}=\hat{\mathbf{x}}_{k|k-1}, \mathbf{u}=\mathbf{u}_k} && (5.12) \end{aligned}$$

For this work, the Jacobians above are evaluated numerically using a centered finite–divide–difference approximation [20]. The optimal estimate of the state, $\hat{\mathbf{x}}$, is given by

$$\hat{\mathbf{x}}_{k|k} = \hat{\mathbf{x}}_{k|k-1} + \mathbf{K}_k(\mathbf{y}_k - \mathbf{g}(\hat{\mathbf{x}}_{k|k-1}, k)) \quad (5.13)$$

where $\hat{\mathbf{x}}_{k|k-1}$ and $\mathbf{g}(\hat{\mathbf{x}}_{k|k-1}, k)$ are the model predictions from Equations 5.2 and 5.3. The estimate error covariance matrix and the Kalman gain are updated as follows [36]

$$\begin{aligned} \hat{\mathbf{P}}_{k|k} &= (\mathbf{I} - \mathbf{K}_k \mathbf{C}_k^m)\, \hat{\mathbf{P}}_{k|k-1} && (5.14) \\ \hat{\mathbf{x}}_{k+1|k} &= \mathbf{f}(\hat{\mathbf{x}}_{k|k}, \mathbf{u}_k, k) && (5.15) \\ \hat{\mathbf{P}}_{k+1|k} &= \mathbf{A}_k \hat{\mathbf{P}}_{k|k} \mathbf{A}_k^T + \mathbf{Q}_\omega && (5.16) \\ \mathbf{K}_k &= \hat{\mathbf{P}}_{k|k-1} \mathbf{C}_k^{mT} \left(\mathbf{C}_k^m \hat{\mathbf{P}}_{k|k-1} \mathbf{C}_k^{mT} + \mathbf{R}_\nu \right)^{-1} && (5.17) \end{aligned}$$

The EKF algorithm consists of the following steps [101]:

1. Process the new output measurement $\mathbf{y}$ when it becomes available and correct the state covariance

$$\begin{aligned}\hat{\mathbf{x}}_{k|k} &= \hat{\mathbf{x}}_{k|k-1} + \mathbf{K}_k(\mathbf{y}_k - \mathbf{g}(\hat{\mathbf{x}}_{k|k-1}, k)) \\ \hat{\mathbf{P}}_{k|k} &= (\mathbf{I} - \mathbf{K}_k\mathbf{C}_k^m)\,\hat{\mathbf{P}}_{k|k-1}\end{aligned}$$

2. While waiting for the duration of the remaining sample interval, integrate the model and compute the predicted error covariance assuming that the input is constant over the sample interval

$$\begin{aligned}\mathbf{x}_{k+1|k} &= \mathbf{f}(\hat{\mathbf{x}}_{k|k}, \mathbf{u}_k) \\ \hat{\mathbf{P}}_{k+1|k} &= \mathbf{A}_k\hat{\mathbf{P}}_{k|k}\mathbf{A}_k^T + \mathbf{Q}_\omega\end{aligned}$$

3. Compute the Kalman gain

$$\mathbf{K}_{k+1} = \hat{\mathbf{P}}_{k+1|k}\mathbf{C}_{k+1}^{mT}\left(\mathbf{C}_{k+1}^m\hat{\mathbf{P}}_{k+1|k}\mathbf{C}_{k+1}^{mT} + \mathbf{R}_\nu\right)^{-1}$$

4. At the end of the sample interval, increment the time counter and go back to step 1.

The estimator is tuned by adjustment of the process noise covariance matrix, $\mathbf{Q}_\omega$. Given an estimate of the system states, the film growth rate and film composition can be inferred from Equation 5.4.

$$\mathbf{z}_{k|k} = \mathbf{h}(\hat{\mathbf{x}}_{k|k}) \tag{5.18}$$

It is the job of the regulator, which is developed in Chapter 6, to drive these growth rates and compositions to their desired targets.

5.3 Observability

In order for state estimation to be effective the measurement outputs $\mathbf{y}$ must contain information about the states $\mathbf{x}$. In other words, the states $\mathbf{x}$ must be observable from the measurements $\mathbf{y}$. A system is observable when it is possible to establish, in a finite interval of time, the time history of the states $\mathbf{x}$ given the time history of the measurement vector $\mathbf{y}$ over the same interval. For a general, time-varying system, the following test determines whether a system is observable [54].

Theorem 5.1 *The linear discrete-time system*

$$\mathbf{x}_{k+1} = \mathbf{A}_k \mathbf{x}_k \tag{5.19}$$

$$\mathbf{y}_k = \mathbf{C}_k^m \mathbf{x}_k \tag{5.20}$$

is completely observable if and only if the observability Grammian matrix

$$\mathbf{M}_d = \sum_{i=1}^{N} \Phi^T(i,0)\mathbf{C}^{mT}(i)\mathbf{C}^m(i)\Phi(i,0) \tag{5.21}$$

is positive definite for some $N > 0$, where $\Phi(i,0)$ is the state transition matrix

$$\begin{aligned} \Phi(i,0) &= \mathbf{A}(i)\mathbf{A}(i-1)\cdots\mathbf{A}(1), \\ i &= 1,\ldots,N \end{aligned} \tag{5.22}$$

A proof of this theorem is given by Meditch [64]. The observability of a certain state can be quantified by examining the singular values of the observability Grammian. Employing a singular value decomposition [42] the observability Grammian can be factored as

$$\mathbf{M}_d = \mathbf{U}\Sigma\mathbf{U}^T \tag{5.23}$$

where Σ is the matrix of singular values and the columns of $\mathbf{U}$ are the singular vectors of $\mathbf{M}_d$. Each singular value in Σ is scaled by the largest value and the ratio is compared to a tolerance. The number of scaled singular values that are greater than the tolerance are the number of observable modes. The columns of $\mathbf{U}$ that correspond to the retained singular values map the state vector to the observable subspace. Thus, the amount of information an observable mode contains about a certain state can be quantified by calculating the norm of the columns of $\mathbf{U}^T$.

5.4 Simulations

In this section simulations are presented that demonstrate the effectiveness of the extended Kalman filter for various scenarios. The plant is represented by numerical solution of the full non-linear model given the sequence of manipulated inputs. For each scenario the same manipulated variable sequence is used. The MFC valve positions for disilane and germane are shown in Figure 5.1. The substrate temperature is shown in Figure 5.2. The reactor pressure is held constant at 26 mTorr for the entire simulation.

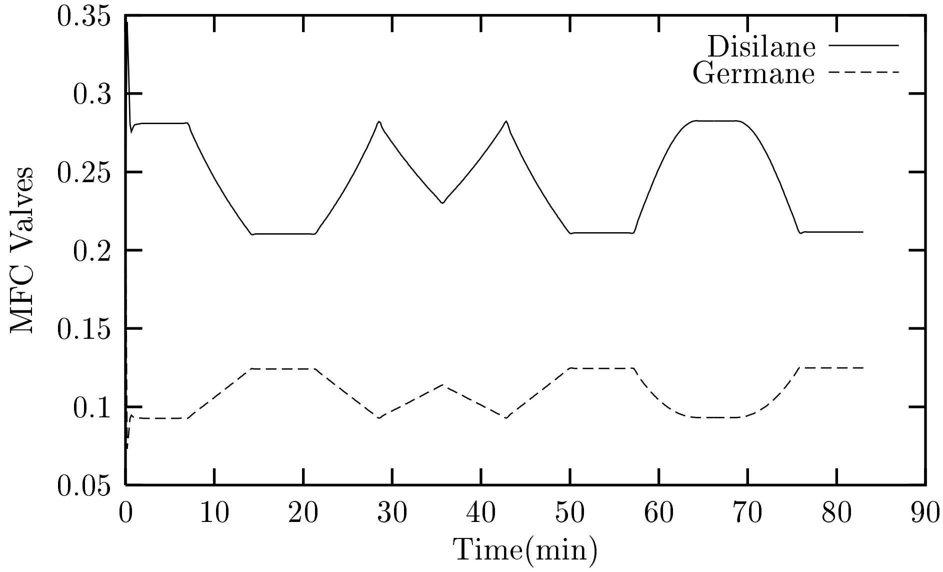

Figure 5.1: Disilane and germane MFC valve positions

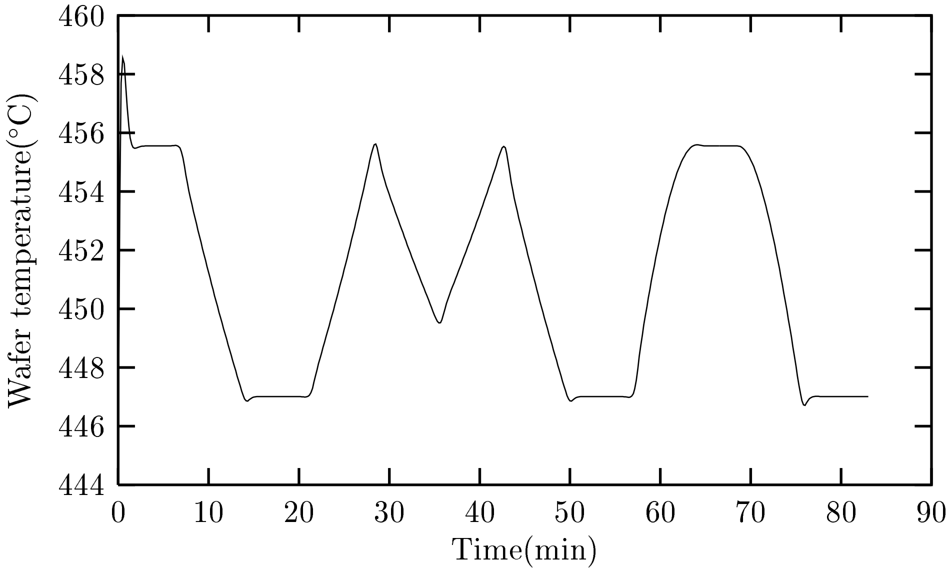

Figure 5.2: Wafer temperature

5.4.1 Case number 1

The EKF is first tested for the case where there is no mismatch between the plant and the model. The plant response is predicted perfectly with the model. However, the plant measurement is corrupted with noise. Figures 5.3 and 5.4 show measured and predicted values of Δ for $\lambda = 3000$Å and $\lambda = 5520$Å. The estimator filters out the measurement noise and provides a smooth estimate of Δ. The filter also reconstructs the system states and as a result infers the film growth rate and composition, which are shown in Figures 5.5 and 5.7. The resulting film profile is shown in Figure 5.8.

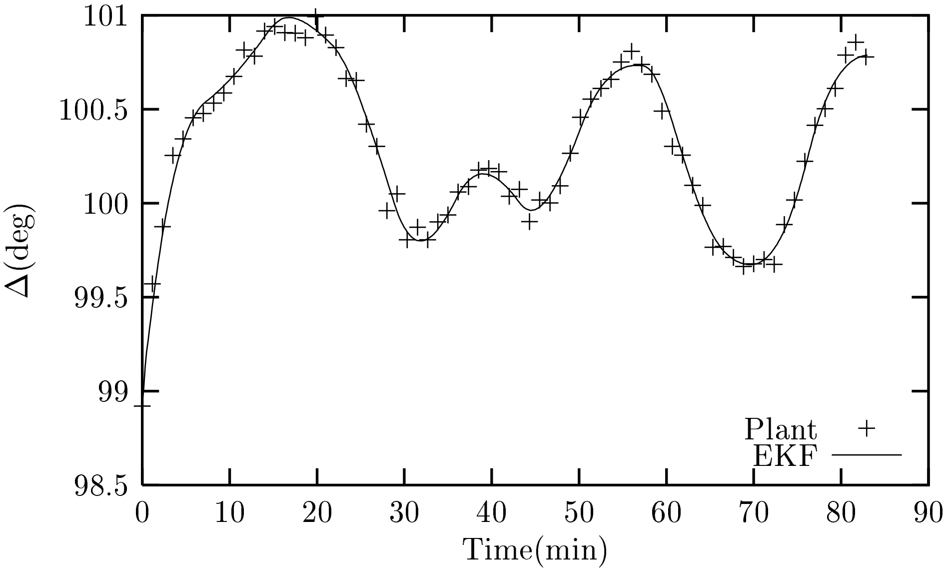

Figure 5.3: Case 1: Δ for $\lambda = 3000$Å

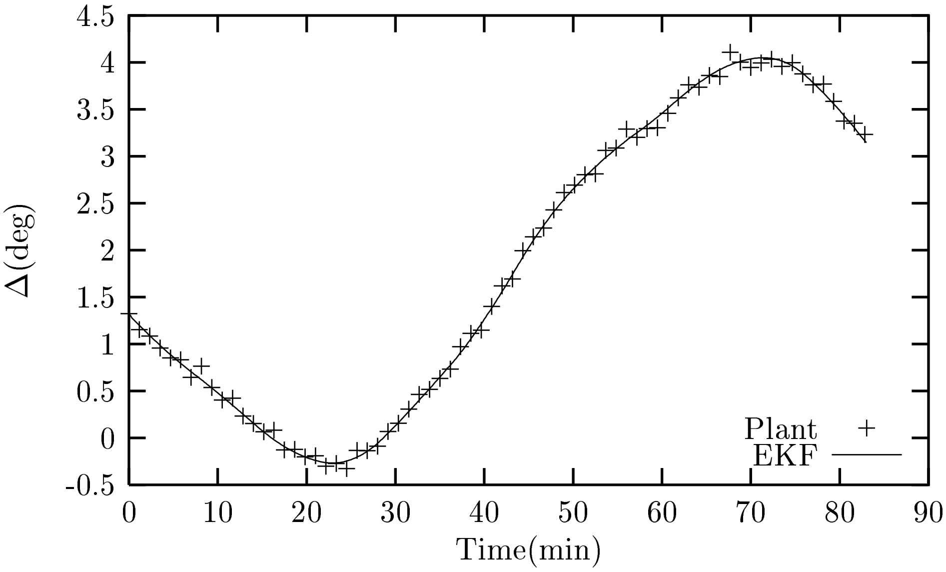

Figure 5.4: Case 1: Δ for $\lambda = 5520$Å

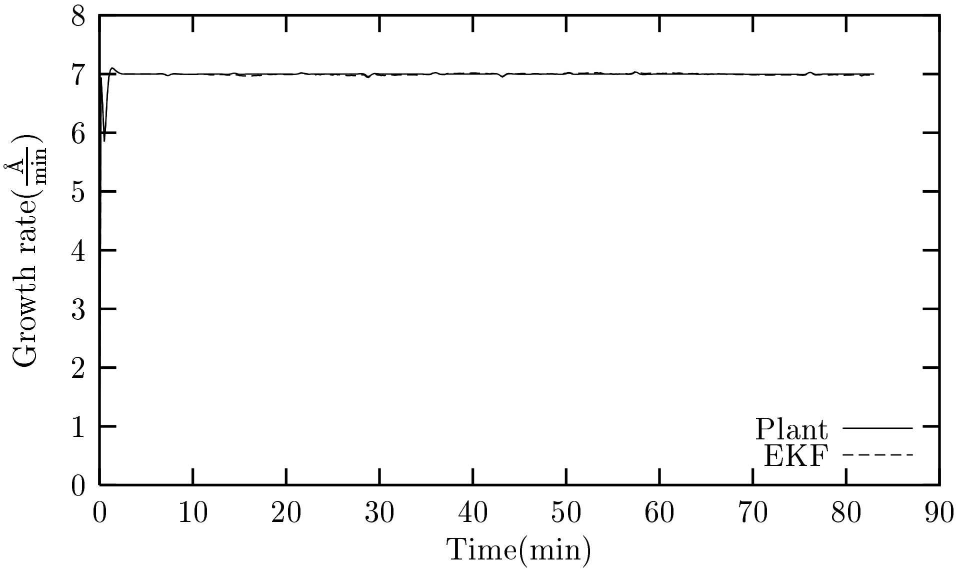

Figure 5.5: Case 1: Film growth rate

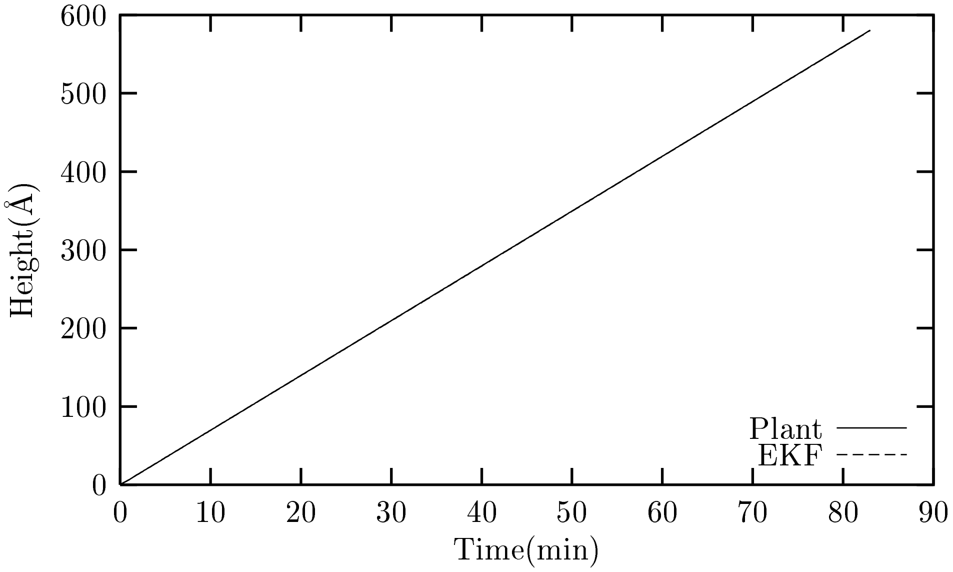

Figure 5.6: Case 1: Film height

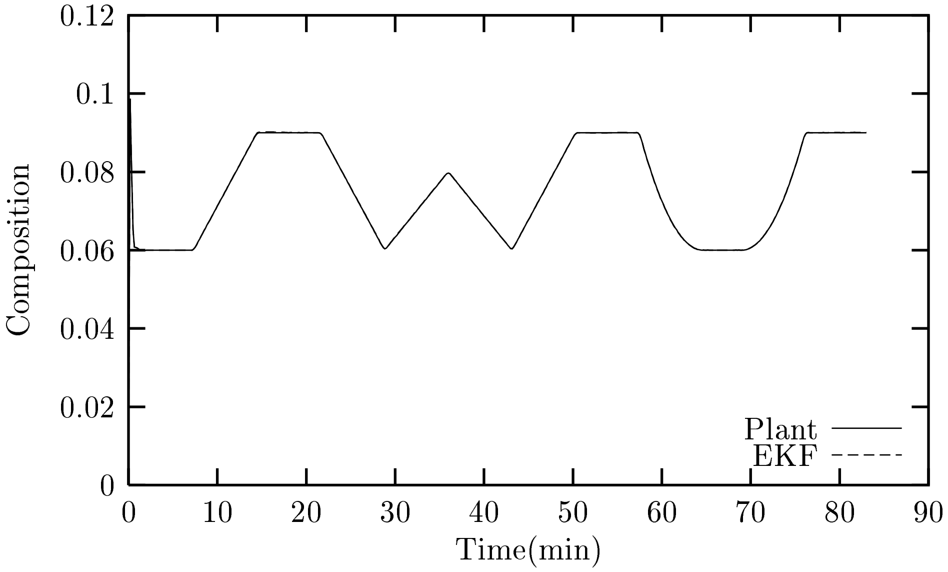

Figure 5.7: Case 1: Film composition

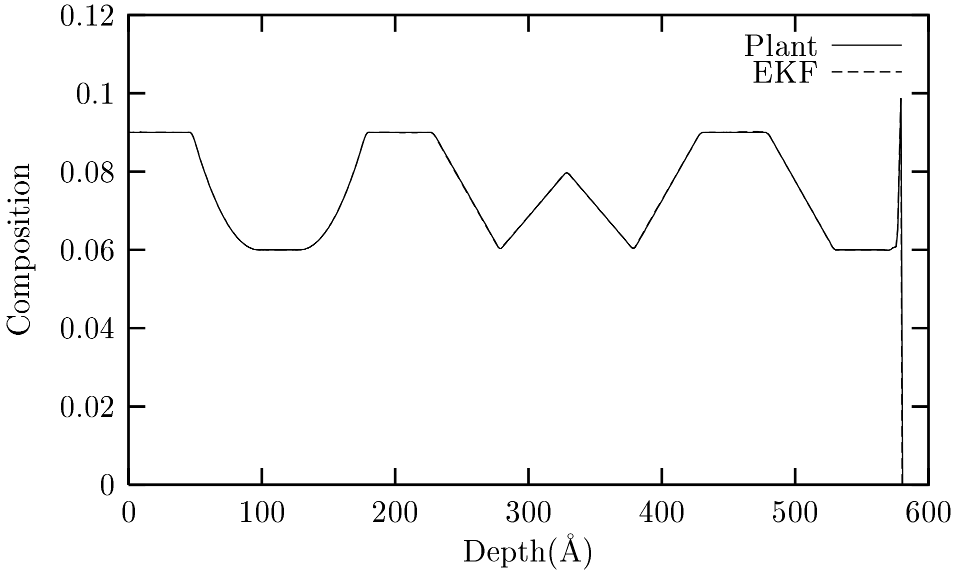

Figure 5.8: Case 1: Resulting film profile

5.4.2 Case number 2

This set of simulations demonstrates the effectiveness of the EKF when there is mismatch between the plant and the model prediction of the plant. The mismatch in this case is as follows:

- The germane MFC valve position is open 0.1 more than expected
- The temperature of the wafer is 10 degrees hotter than expected

Figures 5.9 and 5.10 show the first six minutes of the measured and estimated values of Δ for $\lambda = 3000\text{Å}$ and $\lambda = 5520\text{Å}$. The open–loop model predictions of Δ are plotted as well. The EKF estimates of Δ converge to the plant value within two minutes. The estimates of the disturbance states are shown in Figures 5.11 and 5.12. The Kalman filter succeeds in pinpointing the unmeasured disturbances and correcting them. The state disturbance estimates converge to the mismatch values that were invented and consequently, the inferred values of film growth rate and composition converge to the respective plant values, as shown in Figures 5.13 and 5.14. The open-loop model prediction of film growth rate and composition are also plotted. The EKF estimates track the open–loop responses for about one minute, at which time enough output data has been collected for the estimator to infer the disturbance states. The EKF estimate and the plant value of film height are plotted in Figure 5.15. Note that the estimate of the film height never converges to the plant value. It is not possible to infer film height from the ellipsometric measurements. Thus, any error in film height is not detected by the ellipsometer. Referring to the model developed in Chapter 4 and especially Equation 4.71, it is evident that the ellipsometric output Δ is a function of the film growth rate and *not* a function of film height. In other words film height is unobservable.

Figures 5.16 and 5.17 show the measured and estimated values of Δ for $\lambda = 3000\text{Å}$ and $\lambda = 5520\text{Å}$ for the entire simulation. The EKF estimates of Δ converge to and track the plant values for the entire simulation. The figures also show the open–loop model prediction of Δ for both wavelengths. The mismatch between the open–loop model prediction and the plant response shows up prominently in Δ.

As mentioned previously, the success of the estimator depends on the ability of the output measurement to carry information about the system states. Recall that the norm of the columns of $\mathbf{U}^T$ quantifies the amount of information an observable mode contains about a certain state. This norm of the columns of $\mathbf{U}^T$ is referred to as observability. The observability of film height as well as the observability of the two state disturbances are plotted in Figure 5.18. The figure shows that the observability of film height is identically zero during the entire simulation. The germane

MFC state disturbance is completely observable. However, the wafer temperature state disturbance is not nearly as observable. The measured output Δ oscillates with a period proportional to the film growth rate, which is strongly affected by wafer temperature, producing a classical optical interference pattern. Thus, as Δ cycles through its first period, the observability of wafer temperature increases, and ultimately the growth rate can be inferred. However, as Δ passes through its amplitude it carries no information about the film growth rate and consequently the observability of the wafer temperature state disturbance decreases. The discontinuities in the plotted observability occur when another mode becomes observable or unobservable when compared to the observability tolerance.

Figures 5.19 and 5.20 show the EKF estimates of film growth rate and composition for the entire simulation. The EKF estimates of Δ converge to and track the plant values for the entire simulation and consequently film growth rate and composition also converge to their respective plant values.

Figures 5.21 and 5.22 show the Kalman filter gains during the course of the simulation. The Kalman gains corresponding to the higher wavelength value of Δ oscillate much more than those corresponding to the smaller wavelength. The larger wavelength Kalman gain also becomes zero temporarily during the run. As mentioned earlier, the measured output oscillates, producing a classical optical interference pattern. As Δ passes through its maximum amplitude the Kalman gain becomes zero and temporarily there is no feedback. The Kalman gain for the larger wavelength also changes sign, reflecting the change in phase of the reflected light.

The resulting film profiles for this simulation are shown in Figure 5.23. There is large disagreement between the open–loop model prediction and the plant value because of the unmodelled disturbances. The model predicted a film that has a lower germanium composition and is about 50% thinner than the plant value. In contrast the EKF pinpoints the state disturbances and corrects them, utilizing feedback from the ellipsometric measurements. As a result, the EKF estimate of the film profile converges to the actual value.

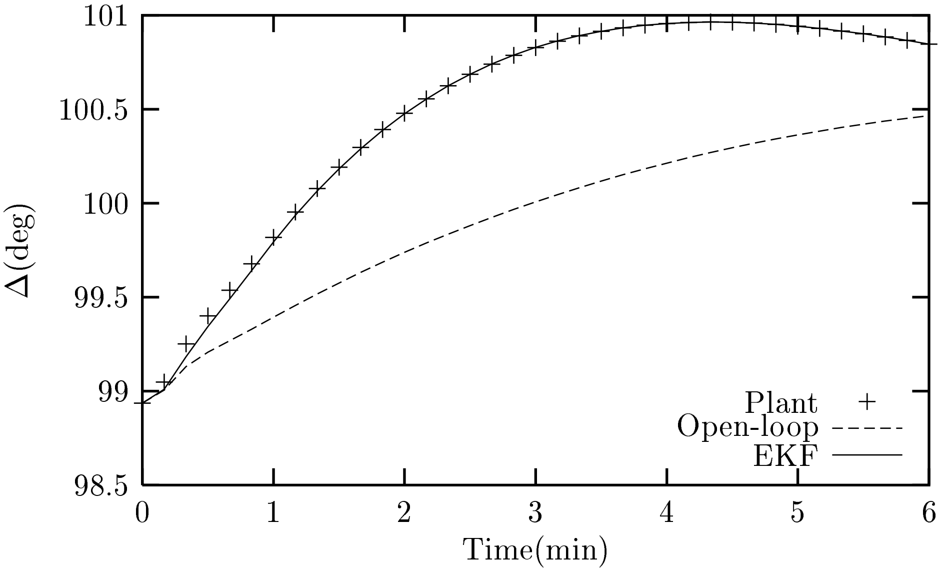

Figure 5.9: Case 2: Δ for $\lambda = 3000$Å

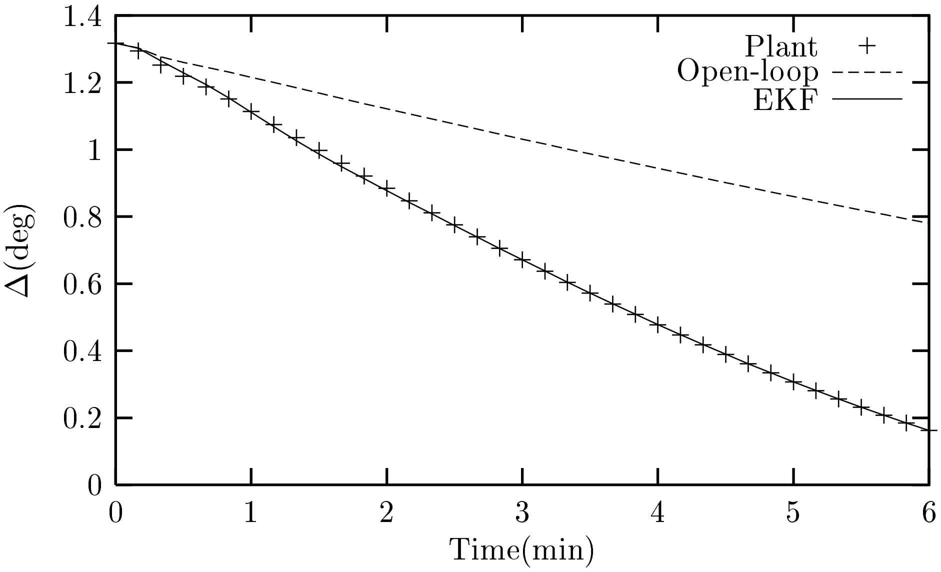

Figure 5.10: Case 2: Δ for $\lambda = 5520$Å

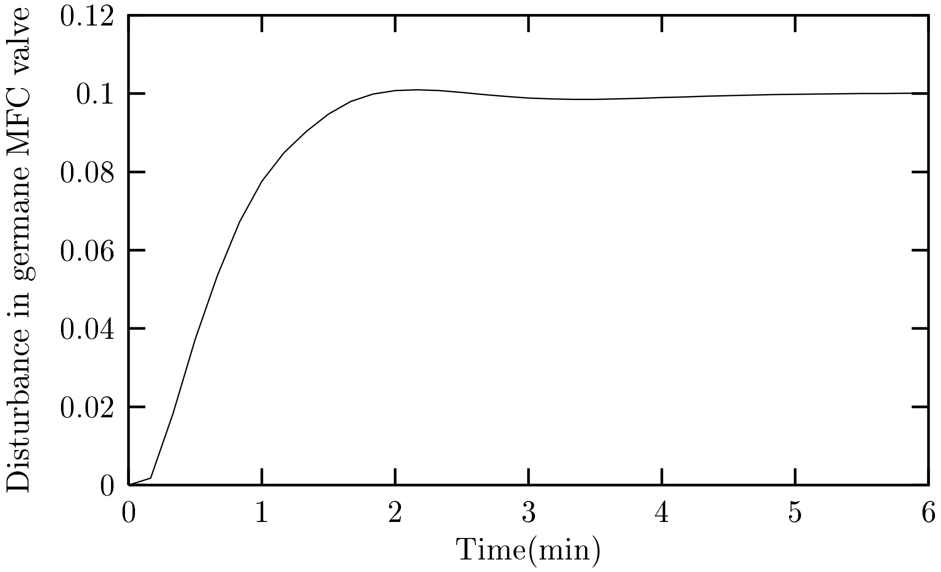

Figure 5.11: Case 2: State disturbance in the germane MFC valve

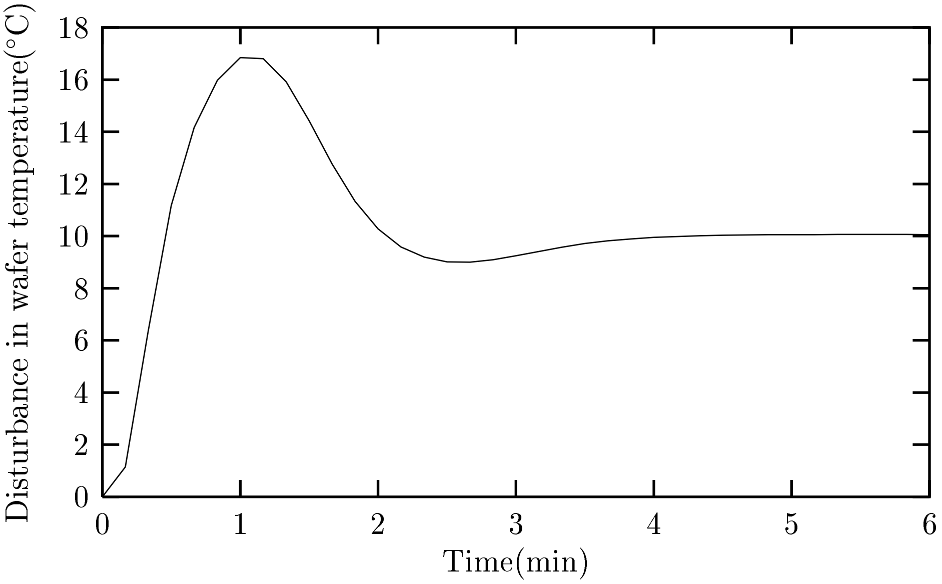

Figure 5.12: Case 2: State disturbance in wafer temperature

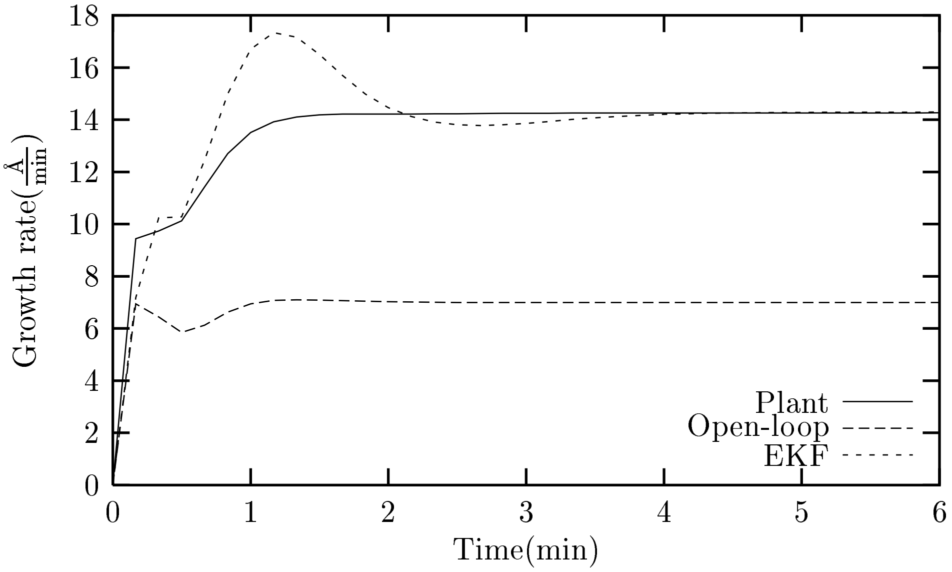

Figure 5.13: Case 2: Film growth rate

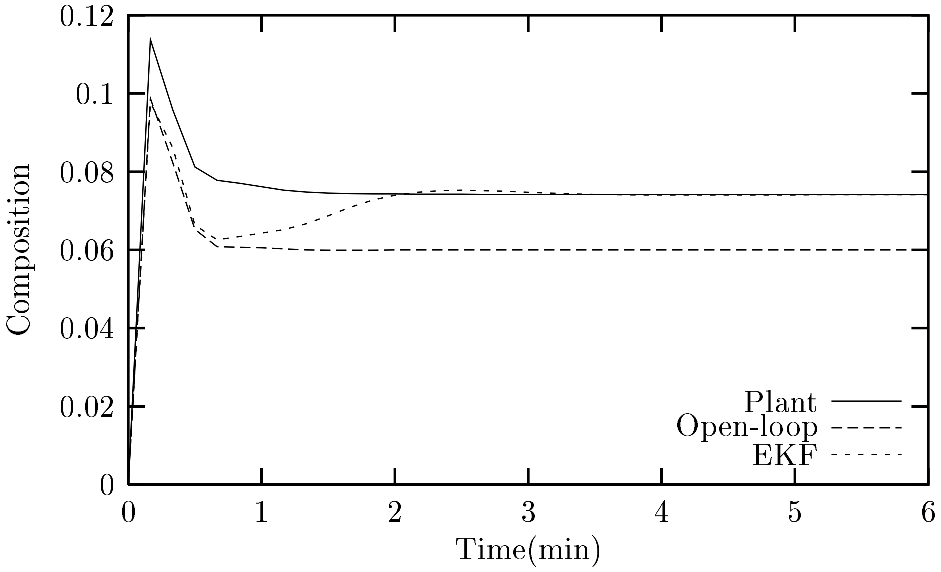

Figure 5.14: Case 2: Film composition

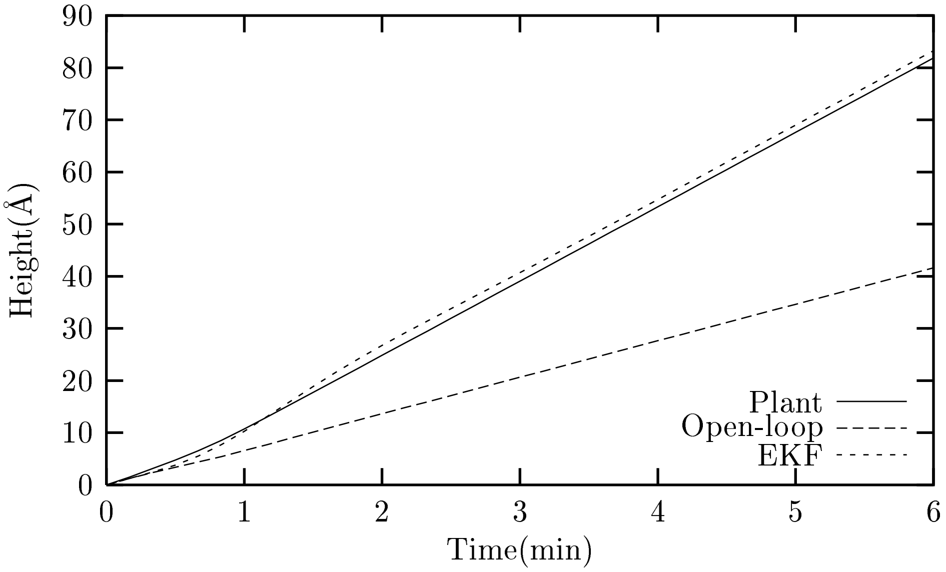

Figure 5.15: Case 2: Film height

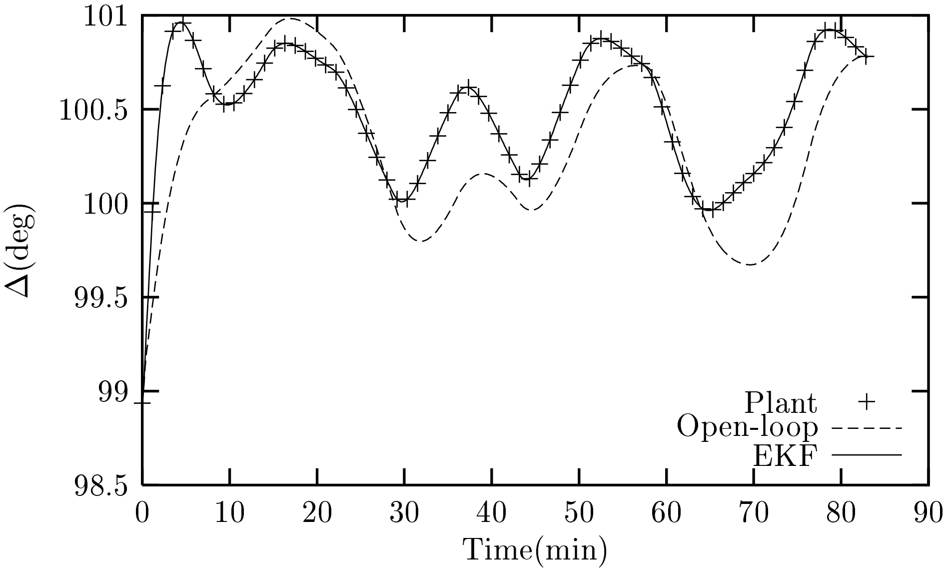

Figure 5.16: Case 2: Δ for $\lambda = 3000$Å

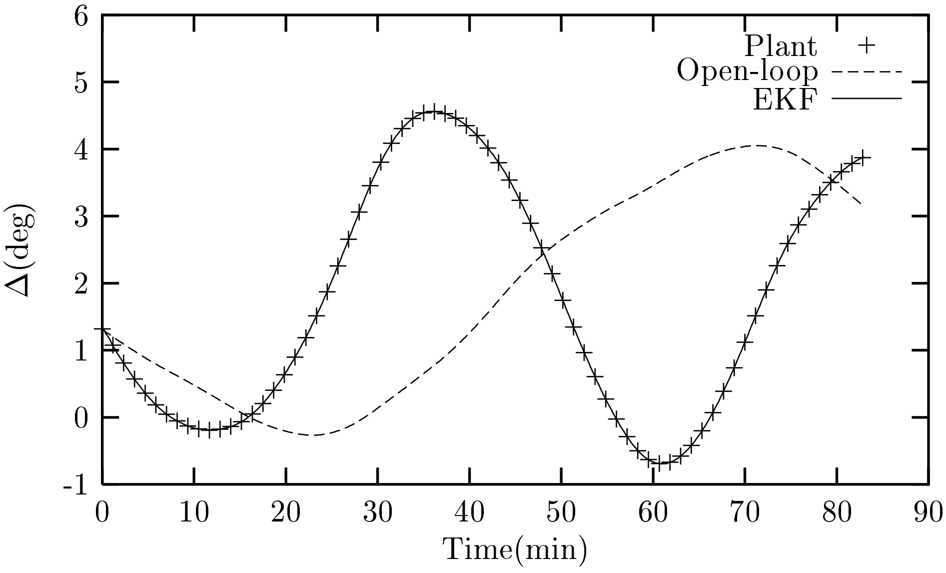

Figure 5.17: Case 2: Δ for $\lambda = 5520$Å

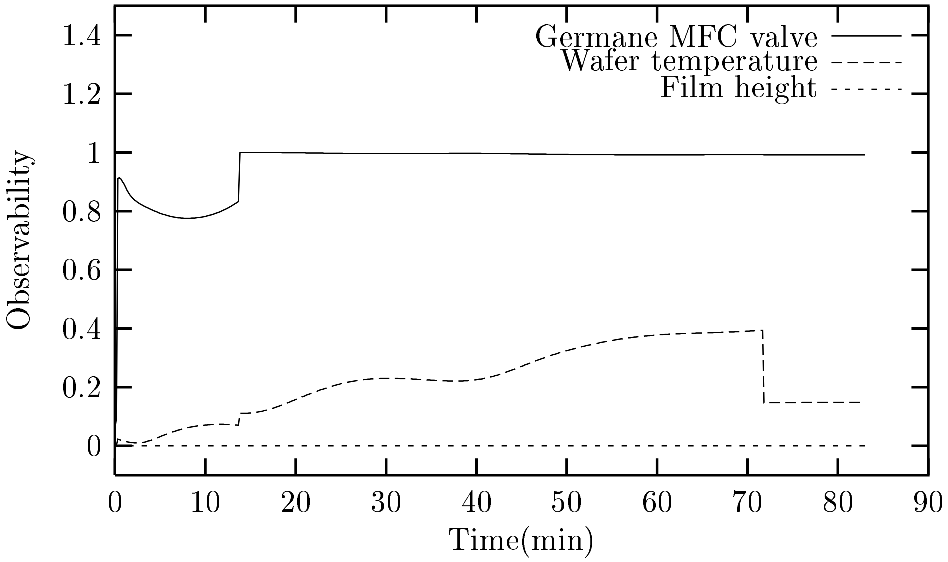

Figure 5.18: Case 2: Observability of the film height and the state disturbances

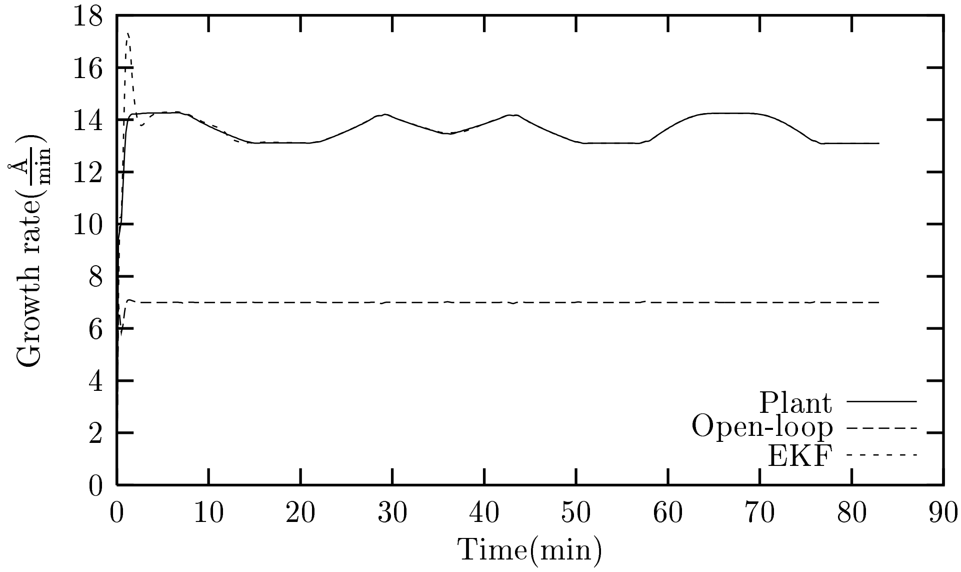

Figure 5.19: Case 2: Film growth rate

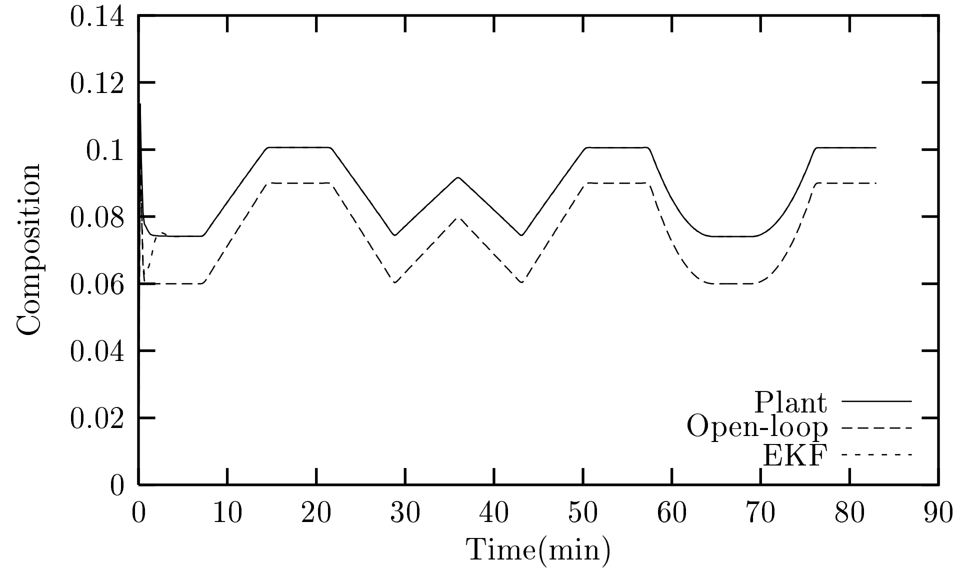

Figure 5.20: Case 2: Film composition

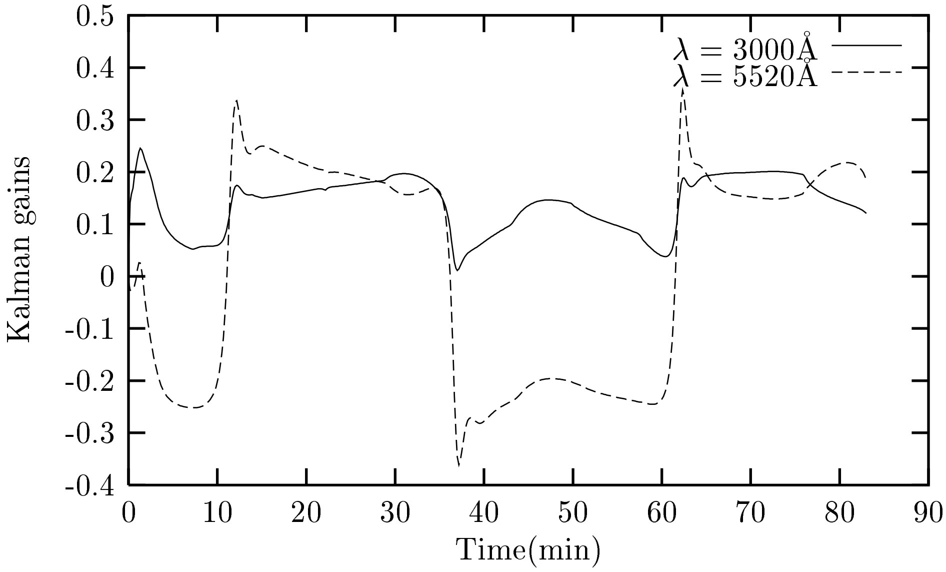

Figure 5.21: Case 2: Kalman filter gains for the germane MFC valve disturbance state

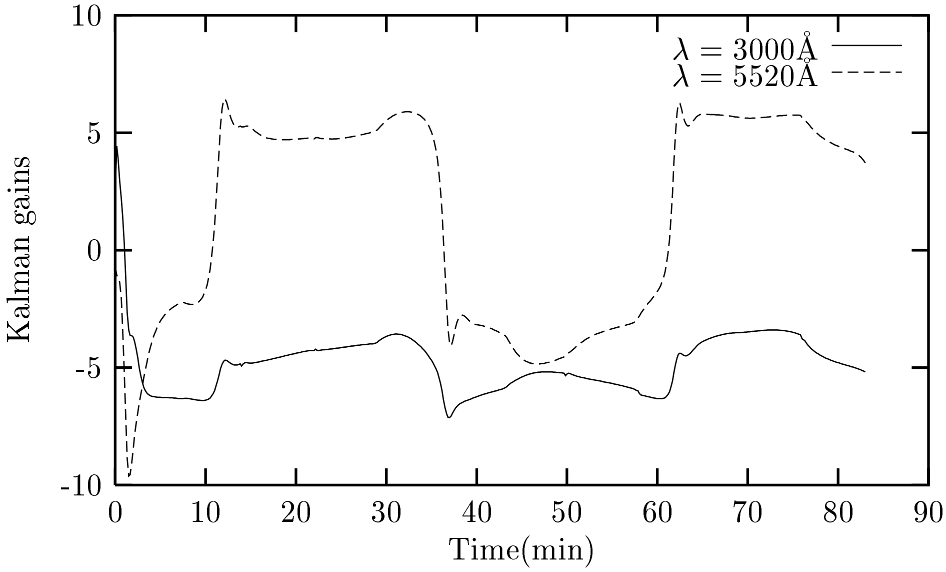

Figure 5.22: Case 2: Kalman filter gains for the wafer temperature disturbance state

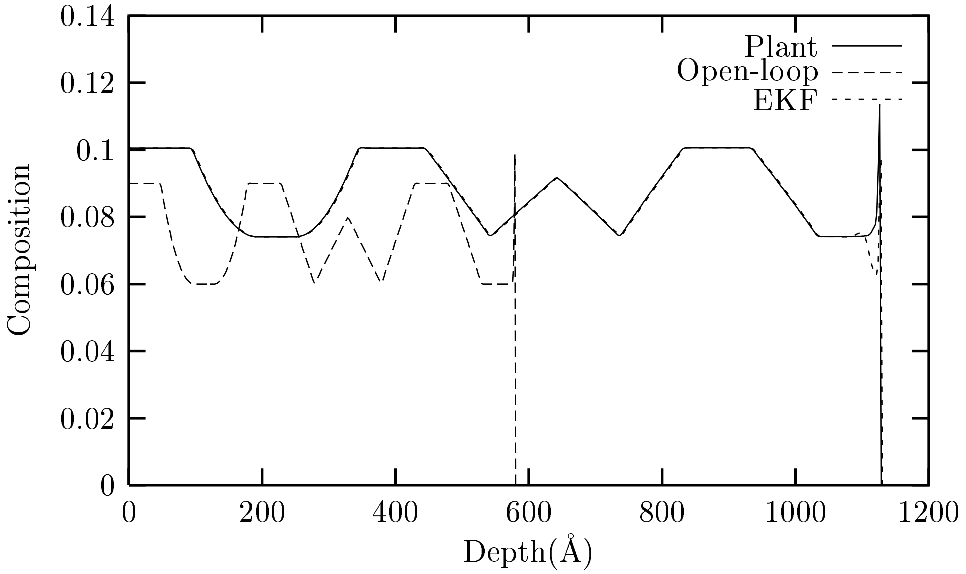

Figure 5.23: Case 2: Resulting film profile

5.4.3 Case number 3

This simulation demonstrates the effectiveness of the EKF for a more general, less transparent case of plant–model mismatch. In this case the kinetic mechanism does not represent the plant correctly. This mismatch scenario is simulated by placing a mismatch in the kinetic parameter k_7. The model value for the parameter k_7 is set 50% larger than the plant value.

Figures 5.24 and 5.25 show the first six minutes of the measured and estimated values of Δ for $\lambda = 3000$Å and $\lambda = 5520$Å. The open–loop model prediction of Δ is plotted as well. The Kalman filter detects a deviation between the predicted value of Δ and the measured plant value. The filter rationalizes that this error between the measured and predicted output is caused by unmeasured disturbances in the MFC germane valve and wafer temperature and updates those states. The estimates of the disturbance states are shown in Figures 5.26 and 5.27. The kinetic mismatch is essentially modeled as unmeasured disturbances in the MFC germane valve and the wafer temperature. As a result the EKF estimates of Δ converge to the plant value within six minutes and consequently the inferred values of film growth rate and composition converge to the respective plant values, as shown in Figures 5.28 and 5.29. The EKF estimate and the plant value of film height are plotted in Figure 5.30. As pointed out in the previous simulation, the estimate of the film height never converges to the plant value. Film height is unobservable and any offset incurred at the beginning of the simulation, when the EKF did not have a sufficient amount of data to provide an estimate, cannot be removed by the estimator.

Figures 5.31 and 5.32 show the measured and estimated values of Δ for $\lambda =$ 3000Å and $\lambda = 5520$Å for the entire simulation. The EKF estimates of Δ converge to and track the plant values for the entire simulation. The figures also show the open–loop model prediction of Δ for both wavelengths. The mismatch between the model prediction and the plant response shows up prominently in the output Δ. The observability of film height as well as the observability of the two state disturbances are plotted in Figure 5.33. The figure shows that the observability of film height is again identically zero during the entire simulation. The germane MFC state disturbance is completely observable. The wafer temperature state disturbance is nearly unobservable at the beginning of the simulation. However, as more data is taken from the higher wavelength sensor, the observability of the wafer temperature disturbance increases and ultimately the state can be inferred. Figures 5.34 and 5.35 show the EKF estimates of film growth rate and composition for the entire simulation. The EKF estimates of Δ converge to and track the plant values for the entire simulation and as a consequence, the film growth rate and composition also converge to their respective plant values.

Figures 5.36 and 5.37 show the Kalman filter gains during the course of the simulation. The Kalman gains corresponding to the larger wavelength value of Δ oscillate much more than those corresponding to the lower wavelength and temporarily become zero during the run.

The resulting film profiles for this simulation are shown in Figure 5.38. There is large disagreement between the open–loop model prediction and the plant value. The model predicts a film that has a lower germanium composition and is about 200Å thicker than the plant value. In contrast, the EKF detects an unmeasured error and models it as disturbances in the MFC germane valve position and the wafer temperature. As a result the EKF estimate of the film profile converges to the actual value.

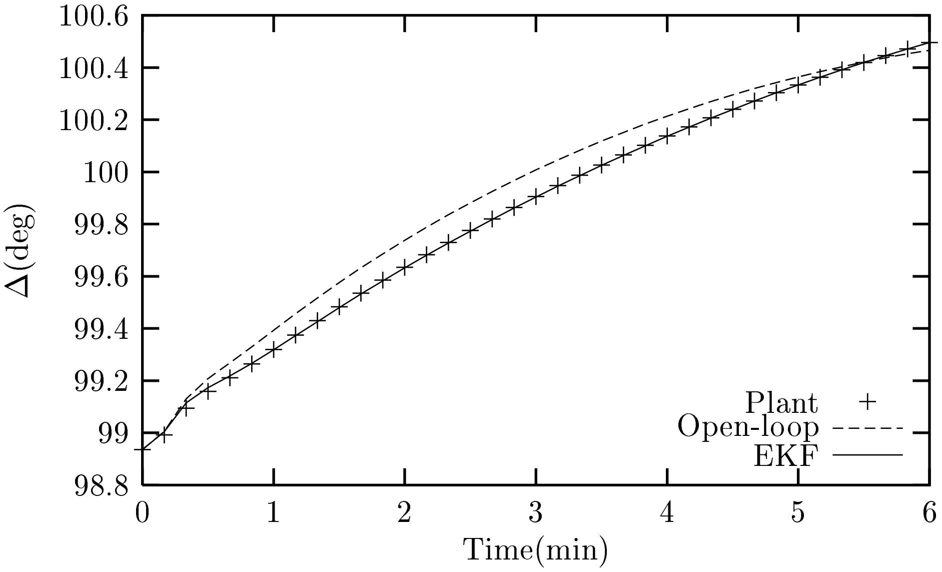

Figure 5.24: Case 3: Δ for $\lambda = 3000$Å

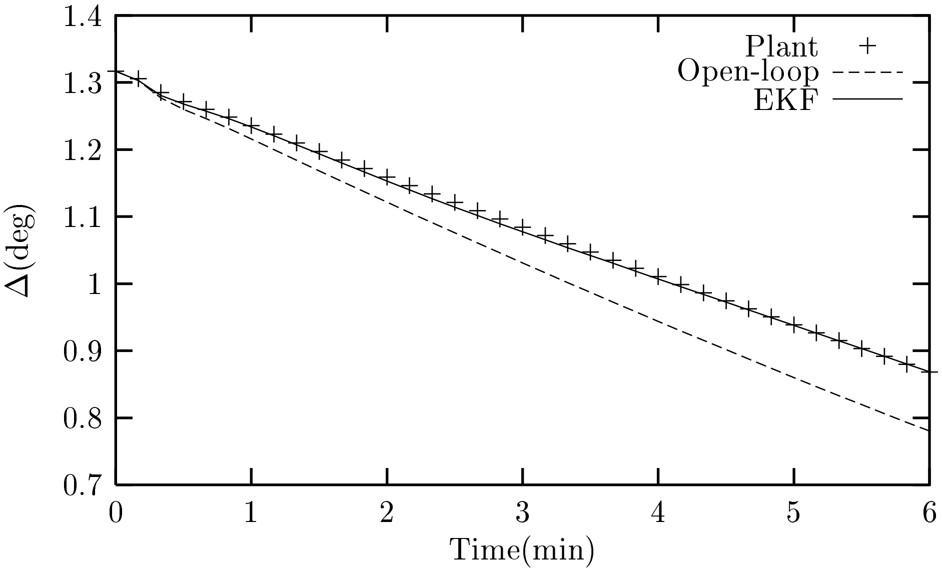

Figure 5.25: Case 3: Δ for $\lambda = 5520$Å

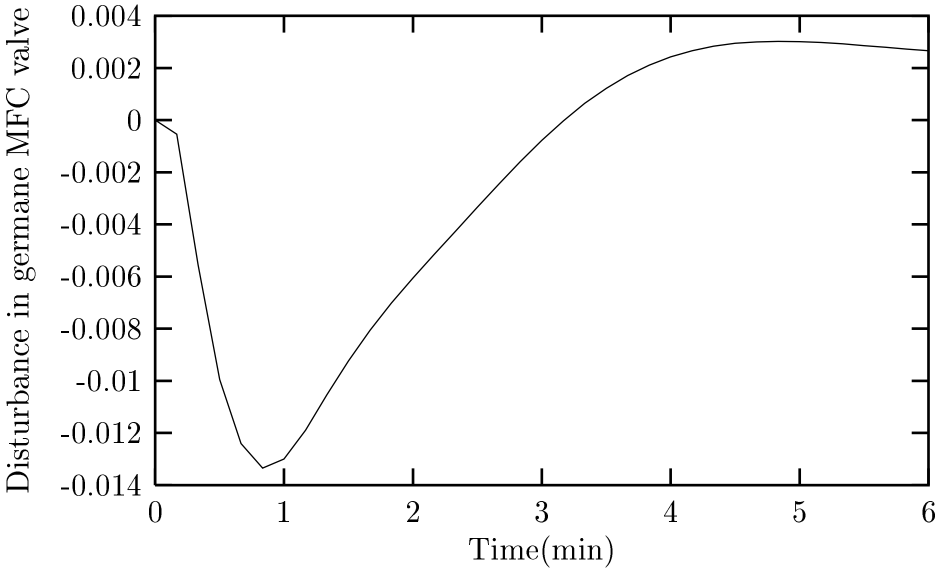

Figure 5.26: Case 3: State disturbance in the germane MFC valve

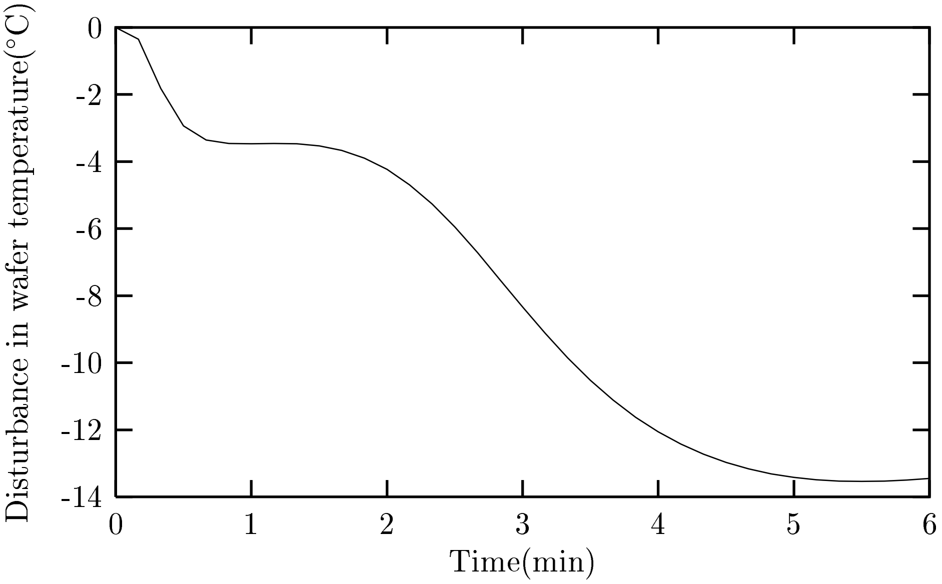

Figure 5.27: Case 3: State disturbance in wafer temperature

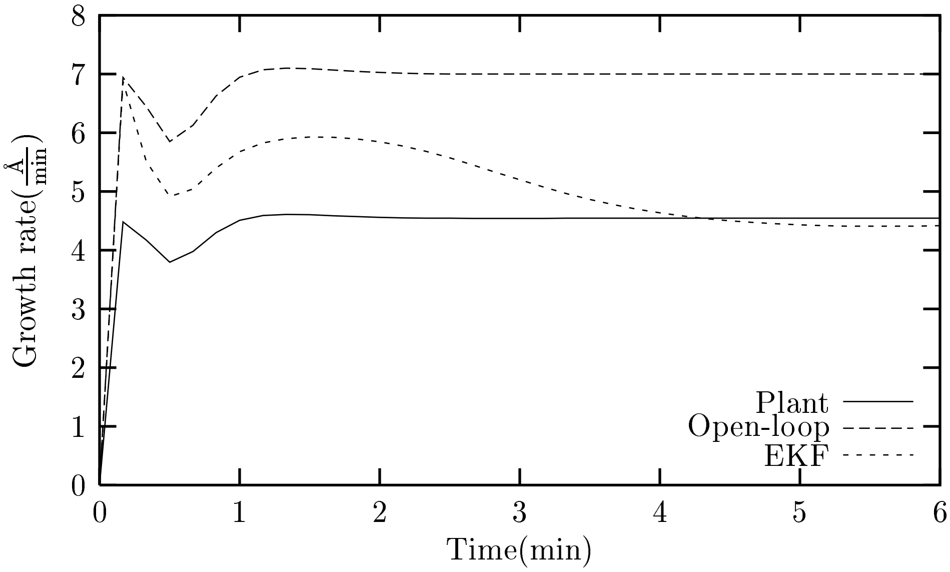

Figure 5.28: Case 3: Film growth rate

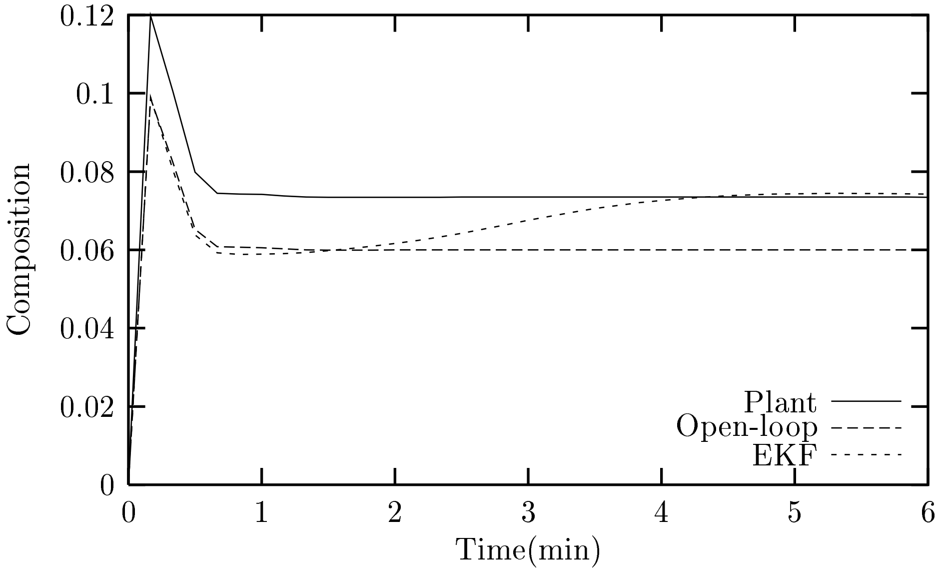

Figure 5.29: Case 3: Film composition

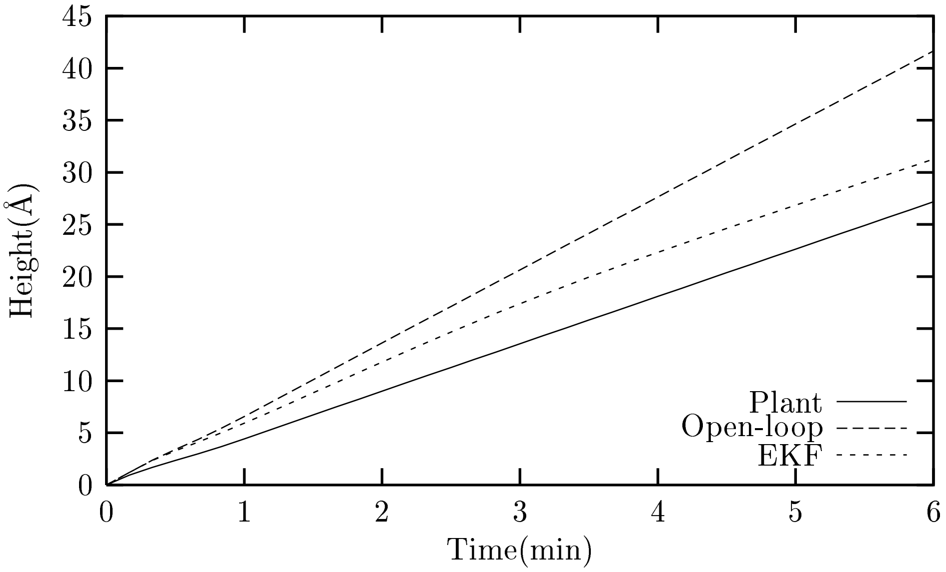

Figure 5.30: Case 3: Film height

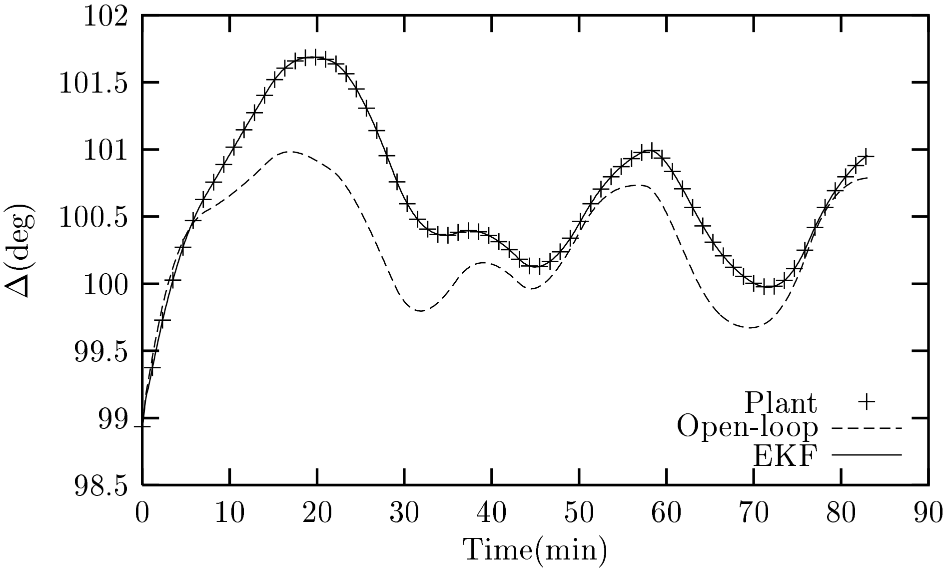

Figure 5.31: Case 3: Δ for $\lambda = 3000$Å

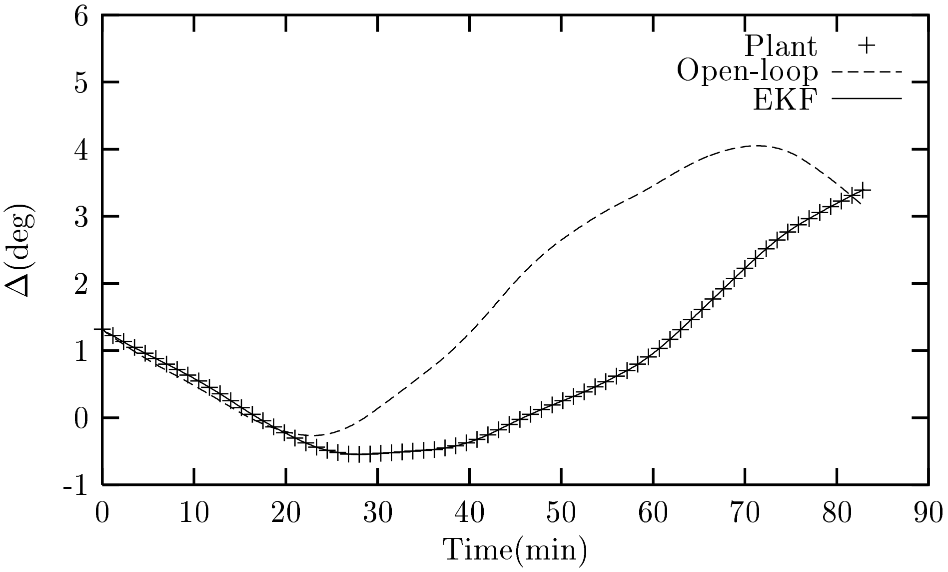

Figure 5.32: Case 3: Δ for $\lambda = 5520$Å

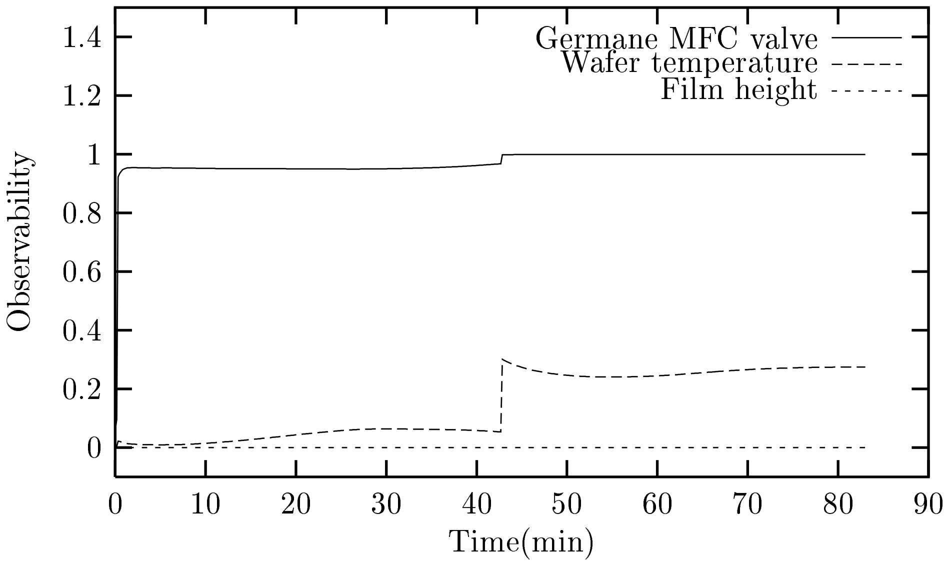

Figure 5.33: Case 3: Observability of the film height and the state disturbances

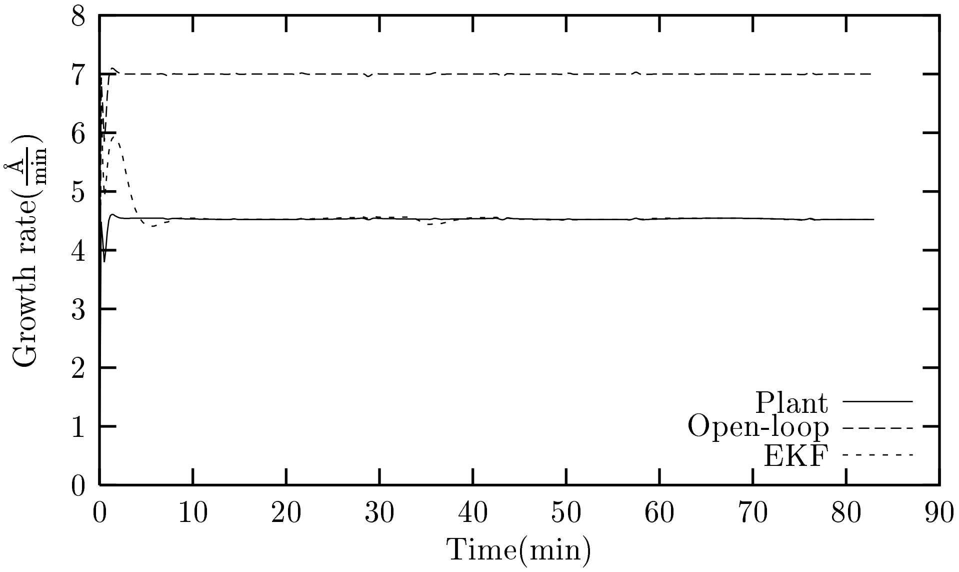

Figure 5.34: Case 3: Film growth rate

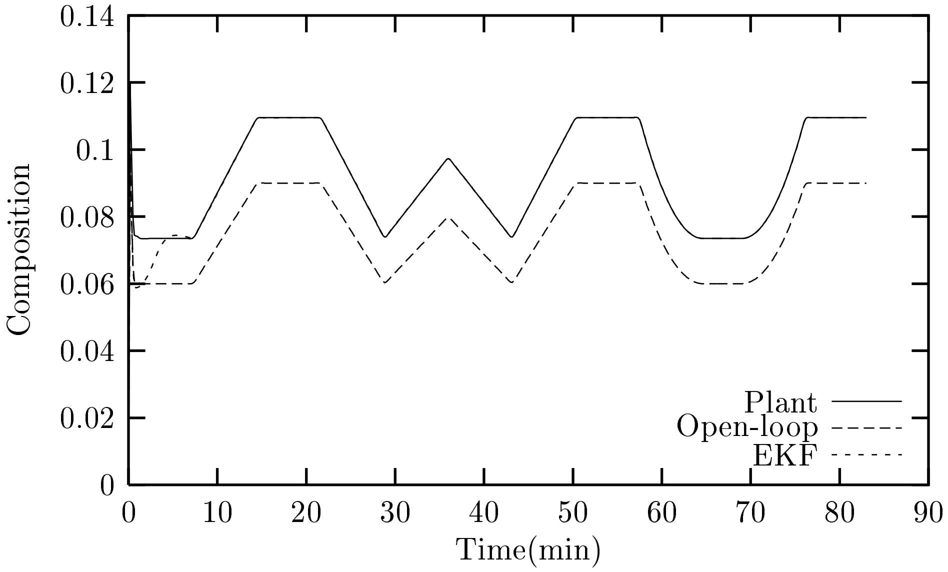

Figure 5.35: Case 3: Film composition

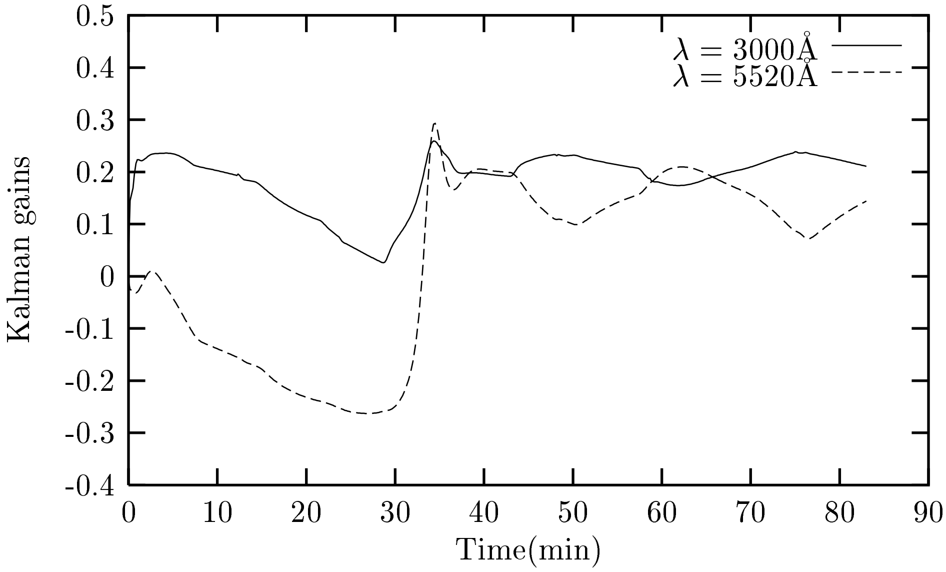

Figure 5.36: Case 3: Kalman filter gains for the germane MFC valve disturbance state

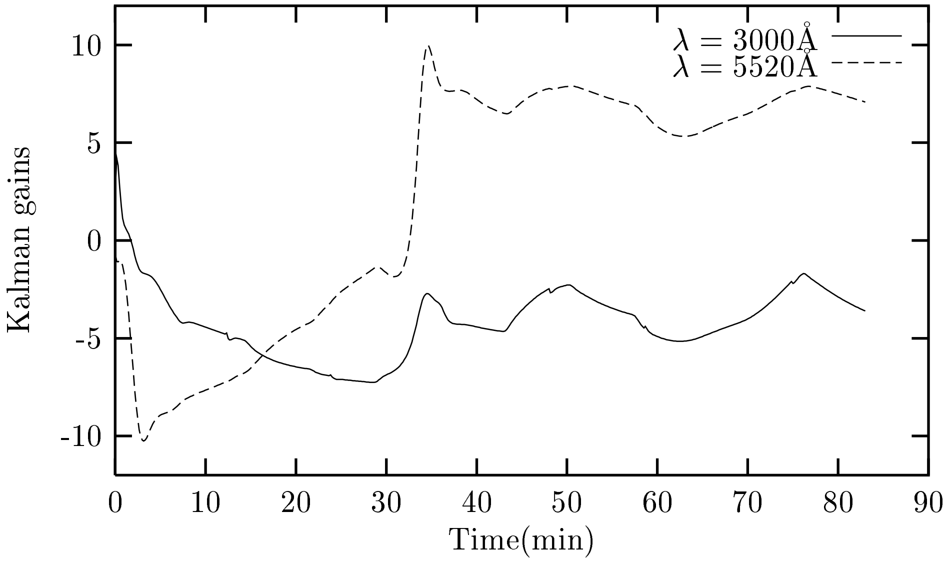

Figure 5.37: Case 3: Kalman filter gains for the wafer temperature disturbance state

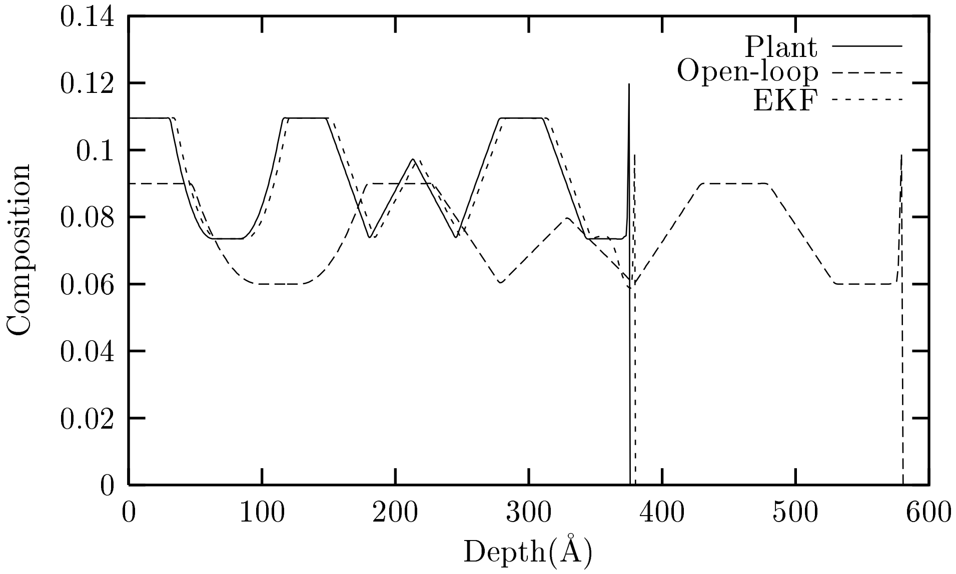

Figure 5.38: Case 3: Resulting film profile

Chapter 6

Regulation and Tracking

At this point it is all numerical hooey

— Rahul Bindlish

As stated in the previous chapter, feedback controllers may perform two separate functions, one of which is to estimate the current value of system states. The other function is regulation. It is the task of the regulator to drive system states to desired targets. A schematic of the estimation and regulation functions of the model–predictive controller used in this work is shown in Figure 6. At each sample time the regulator takes the optimal state estimate $\hat{\mathbf{x}}$ determined by the estimator and attempts to force the inference $\mathbf{z} = \mathbf{h}(\hat{\mathbf{x}})$ to track desired targets $\mathbf{z}^{ref}$ by varying the system's manipulated variables $\mathbf{u}$. Utilizing the optimal estimate delivered from the state estimator at each sample time as the initial starting point for the regulator incorporates feedback into the controller. Section 6.1 presents the model predictive control(MPC) algorithm used in this work. In Section 6.2 simulations are presented that demonstrate the effectiveness of the model predictive controller, which consists of the state estimator and the regulator, for various scenarios.

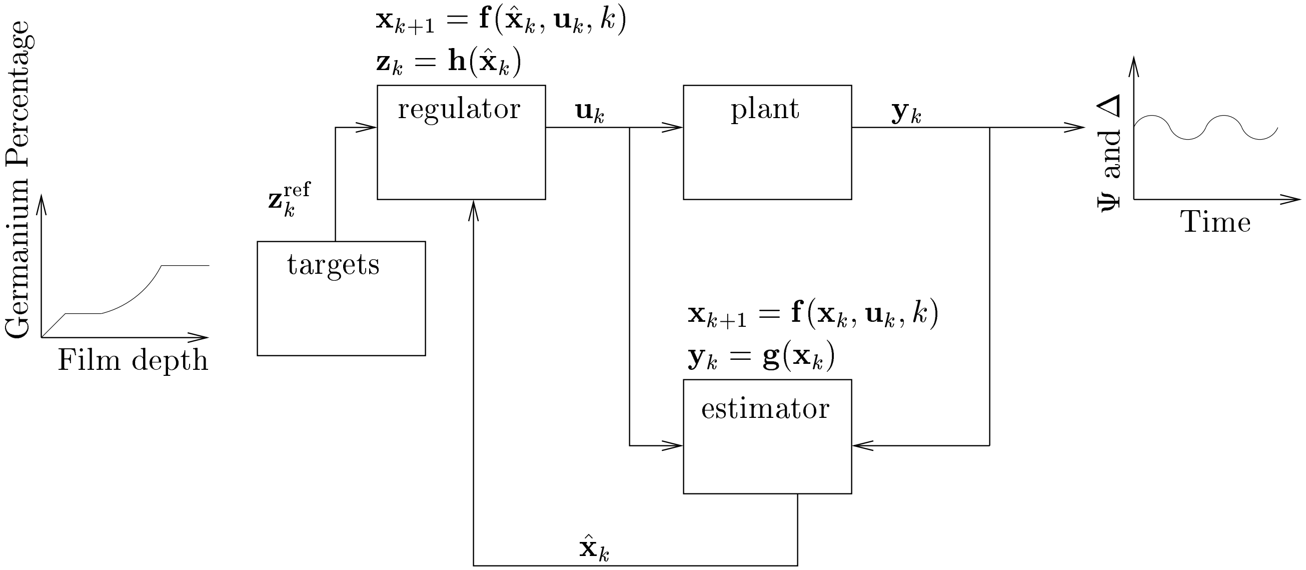

Figure 6.1: Estimation and regulation functions of a model–predictive controller

6.1 MPC Formulation

The essence of model-predictive control(MPC) is to optimize, over the manipulated inputs, forecasts of process behavior. This forecasting is accomplished with a process model. An accurate process model is the cornerstone of an effective MPC controller. Chapter 4 was devoted to developing such a predictive model. The process model is summarized in discrete time as

$$\begin{aligned} \mathbf{x}_{k+1} &= \mathbf{f}(\mathbf{x}_k, \mathbf{u}_k, k) && (6.1) \\ \mathbf{y}_k &= \mathbf{g}(\mathbf{x}_k) && (6.2) \\ \mathbf{z}_k &= \mathbf{h}(\mathbf{x}_k) && (6.3) \end{aligned}$$

where the vector $\mathbf{z}$ is defined as

$$\mathbf{z} = \begin{bmatrix} \mathcal{G} \\ x \end{bmatrix} \tag{6.4}$$

The specific control objective for this work is to grow a $\mathrm{Si}_{1-x}\mathrm{Ge}_x$ alloy with the germanium composition x varying with film thickness in a prescribed manner while maintaining a constant growth rate. The desired targets are dictated by the user before the controller is employed. These controller performance objectives are expressed as the following open–loop quadratic objective function

$$\Phi = \sum_{j=0}^{t_f} ||\mathbf{z}_j^{ref} - \mathbf{z}_j||^2_{\mathbf{Q}} + ||\mathbf{\Delta u}_j||^2_{\mathbf{S}} \tag{6.5}$$

where t_f is the total run time for film growth. The parameters $\mathbf{Q}$ and $\mathbf{S}$ are the weighting matrices on the outputs and the rate of change of the inputs, respectively. Solving the above optimization problem for the entire batch time t_f is intractable due to the large number of decision variables. Thus, the optimization problem is formulated with a smaller number of decision variables to make the problem tractable. The receding horizon regulator is expressed as the following open-loop quadratic function

$$\min_{\mathbf{u}^N} \Phi_k = \sum_{j=0}^{N} ||\mathbf{z}_{k+j}^{ref} - \mathbf{z}_{k+j}||^2_{\mathbf{Q}} + ||\mathbf{\Delta u}_{k+j}||^2_{\mathbf{S}} \tag{6.6}$$

where N is the prediction horizon. The controller minimizes the above objective function in real time subject to the following linear model prediction, which is an approximation of the full non–linear model.

$$\begin{aligned} \mathbf{x}_{k+1} &= \mathbf{f}(\hat{\mathbf{x}}_{k|k}, \mathbf{u}_k) + \mathbf{A}_k x_k + \mathbf{B}_k \mathbf{u}_k && (6.7) \\ \mathbf{z}_k &= \mathbf{h}(\hat{\mathbf{x}}_{k|k}) + \mathbf{C}_k^c \mathbf{x}_k && (6.8) \end{aligned}$$

The non–linear model is re-linearized around the optimal state estimate $\hat{\mathbf{x}}_{k|k}$, which is given by the estimator, to obtain a new linear model at every sample time. The vector of future open-loop control moves $\mathbf{u}^N$ is computed from Equation 6.6 and the first input value is then injected into the plant. The optimization problem is updated and re-solved at each sample time, after a new state estimate becomes available from the estimator. Updating the problem based on the output measurement and re-solving the optimization introduces feedback into the controller.

6.2 Simulations

In this section simulations are presented that demonstrate the effectiveness of the model predictive controller, which consists of the estimator and the regulator, for the same scenarios that were presented in Section 5.4. For each case the control objective is to grow a $\mathrm{Si}_{1-x}\mathrm{Ge}_x$ alloy with the composition x varying with film thickness as shown in Figure 6.2 while maintaining a constant growth rate of $7\frac{\text{Å}}{\text{min}}$. To grow a film that is 580Å thick at $7\frac{\text{Å}}{\text{min}}$ requires that the total batch time t_f be approximately 83 minutes. The sample time for each simulation is 10 seconds. The plant is represented by numerical solution of the full non-linear model with the inputs provided by the regulator at each sample time.

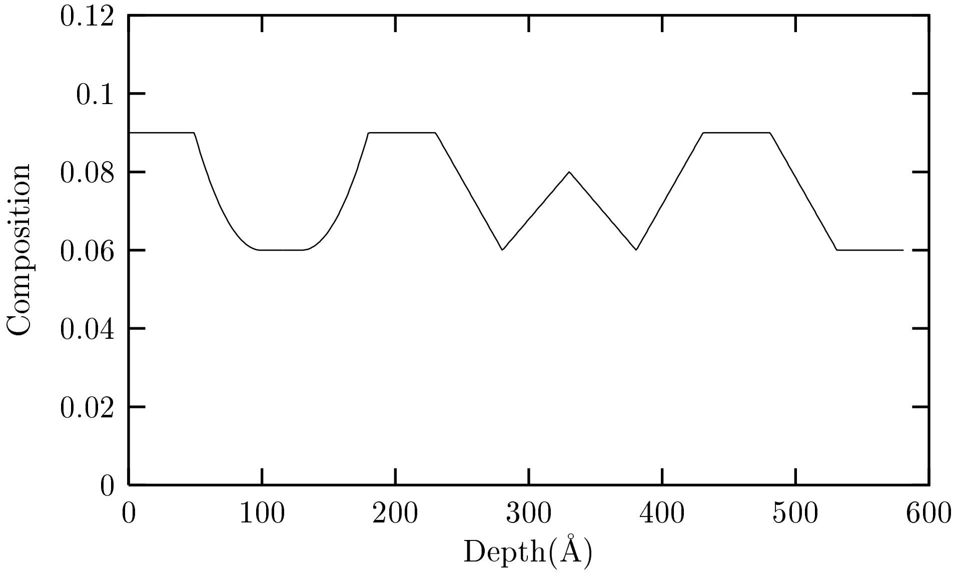

Figure 6.2: Desired profile

6.2.1 Case number 1

The model predictive controller is first tested for the case where there is no mismatch between the plant and the model. The plant response is predicted perfectly with the model. However, the plant data is corrupted with noise. Figures 6.3 and 6.4 show measured and predicted values of Δ for $\lambda = 3000$Å and $\lambda = 5520$Å. The estimator filters out the measurement noise and provides a smooth estimate of Δ.

The EKF also reconstructs the system states and as a result infers the film growth rate and composition, which are shown in Figures 6.7 and 6.9. The regulator then drives the inference of growth rate and composition to the specified targets by manipulating the inputs. The disilane and germane MFC valves are shown in Figure 6.5 and the wafer temperature is displayed in Figure 6.6. The reactor pressure was held constant at 26 mTorr for the entire simulation. Tracking the growth rate and composition set points over the entire batch time produces the desired film, which is shown in Figure 6.10.

The observability values of the two state disturbances are plotted in Figure 6.11. The germane MFC state disturbance is completely observable. The wafer temperature state disturbance is nearly unobservable at the beginning of the simulation. However, as more data is taken from the higher wavelength sensor the observability of the wafer temperature disturbance increases. Figures 6.12 and 6.13 show the estimated state disturbances. The state disturbances do not converge to any specific values as there is no mismatch between the plant and the model. For this case the estimated state disturbances reflect the noise in the output measurements.

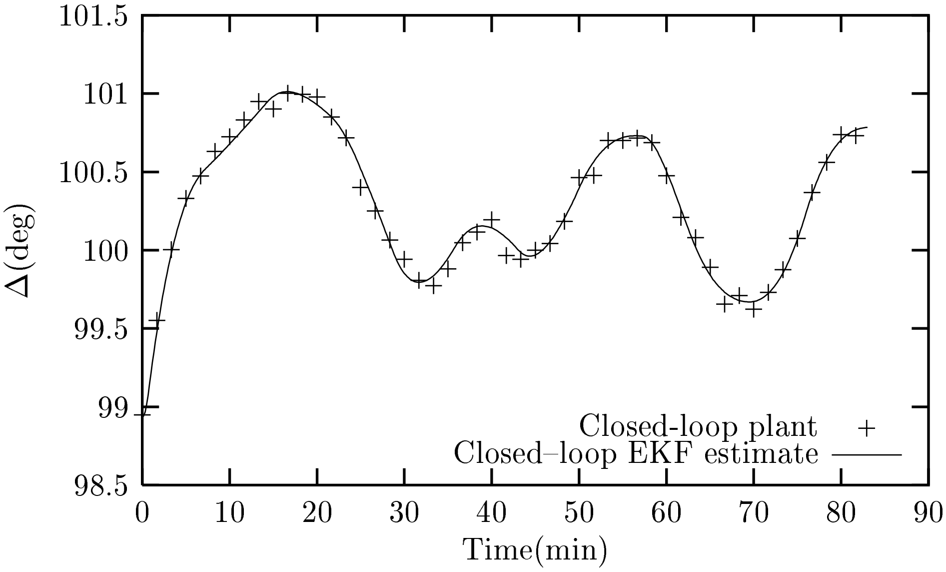

Figure 6.3: Case 1: Δ for $\lambda = 3000$Å

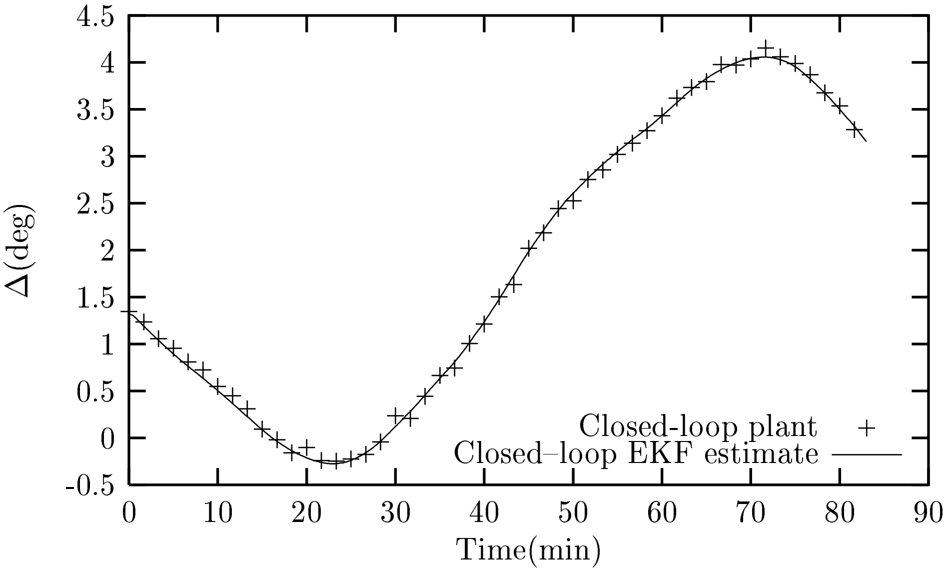

Figure 6.4: Case 1: Δ for $\lambda = 5520$Å

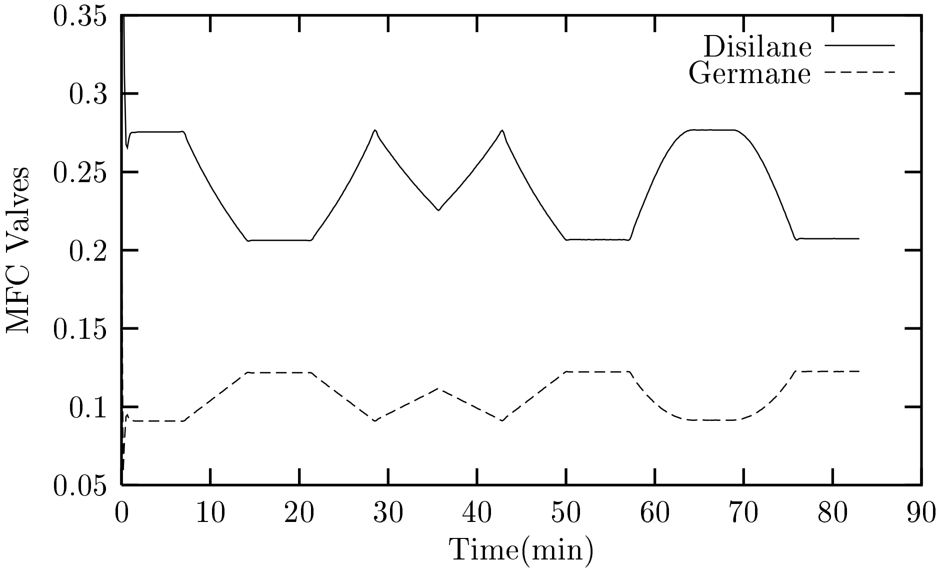

Figure 6.5: Case 1: Disilane and germane MFC valve positions

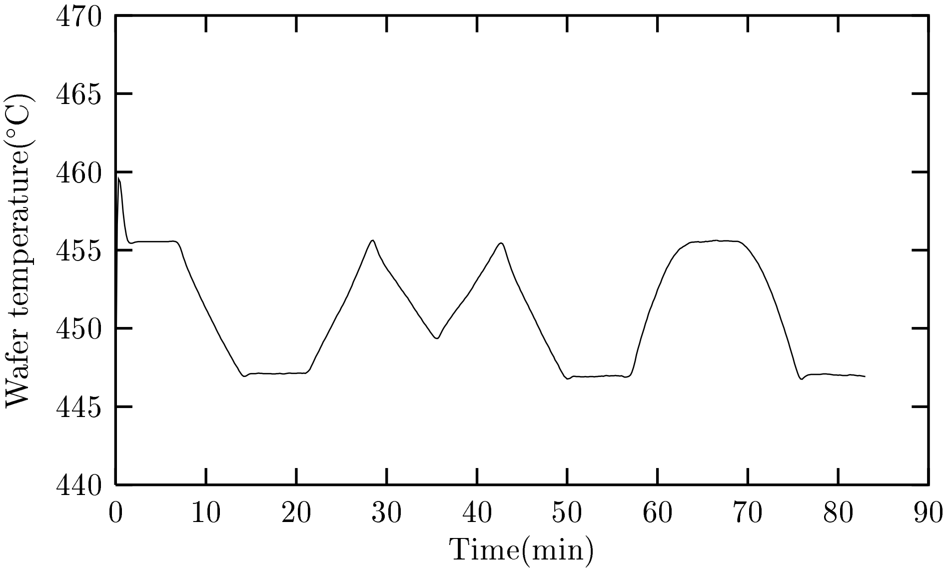

Figure 6.6: Case 1: Wafer temperature

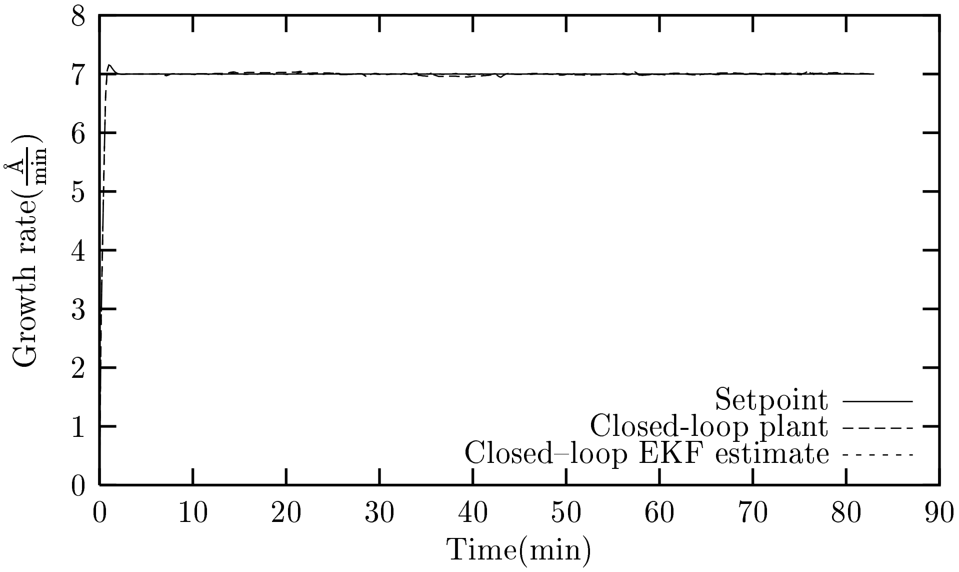

Figure 6.7: Case 1: Film growth rate

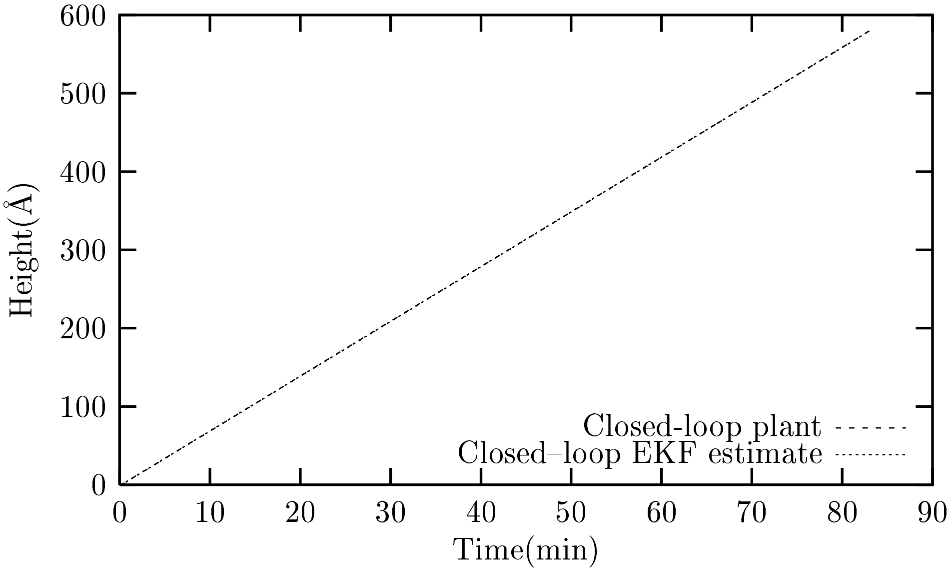

Figure 6.8: Case 1: Film height

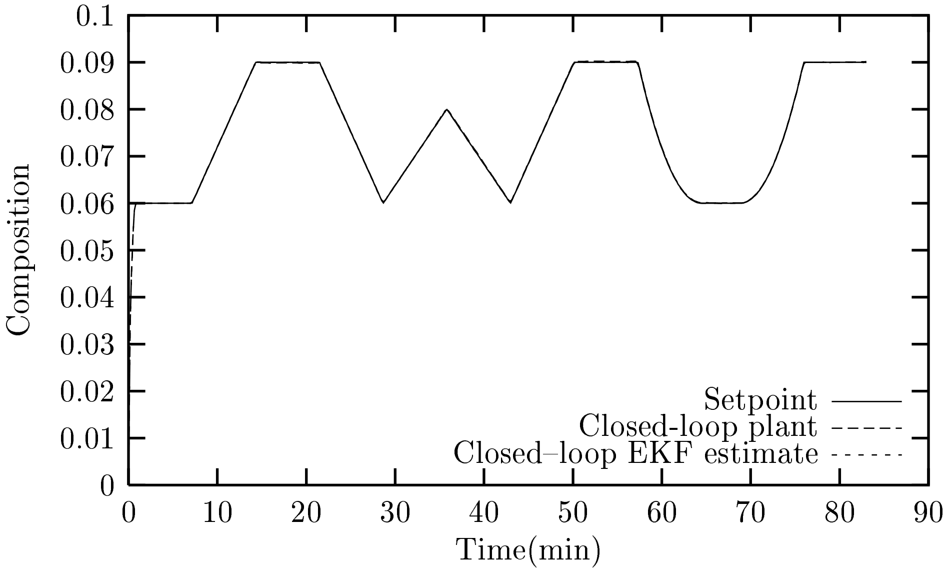

Figure 6.9: Case 1: Film composition

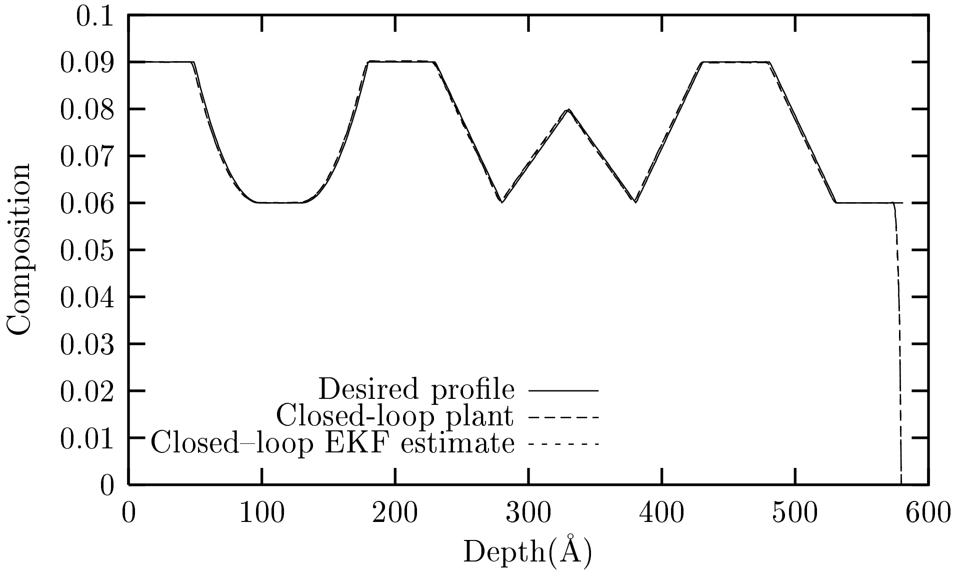

Figure 6.10: Case 1: Resulting film

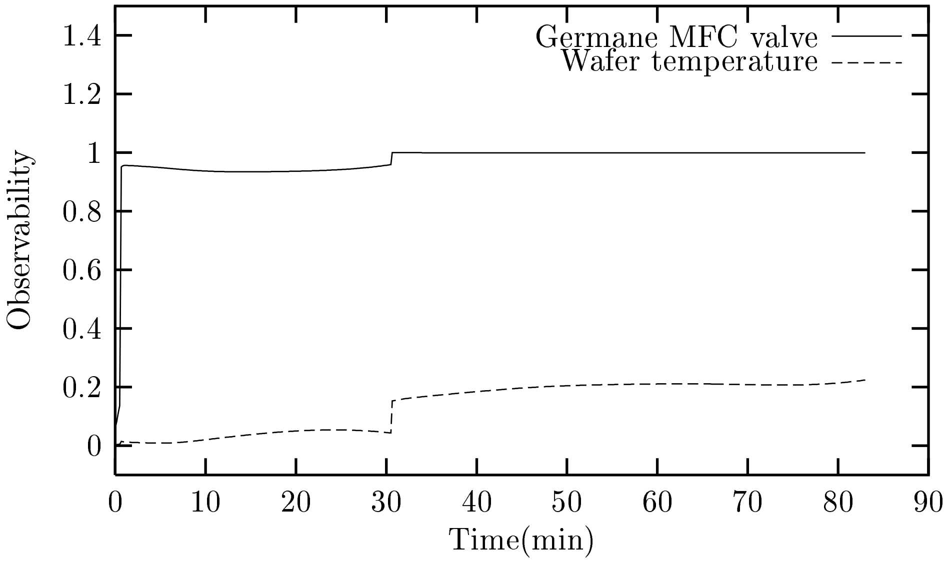

Figure 6.11: Case 1: Closed–loop observability of the state disturbances

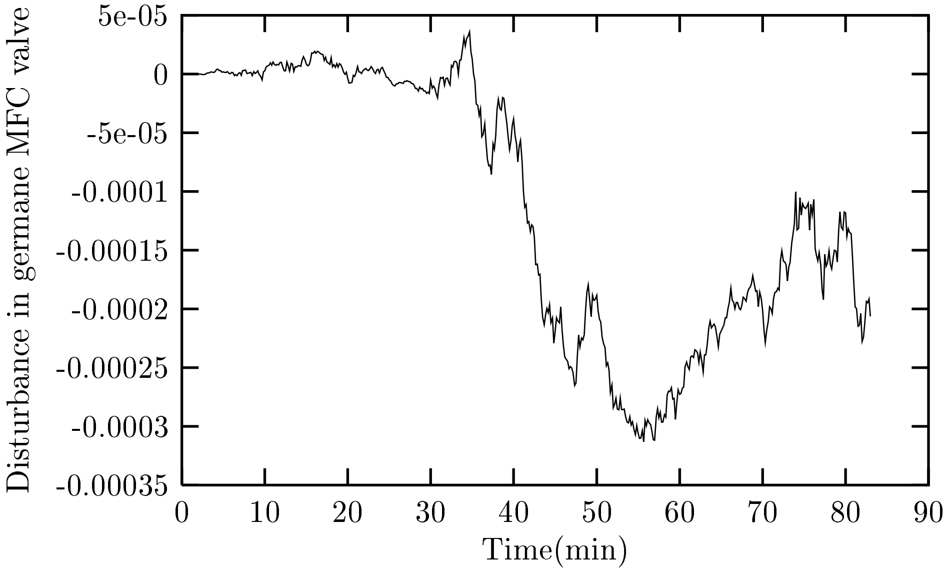

Figure 6.12: Case 1: State disturbance in the germane MFC valve

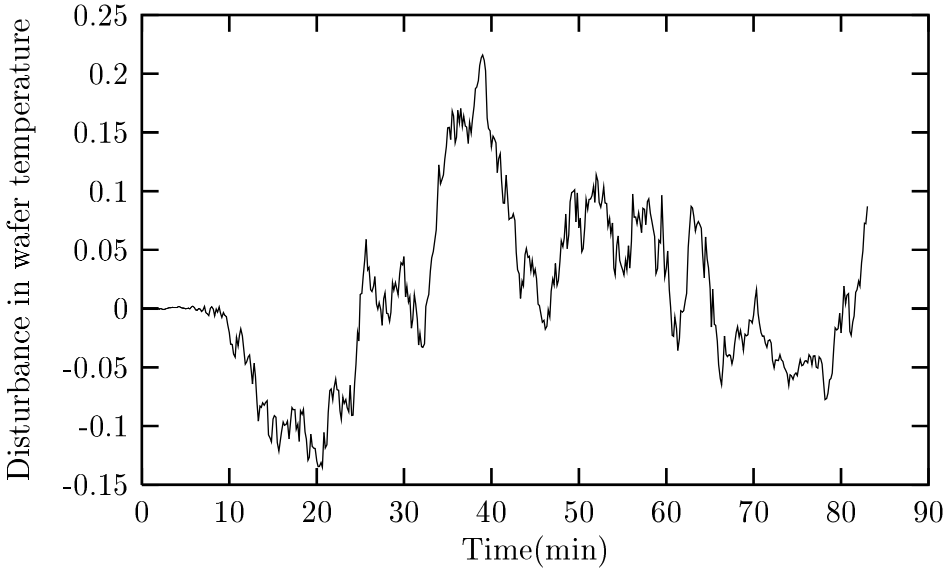

Figure 6.13: Case 1: State disturbance in wafer temperature

6.2.2 Case number 2

This set of simulations demonstrates the effectiveness of the model predictive controller when there is mismatch between the plant and the model prediction of the plant. The mismatch in this case is as follows:

- The germane MFC valve position is open 0.1 more than expected
- The temperature of the wafer is 10 degrees hotter than expected

Figures 6.14 and 6.15 show the measured and estimated values of Δ for $\lambda = 3000\text{Å}$ and $\lambda = 5520\text{Å}$ for the entire simulation. The EKF estimates of Δ converge to and track the plant values for the entire simulation. The figures also show the open–loop model prediction of Δ for both wavelengths. The mismatch between the open–loop model prediction and the plant response shows up prominently in Δ. The estimates of the disturbance states are shown in Figures 6.20 and 6.21. The Kalman filter succeeds in pinpointing the unmeasured disturbances and correcting them.

The state estimator also reconstructs the system states and as a result infers the film growth rate and composition, which are shown in Figures 6.22 and 6.24. The regulator then drives the inference of growth rate and composition to the specified targets by manipulating the inputs. The disilane and germane MFC valve positions determined by the regulator are shown in Figures 6.16 and 6.17. The wafer temperature is displayed in Figure 6.18. The regulator held the reactor pressure constant at 26 mTorr for the entire simulation. Tracking the growth rate and composition set points for the entire batch time produces the desired film, which is shown in Figure 6.25.

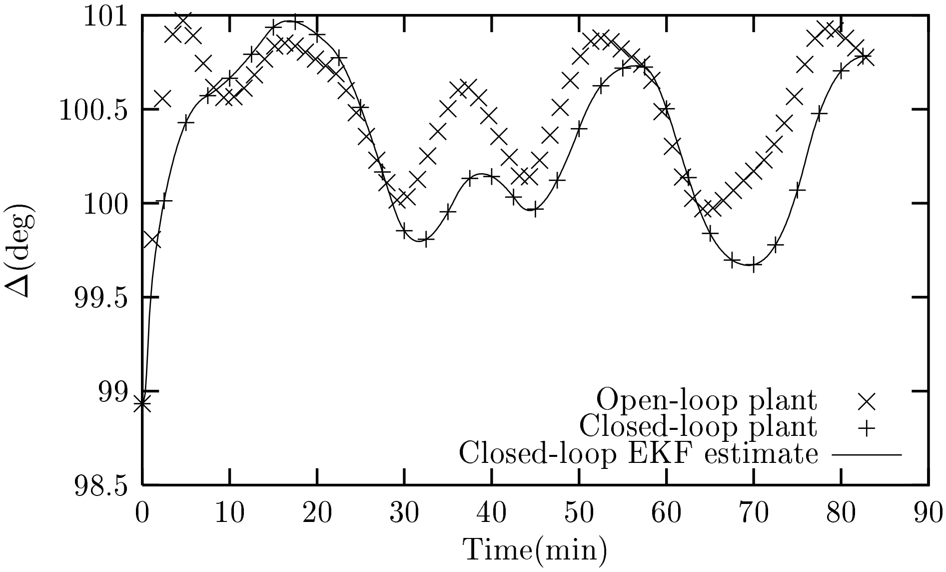

Figure 6.14: Case 2: Δ for $\lambda = 3000$Å

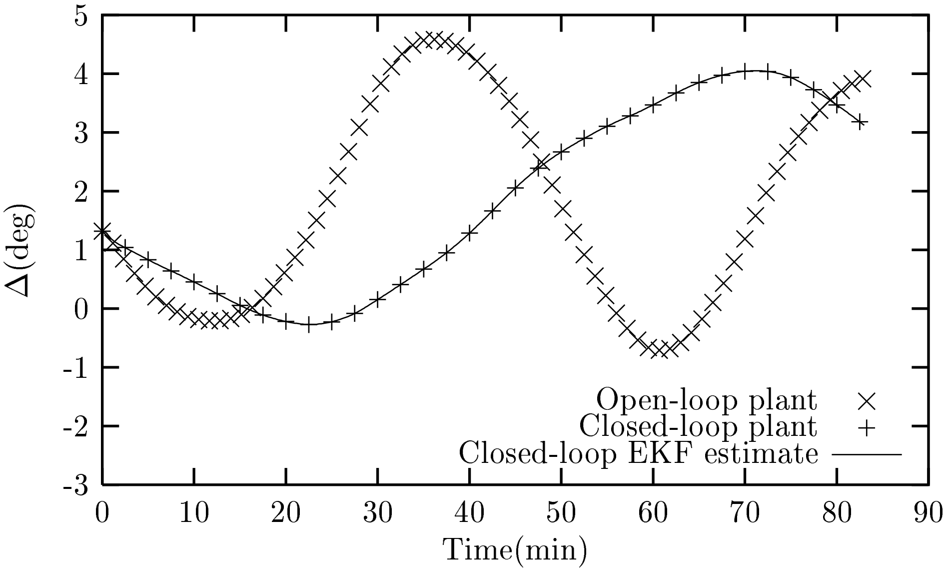

Figure 6.15: Case 2: Δ for $\lambda = 5520$Å

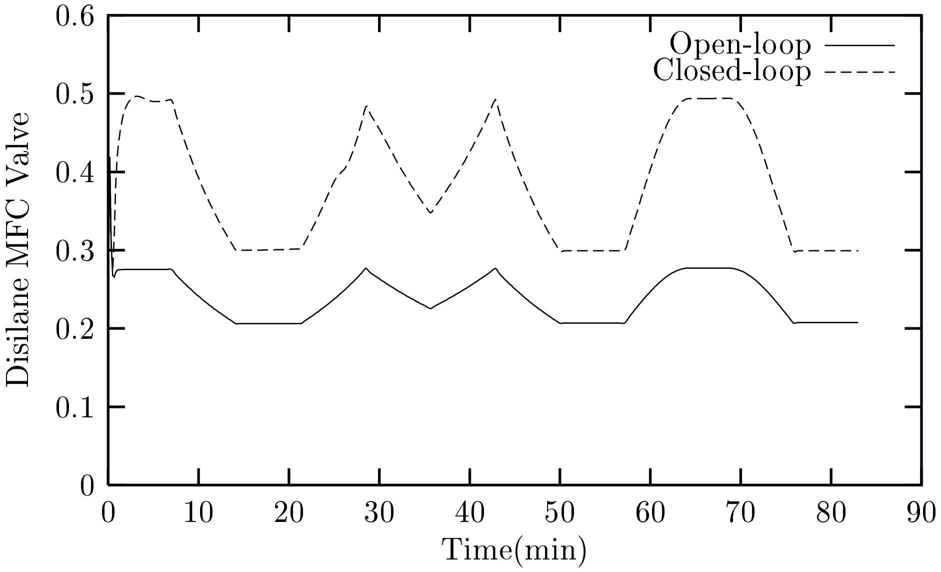

Figure 6.16: Case 2: Disilane MFC valve position

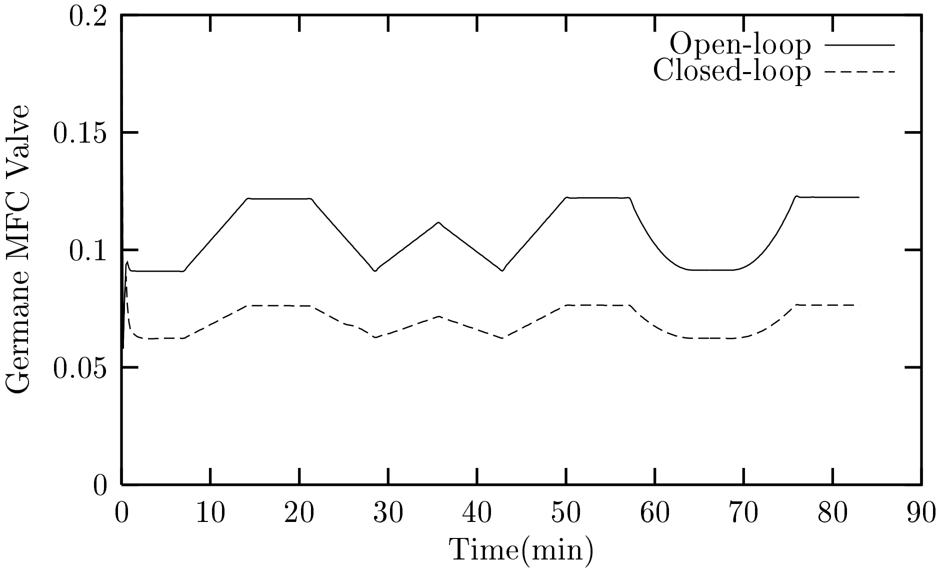

Figure 6.17: Case 2: Germane MFC valve position

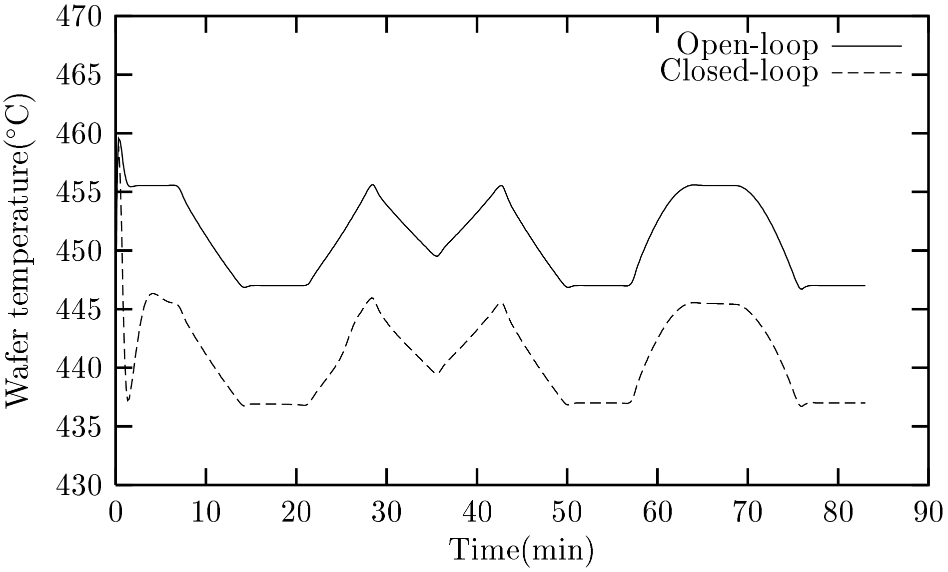

Figure 6.18: Case 2: Wafer temperature

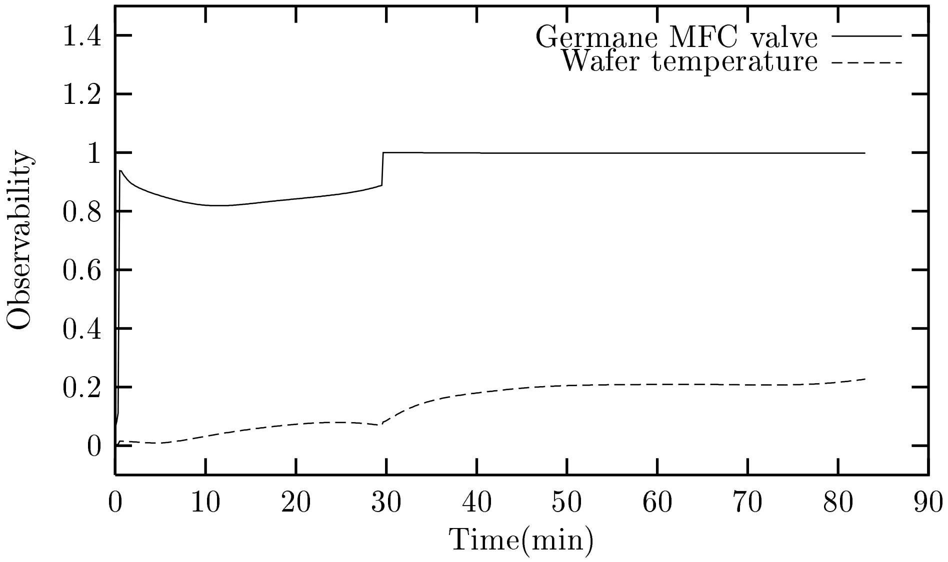

Figure 6.19: Case 2: Closed–loop observability of the state disturbances

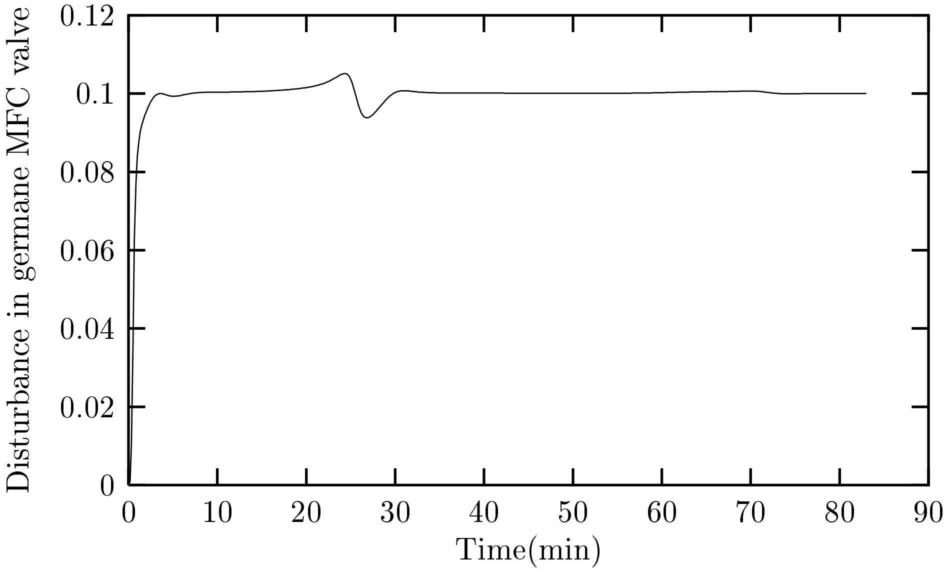

Figure 6.20: Case 2: State disturbance in the germane MFC valve

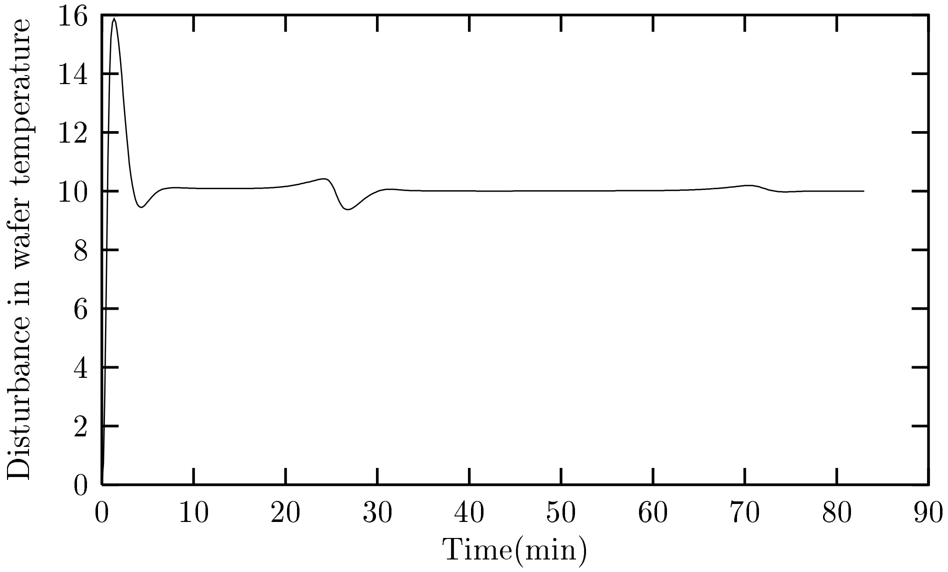

Figure 6.21: Case 2: State disturbance in wafer temperature

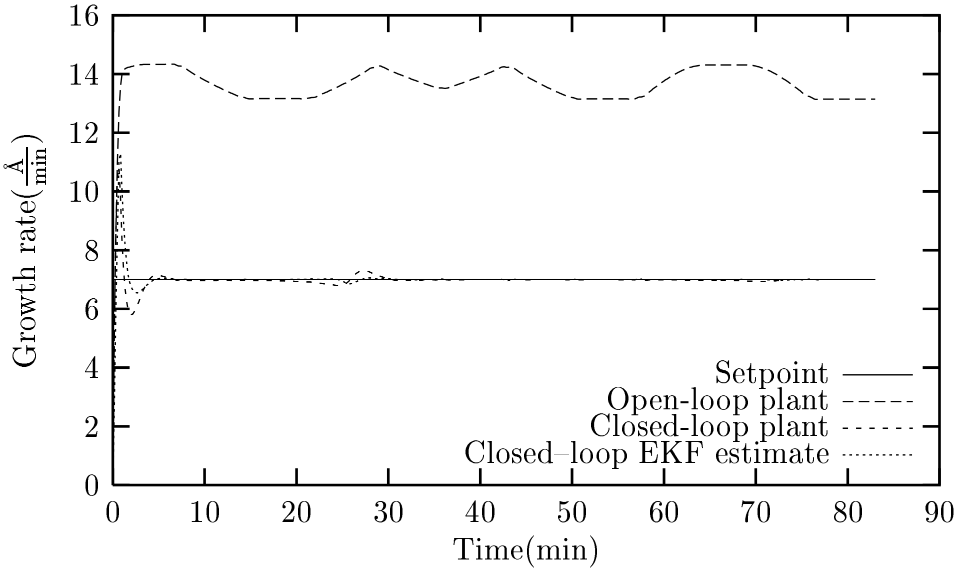

Figure 6.22: Case 2: Film growth rate

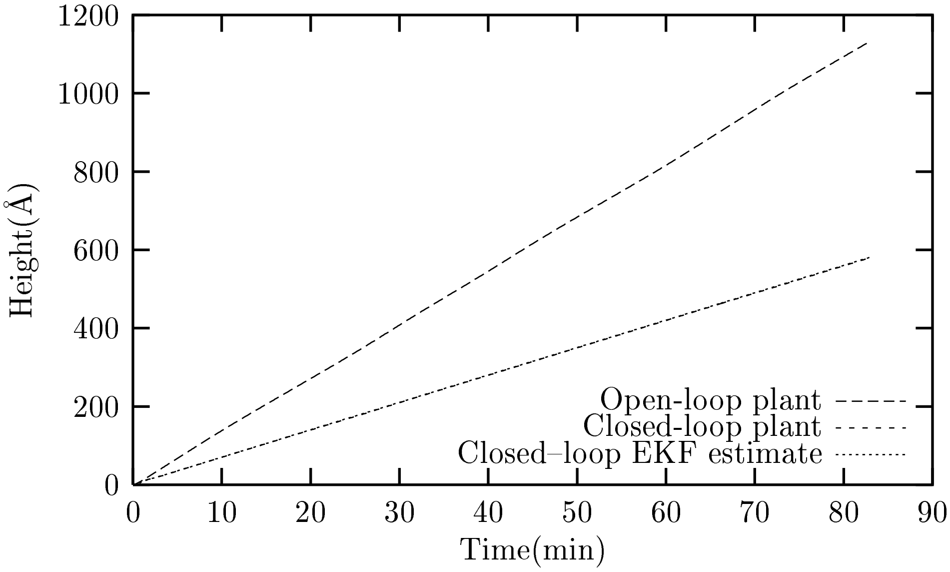

Figure 6.23: Case 2: Film height

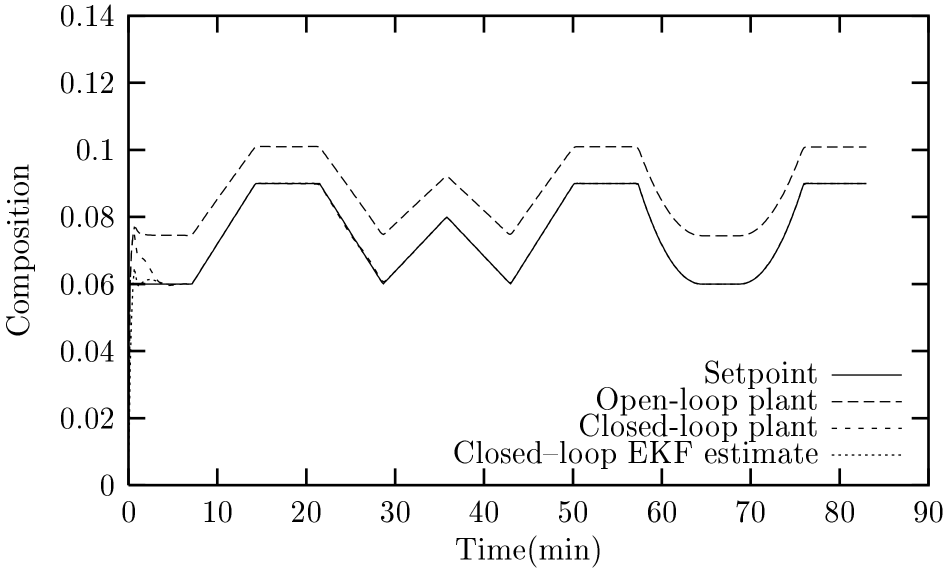

Figure 6.24: Case 2: Film composition

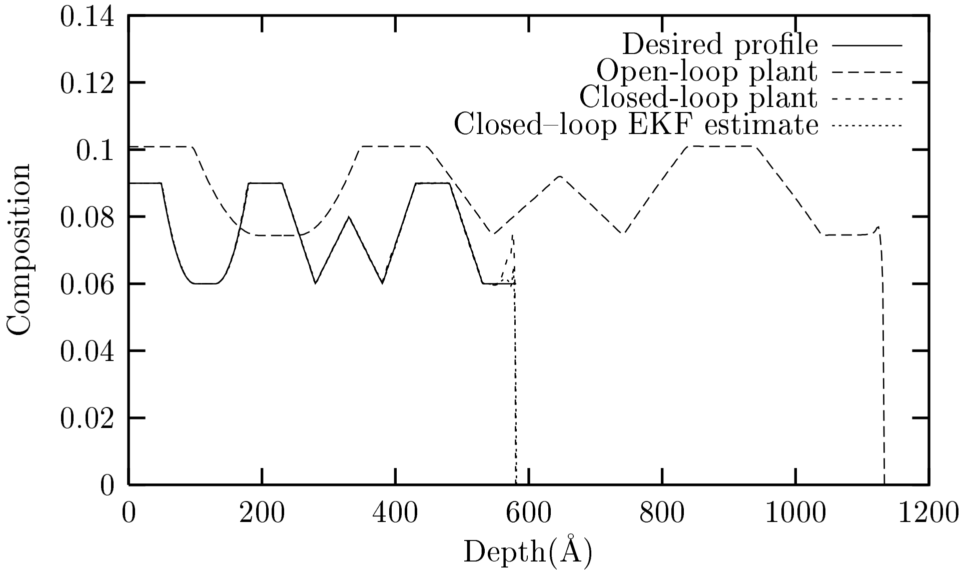

Figure 6.25: Case 2: Resulting film

6.2.3 Case number 3

This simulation demonstrates the effectiveness of the model predictive controller for a more general case of plant–model mismatch, which is simulated by placing a mismatch in the kinetic parameter k_7. The model value for the parameter k_7 is set 50% larger than the plant value.

Figures 6.29 and 6.30 show the first six minutes of the measured and estimated values of Δ for $\lambda = 3000\text{Å}$ and $\lambda = 5520\text{Å}$. The open–loop model prediction of Δ is plotted as well.

Figures 6.29 and 6.30 show the measured and estimated values of Δ for $\lambda = 3000\text{Å}$ and $\lambda = 5520\text{Å}$ for the entire simulation. The EKF estimates of Δ converge to and track the plant values for the entire simulation. The figures also show the open–loop model prediction of Δ for both wavelengths. The mismatch between the open–loop model prediction and the plant response shows up prominently in Δ. The Kalman filter detects a deviation between the predicted value of Δ and the measured plant value. The filter rationalizes that this error between the measured and predicted output is caused by unmeasured disturbances in the MFC germane valve and wafer temperature and updates those states. The estimates of the disturbance states are shown in Figures 6.32 and 6.33. The kinetic mismatch is essentially modeled as unmeasured disturbances in the MFC germane valve and the wafer temperature.

The filter also reconstructs the system states and as a result infers the film growth rate and composition, which are shown in Figures 6.34 and 6.36. The regulator then drives the inference of growth rate and composition to the specified targets by manipulating the inputs. The disilane and germane MFC valve positions determined by the regulator are shown in Figures 6.26 and 6.27. The wafer temperature is displayed in Figure 6.28. The regulator held the reactor pressure constant at 26 mTorr for the entire simulation. Tracking the growth rate and composition set points for the entire batch time produces the desired film, which is shown in Figure 6.37.

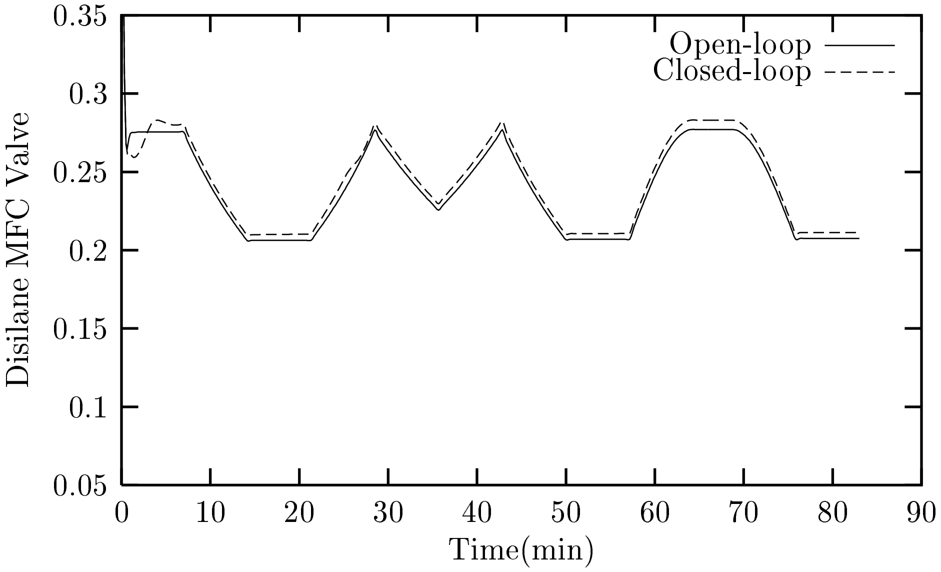

Figure 6.26: Case 3: Disilane MFC valve position

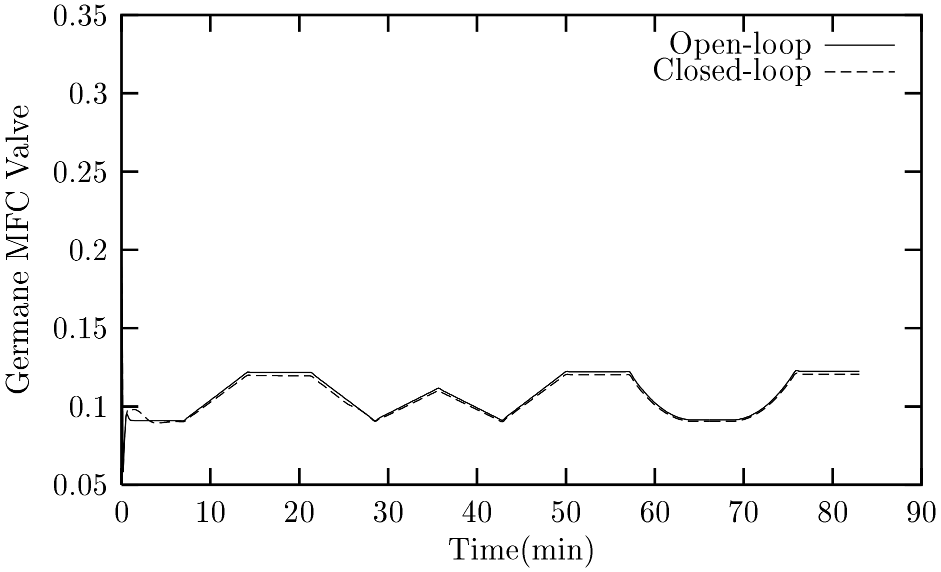

Figure 6.27: Case 3: Germane MFC valve position

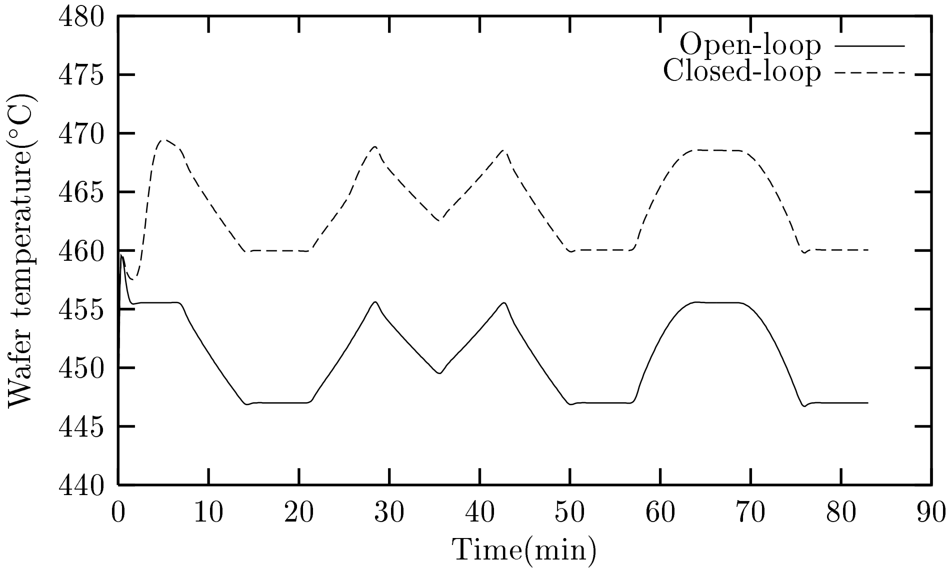

Figure 6.28: Case 3: Wafer temperature

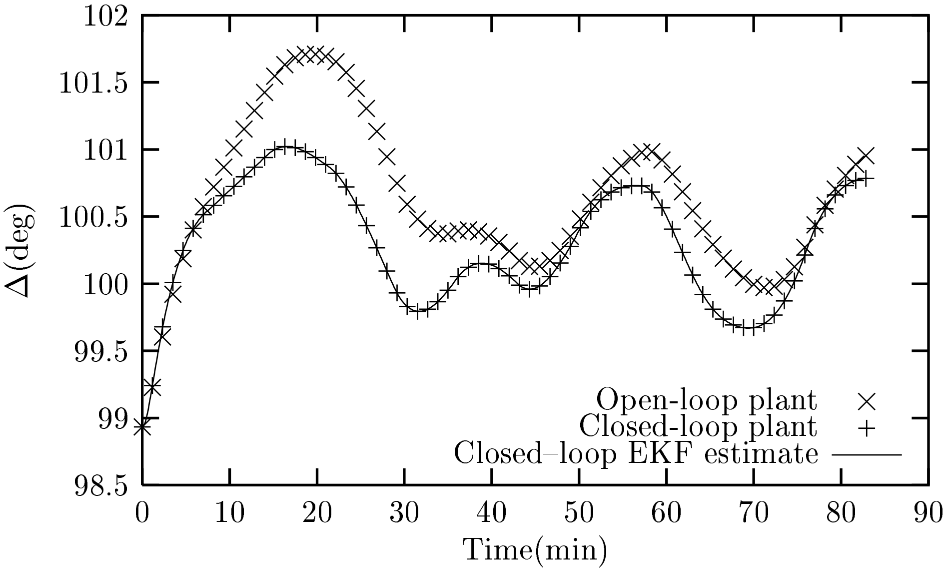

Figure 6.29: Case 3: Δ for $\lambda = 3000\text{Å}$

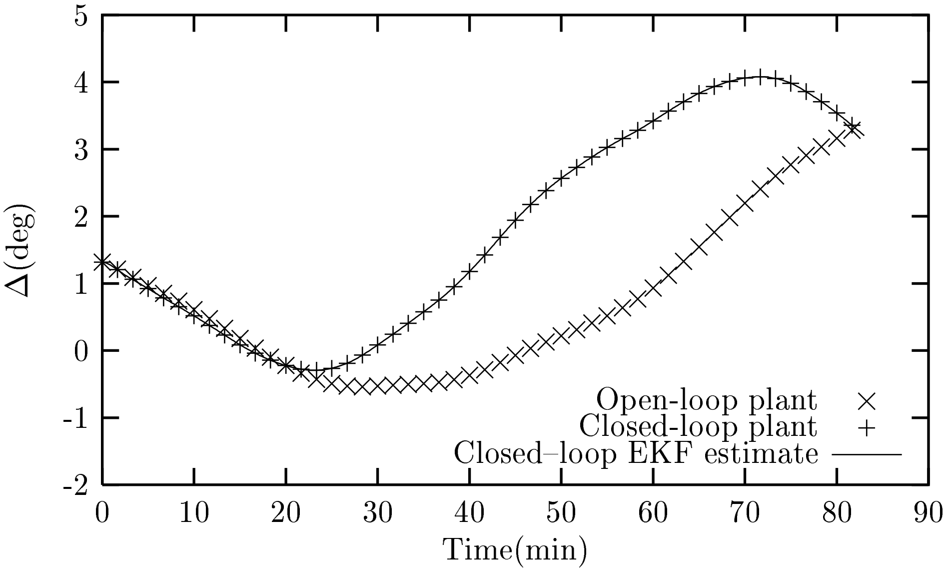

Figure 6.30: Case 3: Δ for $\lambda = 5520\text{Å}$

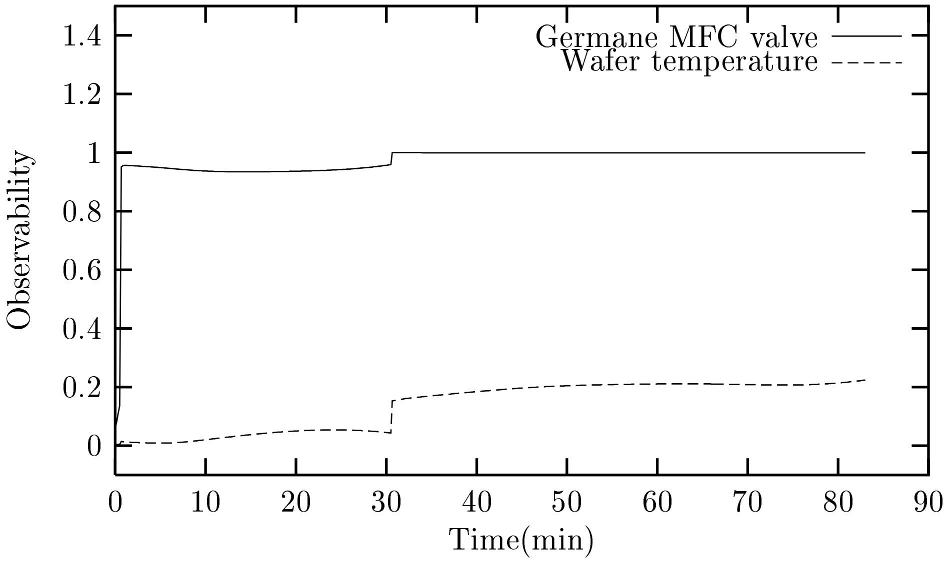

Figure 6.31: Case 3: Closed–loop observability of the state disturbances

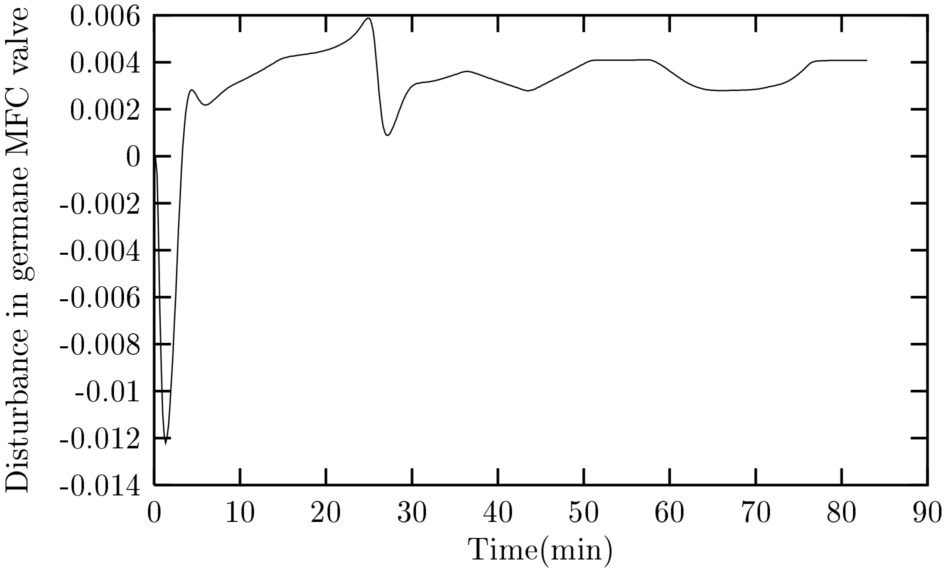

Figure 6.32: Case 3: State disturbance in the germane MFC valve

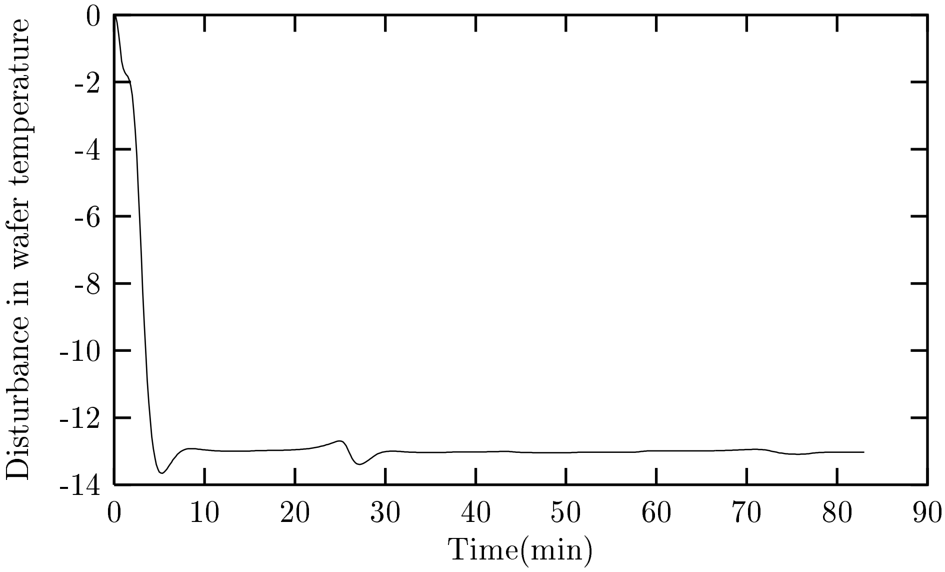

Figure 6.33: Case 3: State disturbance in wafer temperature

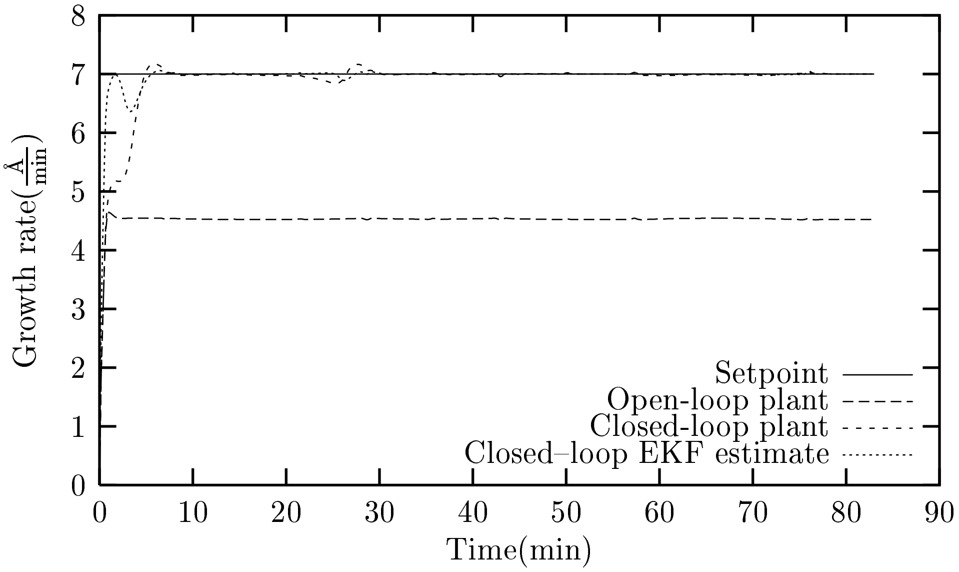

Figure 6.34: Case 3: Film growth rate

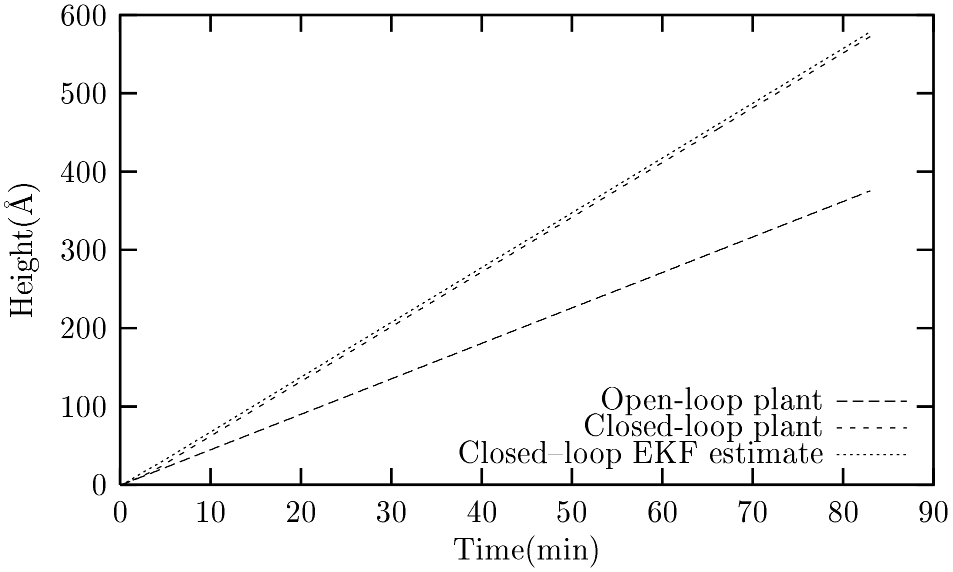

Figure 6.35: Case 3: Film height

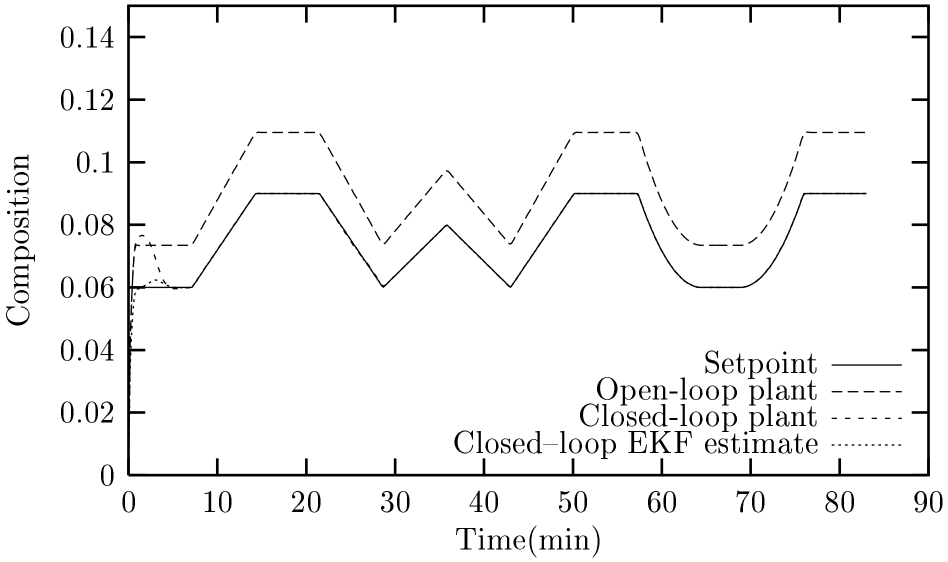

Figure 6.36: Case 3: Film composition

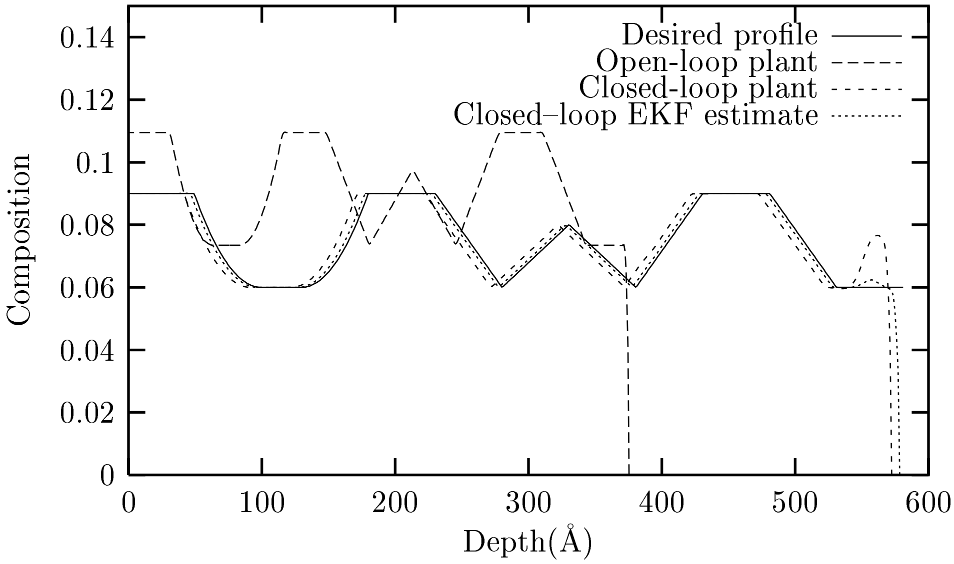

Figure 6.37: Case 3: Resulting film

Chapter 7

Experimental Results

> *The rare occurence of the expected*
>
> — William Carlos Williams, *At Kenneth Burke's Place*

The model predictive controller is tested by growing aggressive $\mathrm{Si}_{1-x}\mathrm{Ge}_x$ alloy composition profiles and the results are presented in this chapter. The experimental results presented in this work provide the first demonstration of feedback control using online optical film measurements to grow aggressive alloy composition profiles in which flow rates of several component gases and reactor temperature must be varied simultaneously in order to achieve the profile of interest. The films grown utilizing feedback from the optical sensor are compared to the films grown using open–loop recipes. These films are compared quantitatively utilizing off-line characterization techniques, such as auger spectrometry or secondary–ion–mass–spectrometry (SIMS) analysis. Section 7.1 presents an experiment that shows the effectiveness of closed–loop control for propitious conditions. Section 7.2 shows an experiment that further demonstrates the effectiveness of the closed–loop controller by rejecting a temperature disturbance. In Section 7.3 an experiment is presented that shows the limitations of the controller. During each experiment, Δ for only one wavelength($\lambda = 5520$Å) is used for feedback. The Verity ellipsometer used in this work is not able to resolve Δ for wavelengths less than 4500Å. Below 4500Å the signal to noise ratio for the instrument is very low and the values of Ψ and Δ cannot be discerned.

7.1 Experiment number 1

The model predictive controller is first tested for the case where experimental conditions are favorable. There are no known disturbances entering the plant and the model predicts accurately. Figure 7.1 shows the measured and estimated values of Δ for $\lambda = 5520\text{Å}$ for an open–loop and closed–loop run. There is some disagreement between the measurements of the open–loop and the closed–loop run. This discrepancy might be caused by unmeasured disturbances, such as temperature or valve fluctuations, or it might simply indicate that there is some model mismatch. The closed–loop EKF estimate of Δ tracks the closed–loop measurement by attributing any variation between the output measurement and the output prediction as a disturbance in the substrate temperature. This temperature disturbance is shown in Figure 7.2. The state disturbance necessary to converge the EKF estimate of Δ to the measured value is small, suggesting that the model does a reasonable job of predicting. The observability of the temperature state disturbance during the closed–loop run is shown in Figure 7.3. The observability is quite low at the beginning of the run. However, as more data is collected the observability increases and ultimately the wafer temperature state disturbance is inferred.

Figure 7.4 shows the open–loop and closed–loop substrate temperature set points determined by the regulator. The figure also shows the temperature response as measured by the pyrometer. Notice that there is a slight difference between the open–loop and closed–loop set points. This difference is caused by the regulator correcting the small temperature disturbance that was determined by the state estimator.

Figures 7.5 and 7.6 show the disilane and germane valve set points determined by the regulator during both the open–loop and the closed–loop experiment. Notice that there is no difference between the open–loop and closed–loop valve positions. Since only Δ corresponding to a large wavelength was available for feedback, the germane MFC state disturbance was not estimated. Any difference between the measured and predicted value of Δ was corrected by adjusting only the wafer temperature.

Figures 7.7 and 7.9 show the closed–loop EKF estimates of film growth rate and composition as well as the desired targets for each. The regulator drives the estimates of growth rate and composition to their specified set points while the EKF estimate of Δ converges to and tracks the plant response measured by the ellipsometer.

The resulting film profiles grown with open–loop and closed–loop control are shown in Figure 7.10. The figure shows that the closed–loop EKF estimate of the film profile converges to profile that was specified. The figure also shows the profiles of the physical films as measured by SIMS analysis. The film grown utilizing feedback from the optical sensor is truer to the desired profile than the film grown with an open–loop recipe.

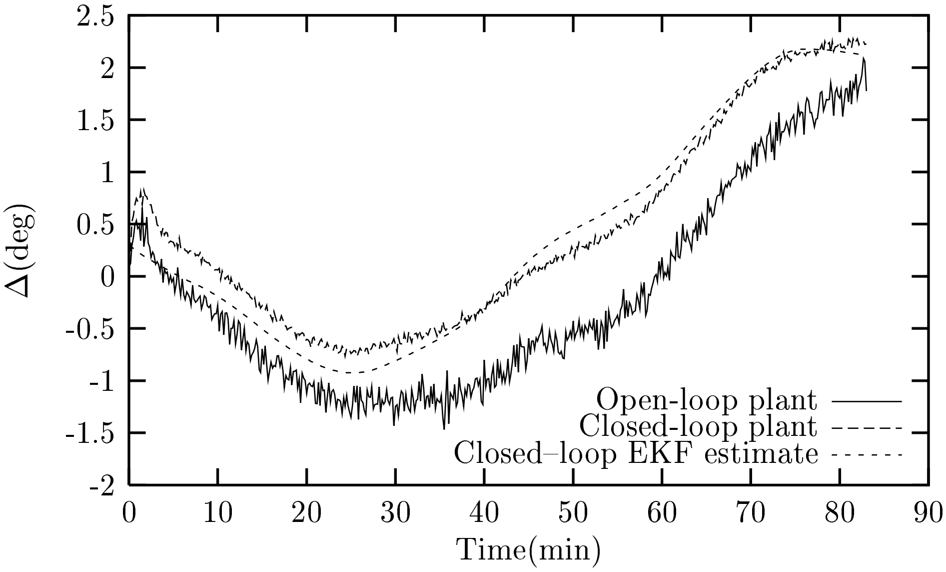

Figure 7.1: Experiment 1: Δ for $\lambda = 5520$Å

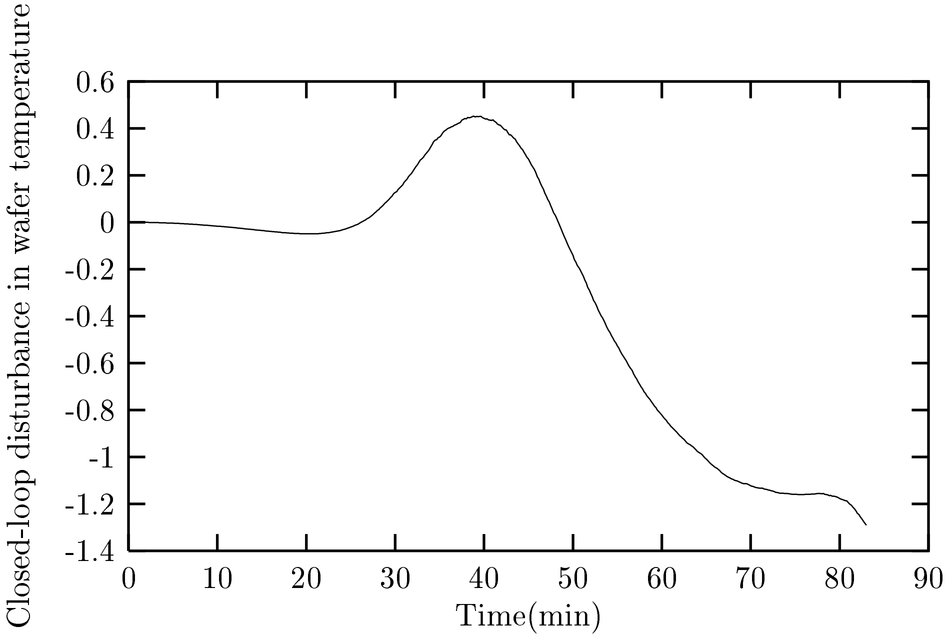

Figure 7.2: Experiment 1: State disturbance in wafer temperature

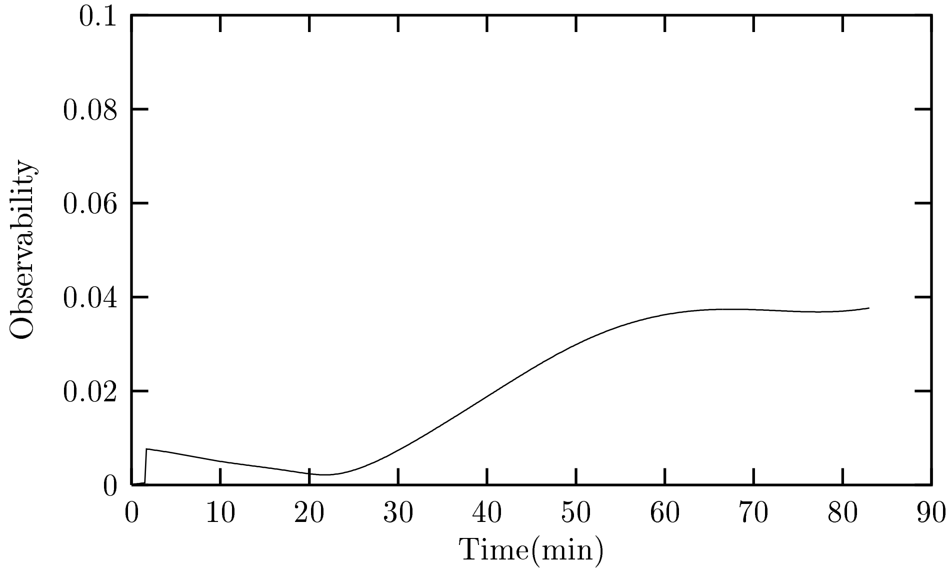

Figure 7.3: Experiment 1: Closed–loop observability of state disturbance in wafer temperature

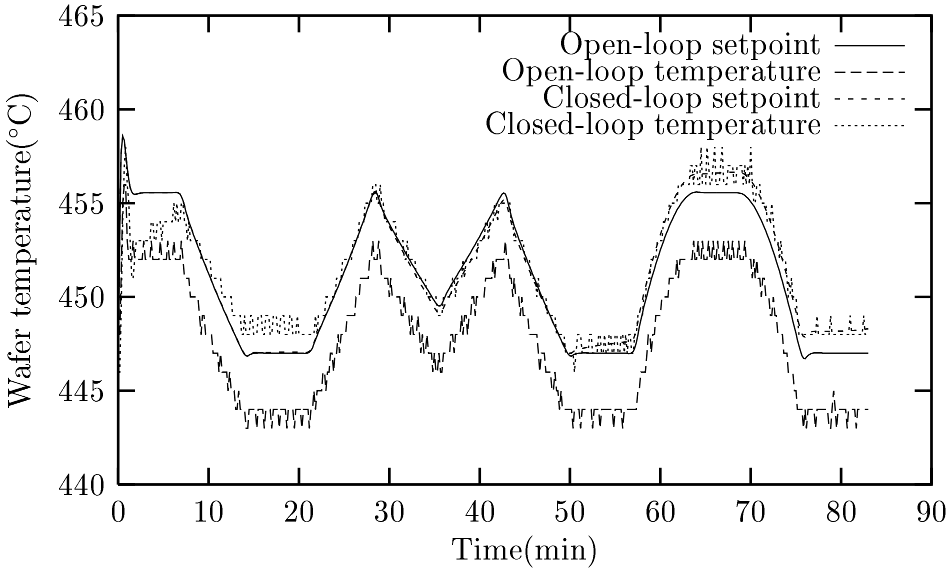

Figure 7.4: Experiment 1: Wafer temperature

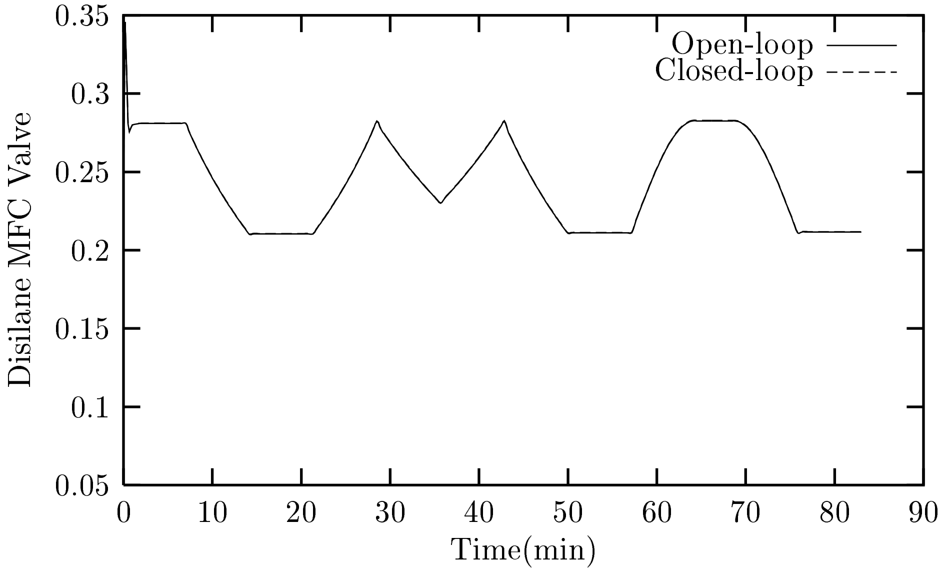

Figure 7.5: Experiment 1: Disilane MFC valve position

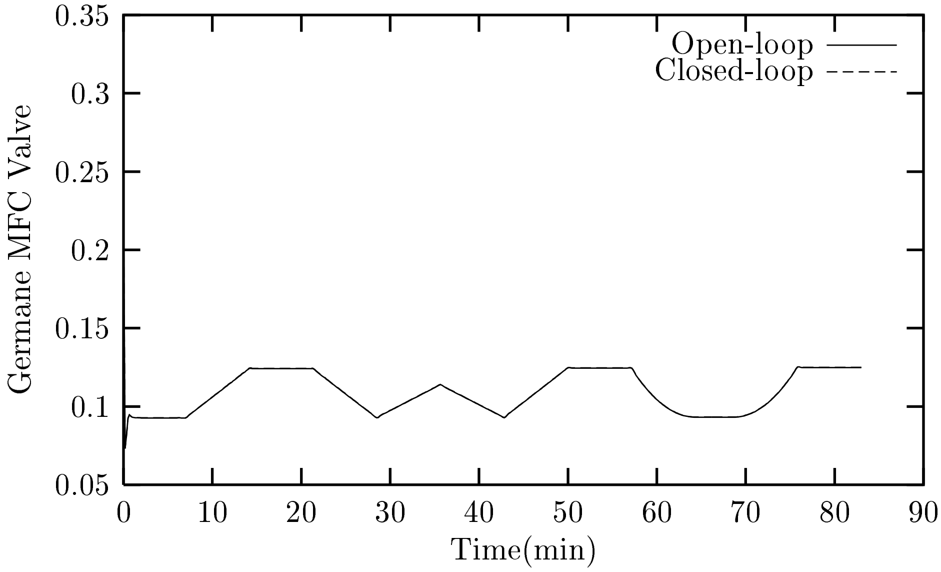

Figure 7.6: Experiment 1: Germane MFC valve position

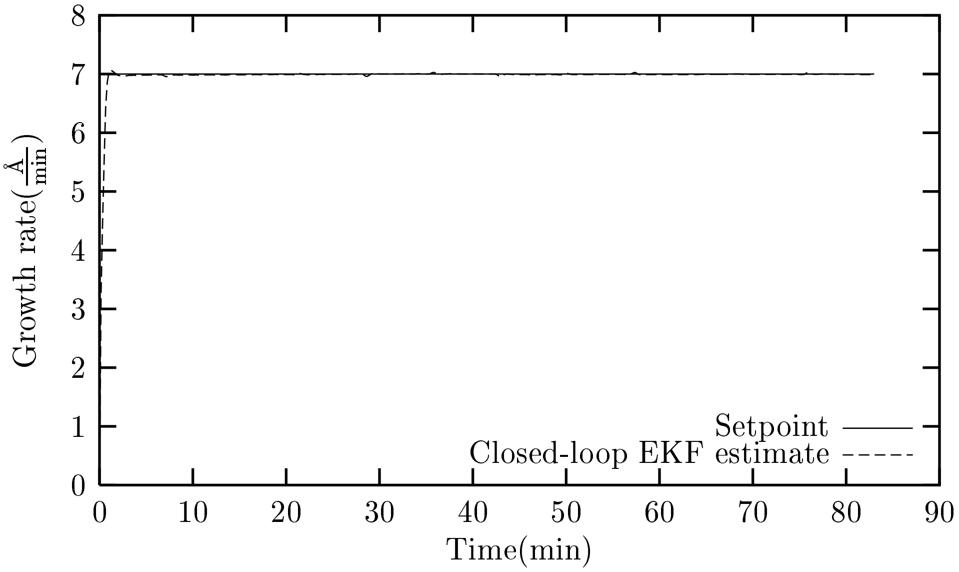

Figure 7.7: Experiment 1: Film growth rate

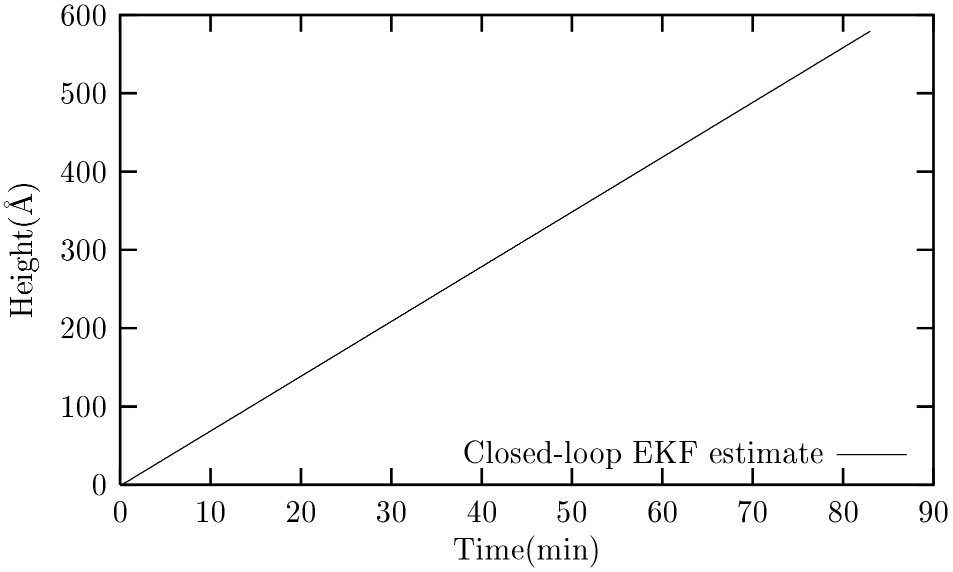

Figure 7.8: Experiment 1: Film height

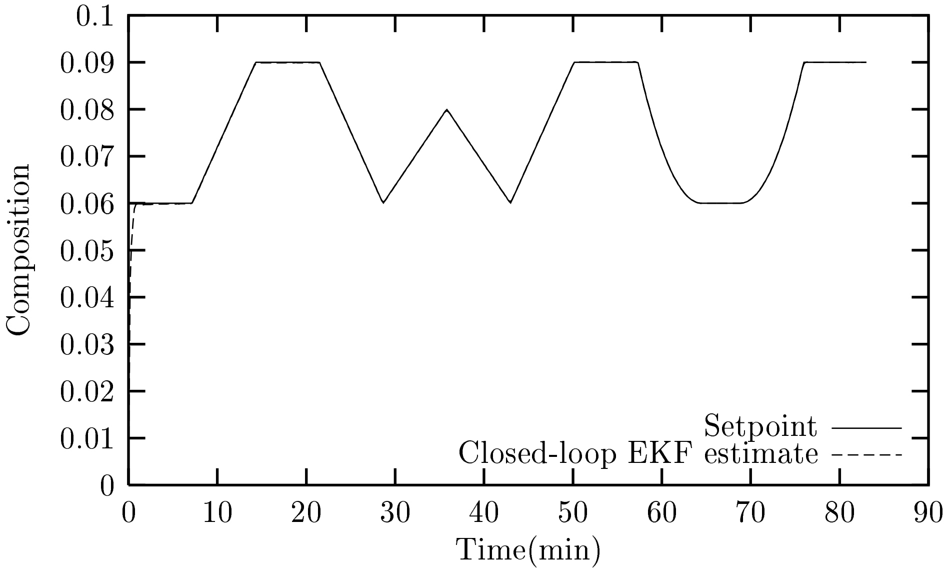

Figure 7.9: Experiment 1: Film composition

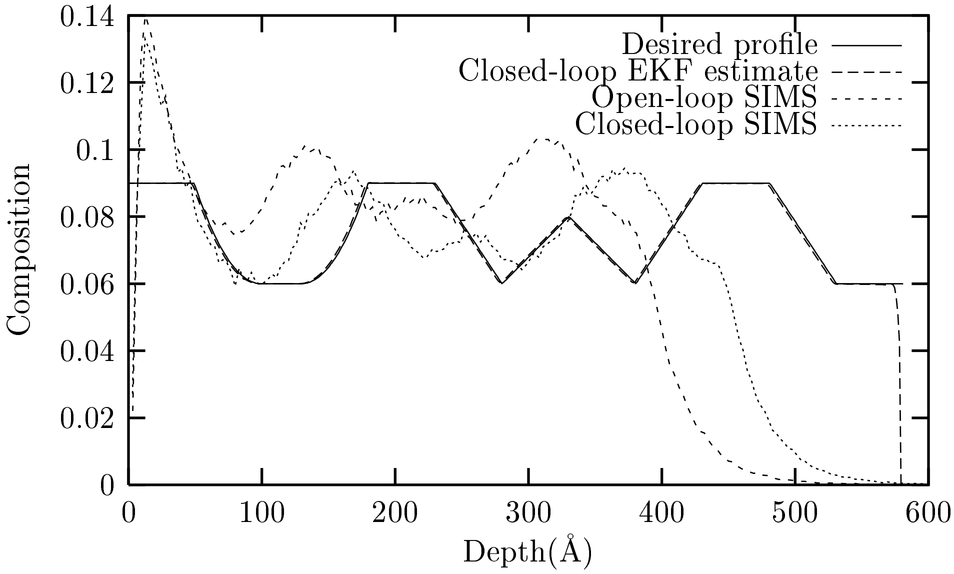

Figure 7.10: Experiment 1: Resulting films

7.2 Experiment number 2

In this experiment the model predictive controller is tested for the case where there is an unmeasured temperature disturbance. In this case the temperature disturbance is caused by a measurement error in the pyrometer. The pyrometer, which is used to regulate the substrate temperature, reports that the wafer temperature is 10 degrees less than it it really is. Thus, the wafer temperature is 10 degrees hotter than the model expects.

Figure 7.11 shows the measured and estimated values of Δ for $\lambda = 5520\text{Å}$ for the open–loop and closed–loop runs. The closed–loop EKF estimate of Δ tracks the closed–loop measurement by attributing any variation between the output measurement and the output prediction as a disturbance in the substrate temperature. The estimated temperature state disturbance is shown in Figure 7.12. The observability of the temperature state disturbance during the closed–loop run is shown in Figure 7.13. The observability is quite low at the beginning of the run. However, as more data is collected the observability increases and ultimately the wafer temperature state disturbance is inferred.

Figures 7.17 and 7.19 show the closed–loop EKF estimates of film growth rate and composition as well as the desired targets for each. Notice that at around 20 minutes into the run the EKF estimate of the growth rate moves off its set point. As stated in the above paragraph, the state estimator is not able to infer the temperature state disturbance until about 20 minutes into the run, at which time enough data has been collected. After about 20 minutes, the EKF infers the growth rate and the regulator drives it back to its target by adjusting the wafer temperature. The regulator drives the estimates of growth rate and composition to their specified set points while the EKF estimate of Δ converges to and tracks the plant response measured by the ellipsometer.

Figure 7.14 shows the open–loop and closed–loop substrate temperature set points determined by the regulator. The figure also shows the temperature response as measured by the pyrometer, which reports a temperature that is 10 degrees lower than actual. Notice that there is about a 10 degree difference between the open–loop and closed–loop set points. This difference is caused by the regulator correcting the temperature disturbance that was determined by the state estimator in order to keep the estimates of growth rate and composition on target.

Figures 7.15 and 7.16 show the disilane and germane valve set points determined by the regulator during both the open–loop and the closed–loop experiment. Notice that there is no difference between the open–loop and closed–loop valve positions. Since only Δ corresponding to a large wavelength was available for feedback, the germane MFC state disturbance was not estimated. Any difference between the measured and predicted value of Δ was corrected by adjusting only the wafer temperature.

The resulting film profiles grown with open–loop and closed–loop control are shown in Figure 7.20. The figure shows the physical film profiles as measured by SIMS analysis. The film grown utilizing an open–loop recipe is almost twice as thick as desired. In contrast, the film grown utilizing feedback from the optical sensor is truer to the desired profile.

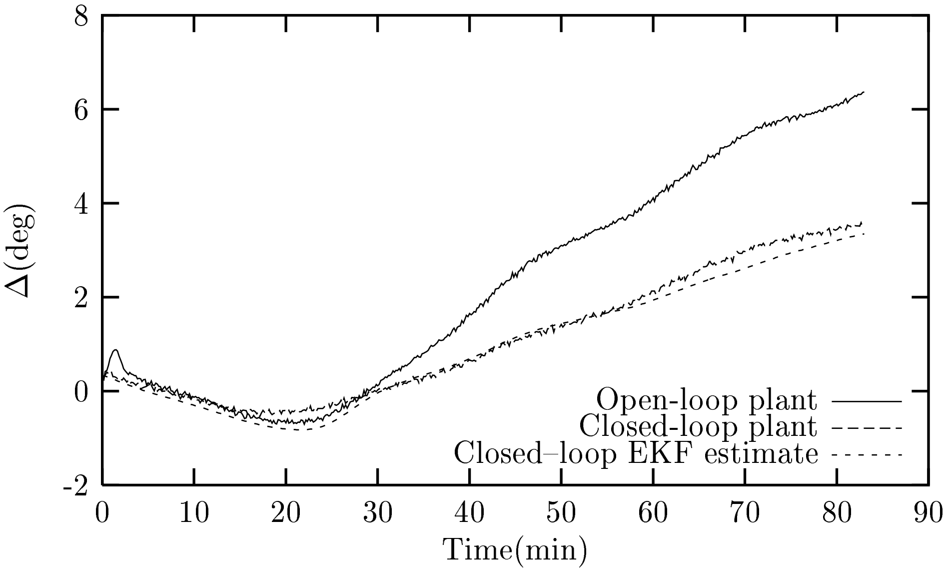

Figure 7.11: Experiment 2: Δ for $\lambda = 5520$Å

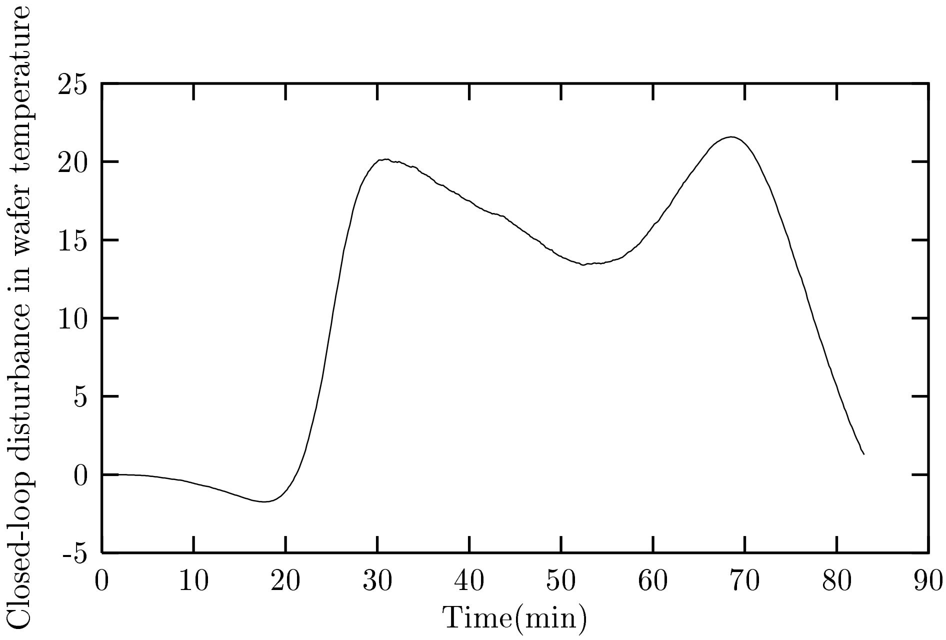

Figure 7.12: Experiment 2: State disturbance in wafer temperature

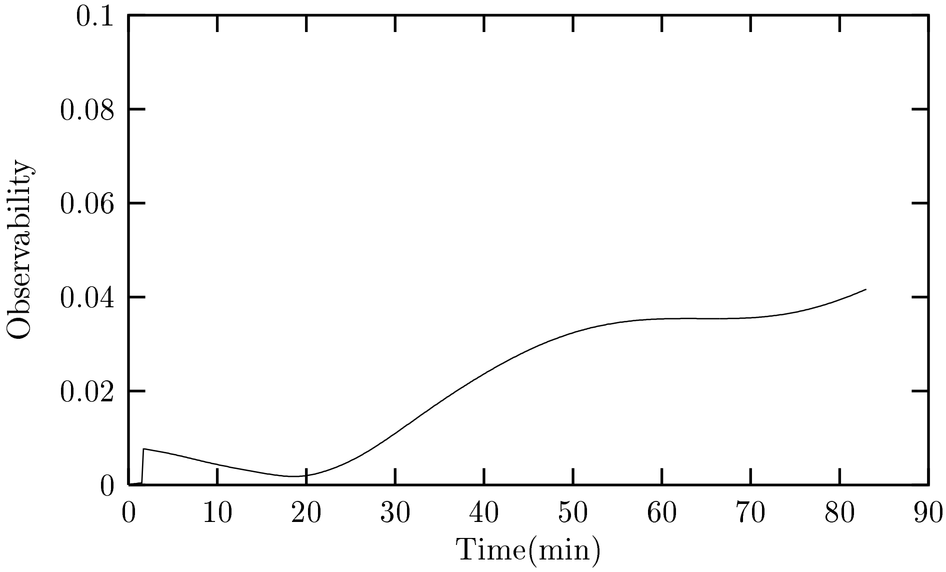

Figure 7.13: Experiment 2: Closed–loop observability of state disturbance in wafer temperature

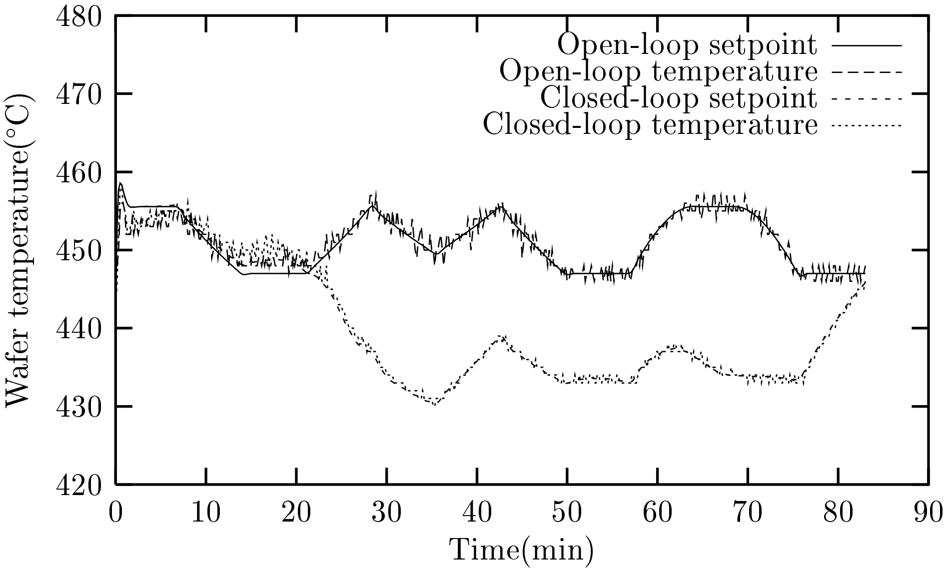

Figure 7.14: Experiment 2: Wafer temperature

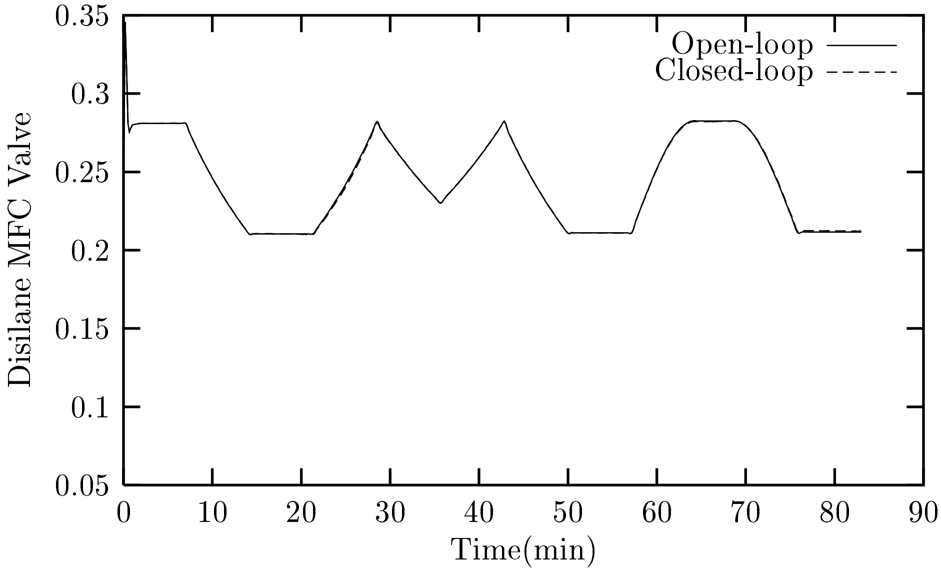

Figure 7.15: Experiment 2: Disilane MFC valve position

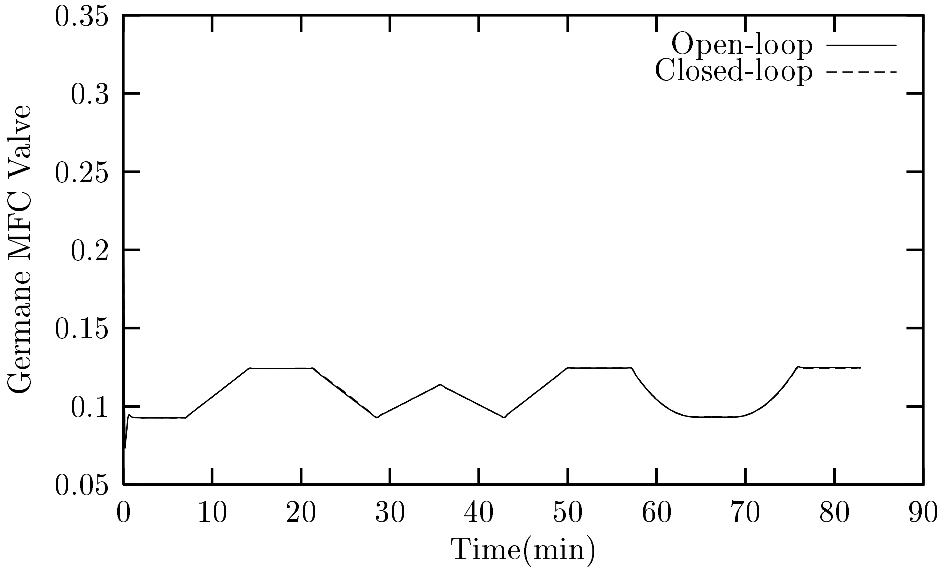

Figure 7.16: Experiment 2: Germane MFC valve position

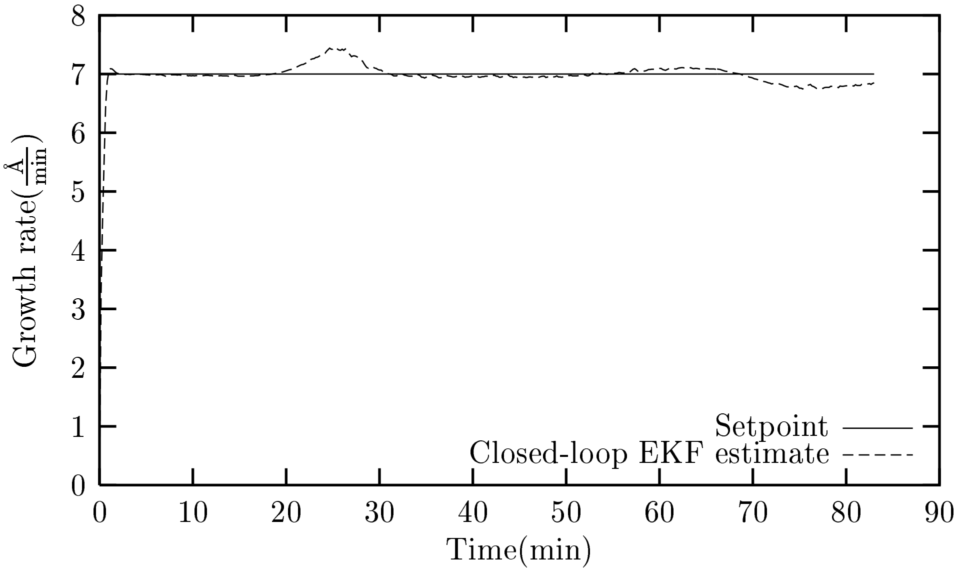

Figure 7.17: Experiment 2: Film growth rate

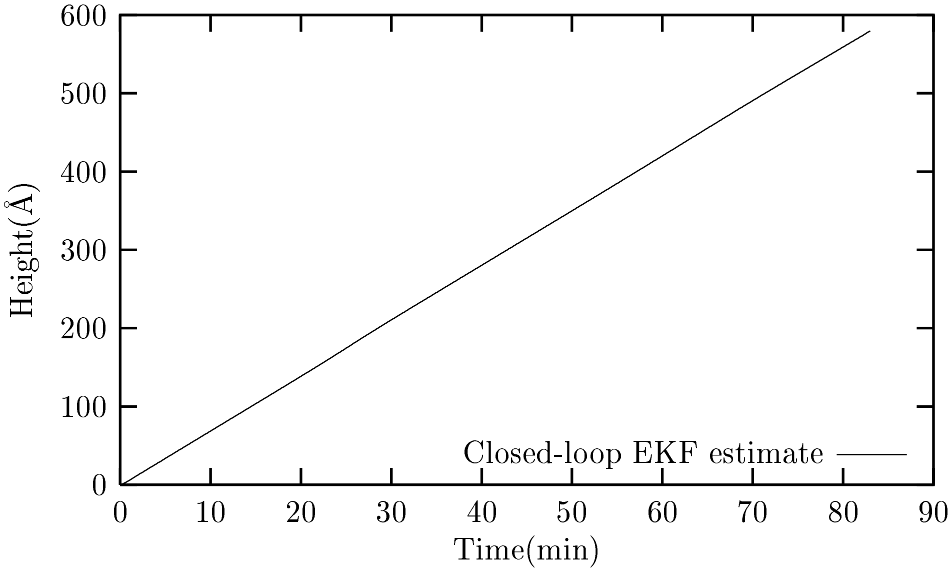

Figure 7.18: Experiment 2: Film height

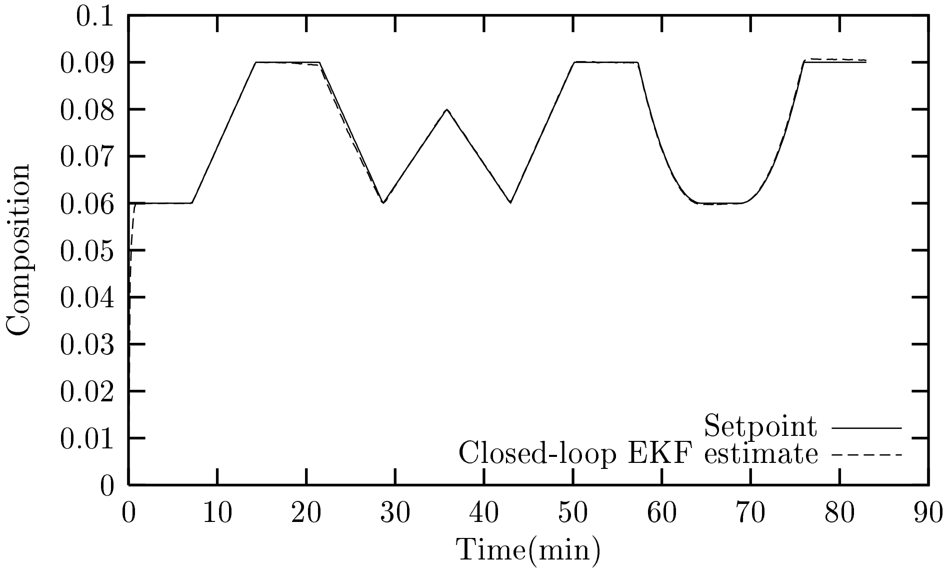

Figure 7.19: Experiment 2: Film composition

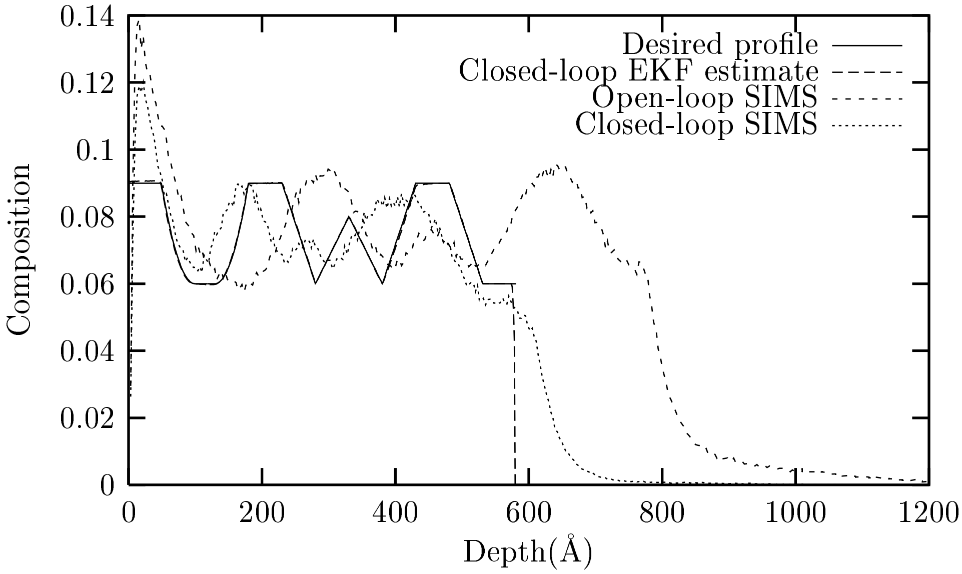

Figure 7.20: Experiment 2: Resulting films

7.3 Experiment number 3

In this experiment, the model predictive controller is tested by growing profile that has a more aggressive germanium composition. For this experiment there are no known disturbances entering the plant. Figure 7.21 shows the measured and estimated values of Δ for $\lambda = 5520\text{Å}$ for an open–loop and closed–loop run. There is very little disagreement between the ellipsometer measurements of the open–loop and the closed–loop run, suggesting that the model does a good job of predicting Δ for this wavelength and perhaps does a good job of predicting the final film qualities.

The closed–loop EKF estimate of Δ tracks the closed–loop measurement by attributing any variation between the output measurement and the output prediction as a disturbance in the substrate temperature. This temperature disturbance is shown in Figure 7.22. The observability of the temperature state disturbance during the closed–loop run is shown in Figure 7.23. The observability is quite low at the beginning of the run. However, as more data is collected the observability increases and ultimately the state disturbance becomes completely observable.

Figure 7.24 shows the open–loop and closed–loop substrate temperature set points determined by the regulator. The figure also shows the temperature response as measured by the pyrometer. The difference between the open–loop and closed–loop temperature set points is caused by the regulator correcting the temperature disturbance that was determined by the state estimator.

Figures 7.25 and 7.26 show the disilane and germane valve set points determined by the regulator during both the open–loop and the closed–loop experiment. Notice that there is no difference between the open–loop and closed–loop valve positions. Since only Δ corresponding to a large wavelength was available for feedback, the germane MFC state disturbance was not estimated. Any difference between the measured and predicted value of Δ was corrected by adjusting only the wafer temperature.

Figures 7.27 and 7.29 show the closed–loop EKF estimates of film growth rate and composition as well as the desired targets for each. The regulator drives the estimates of growth rate and composition to their specified set points while the EKF estimate of Δ converges to and tracks the plant response measured by the ellipsometer.

The resulting film profiles grown with open–loop and closed–loop control are shown in Figure 7.20. The figure shows the physical film profiles as measured by SIMS analysis. The film grown utilizing an open–loop recipe is almost identical to that which was grown utilizing feedback from the optical sensor. Although the films are close to the desired thickness, there is a 25% error between actual and desired germanium composition. This composition error goes undetected by the ellipsometer at the wavelength that was sampled. Figure 7.21 shows that the EKF estimate of

Δ converges to the measured value beautifully. The estimator pulls every nugget of information out of that signal. However, Δ at that particular wavelength ($\lambda = 5520$Å) carries little or no information about the composition of germanium at the surface of the film. Another ellipsometric parameter Δ measured at a smaller wavelength is needed to complete the controller. Δ measured at a "short" wavelength attenuates rapidly and observes the composition variation at the surface of the film. Figures 7.31 and 7.32 show the model prediction of Δ for $\lambda = 5520$Å and $\lambda = 3000$Å respectively. Notice that Δ corresponding to the "short" wavelength clearly contains information about the surface composition of germanium. Regrettably, the Verity ellipsometer used in this work is not able to resolve Ψ and Δ at wavelengths below $\lambda = 5520$Å.

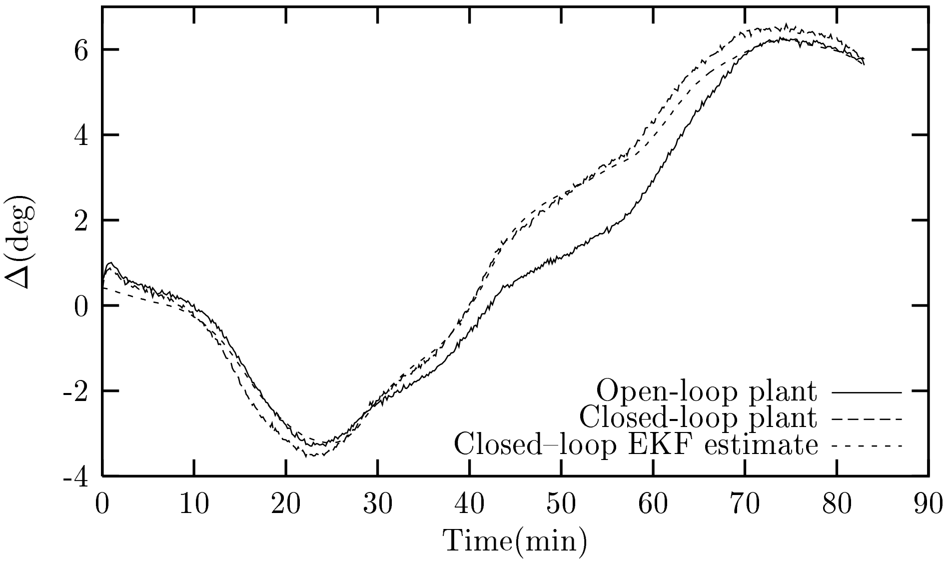

Figure 7.21: Experiment 3: Δ for $\lambda = 5520\text{Å}$

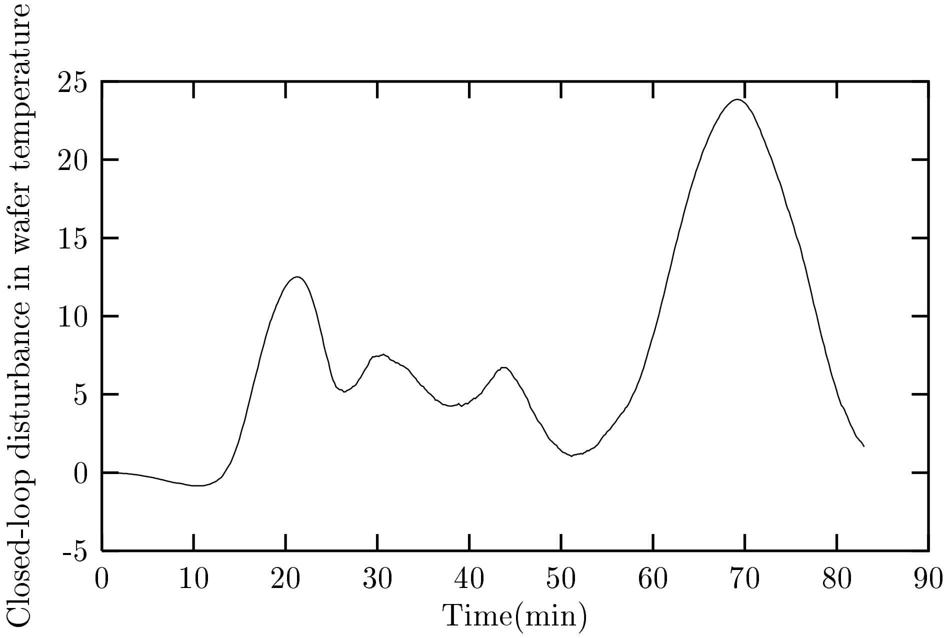

Figure 7.22: Experiment 3: State disturbance in wafer temperature

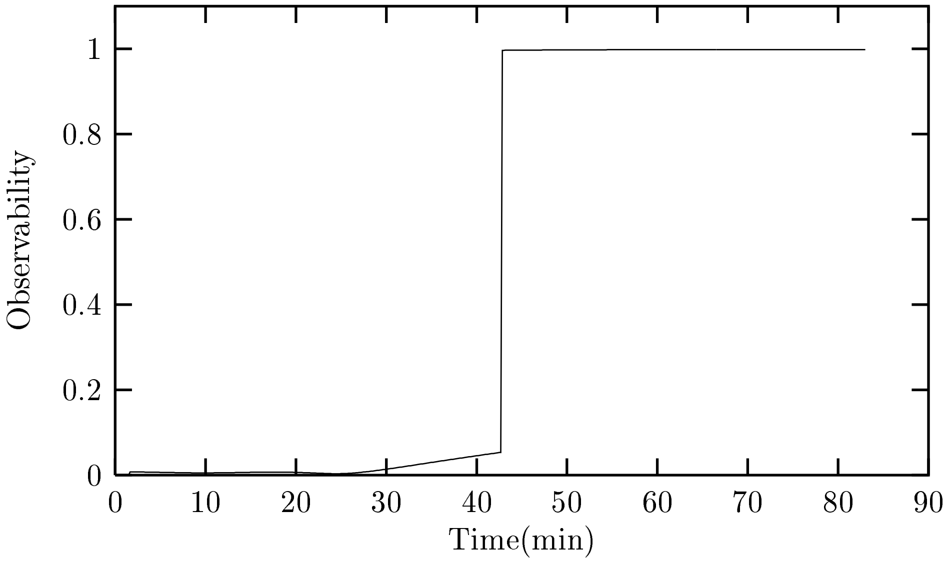

Figure 7.23: Experiment 3: Closed–loop observability of state disturbance in wafer temperature

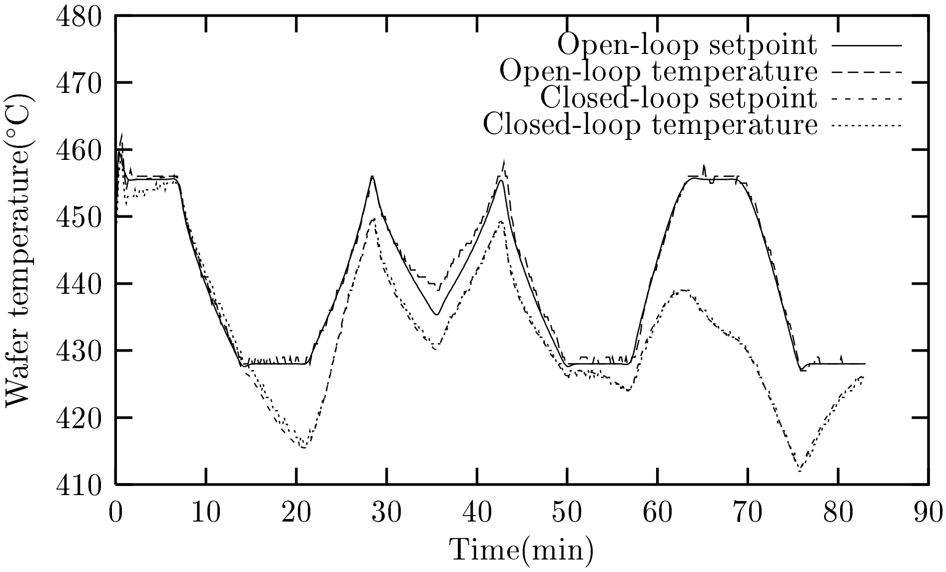

Figure 7.24: Experiment 3: Wafer temperature

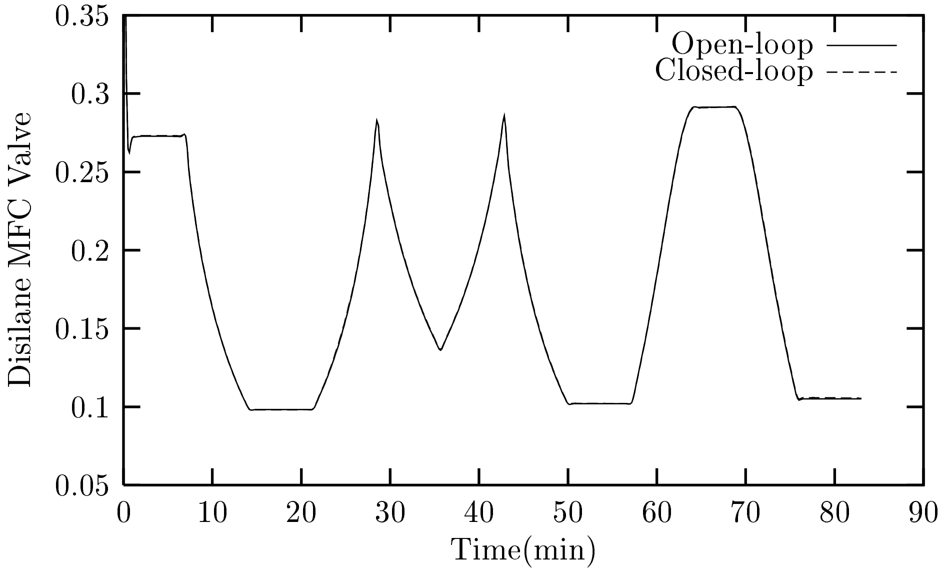

Figure 7.25: Experiment 3: Disilane MFC valve position

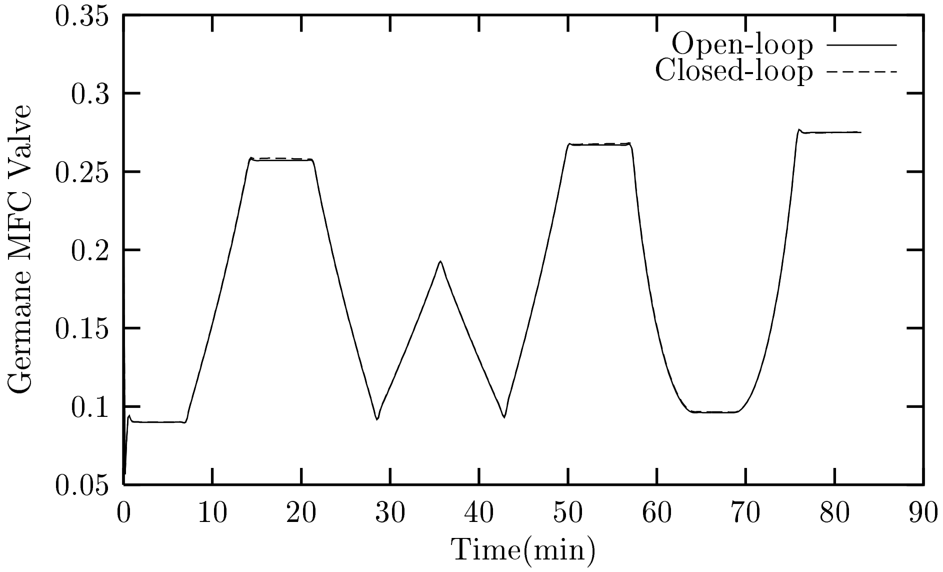

Figure 7.26: Experiment 3: Germane MFC valve position

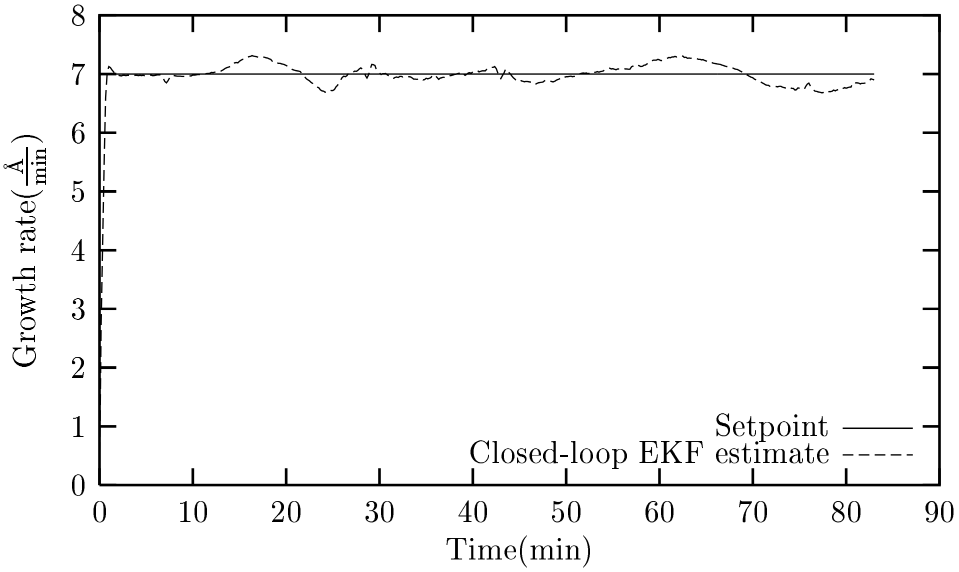

Figure 7.27: Experiment 3: Film growth rate

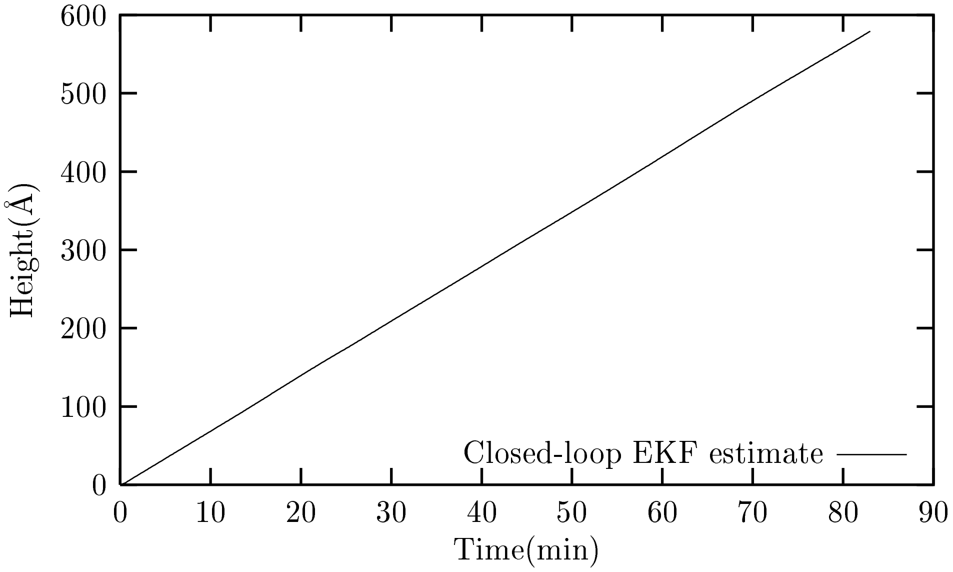

Figure 7.28: Experiment 3: Film height

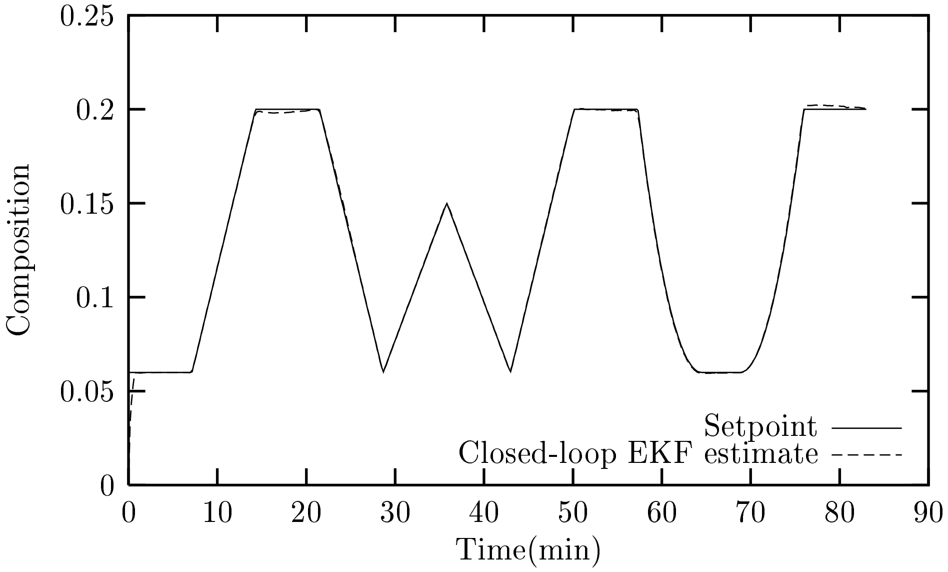

Figure 7.29: Experiment 3: Film composition

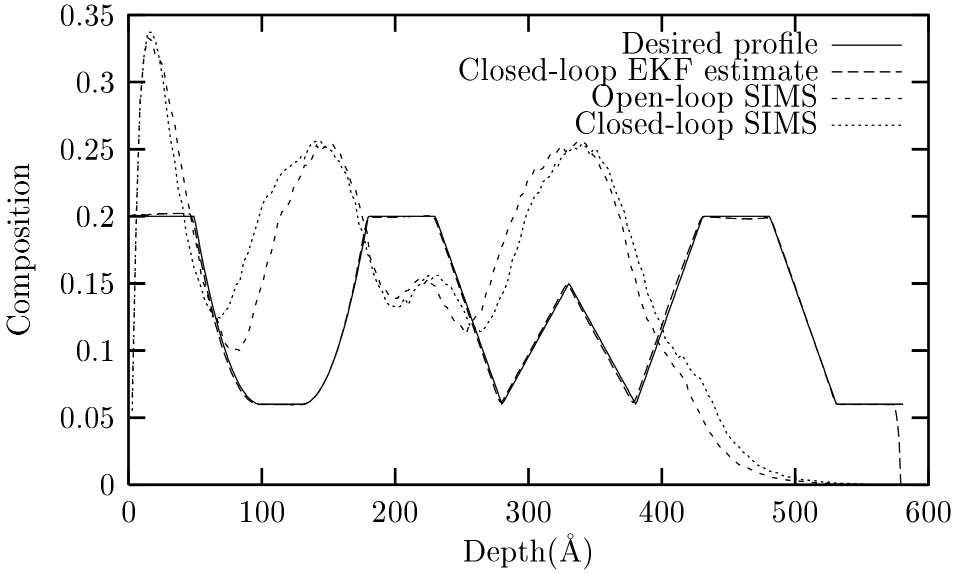

Figure 7.30: Experiment 3: Resulting films

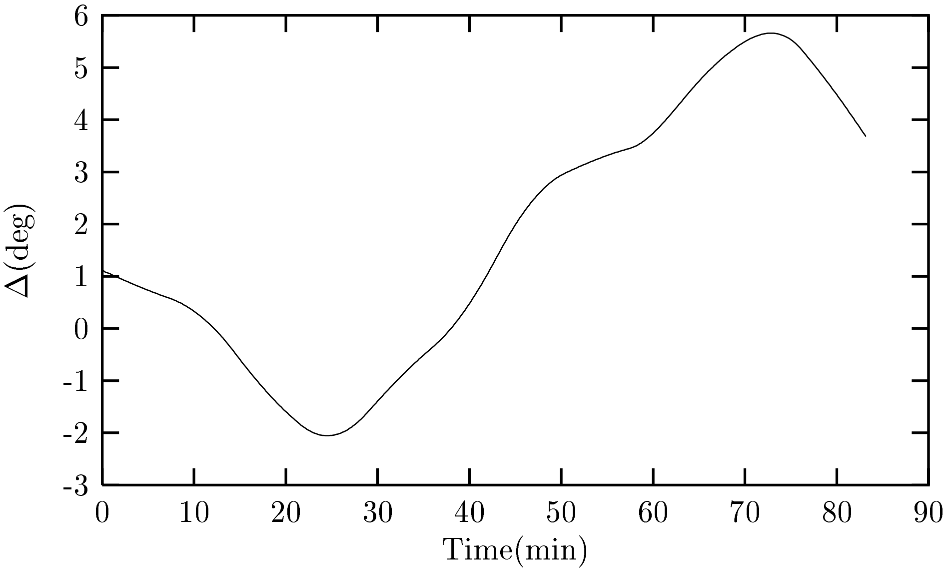

Figure 7.31: Experiment 3: Predicted Δ for $\lambda = 5520\text{Å}$

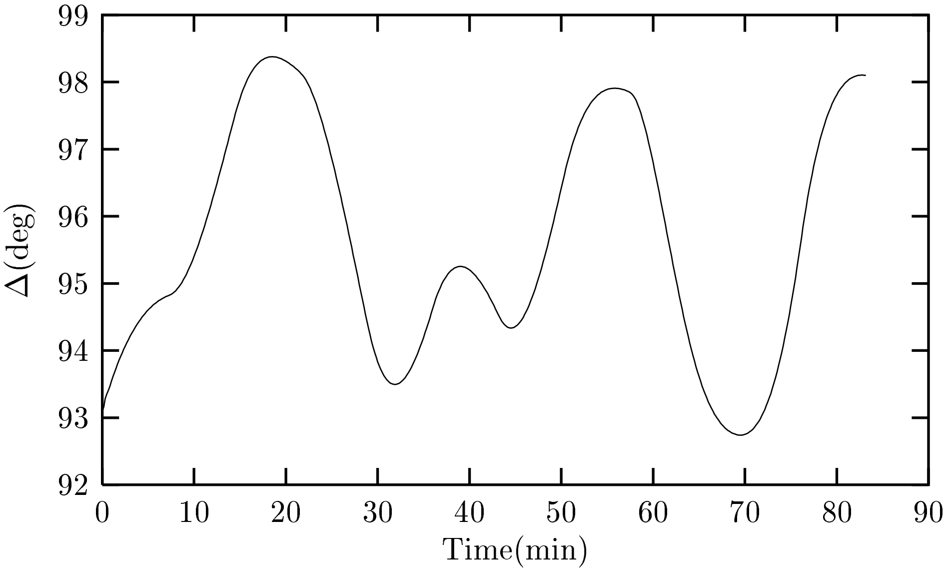

Figure 7.32: Experiment 3: Predicted Δ for $\lambda = 3000\text{Å}$

Chapter 8

Conclusions

> *He subsides. Indeed all subsides.*
>
> — Samuel Beckett, *Waiting for Godot*

As noted in the introduction, the heteroepitaxial growth of $\mathrm{Si}_{1-x}\mathrm{Ge}_x$ films on Si(100) has received much attention recently due to the possibility of band-gap engineering. Alloys of $\mathrm{Si}_{1-x}\mathrm{Ge}_x$ are of interest for the fabrication of micro-electronic devices such as heterojunction field-effect transistors(MOSFETs) and heterojunction bipolar transistors(HBTs). Chemical vapor deposition, which is the utilization of chemically reactive gases to form thin solid films, is among the most widely used film growth methods. With ultra-high vacuum chemical vapor deposition(UHVCVD) it is possible to prepare multicomponent epitaxial heterostructures with user defined composition and thickness. The quality characteristics of micro-electronic devices can be improved by improving the manufacturing process and especially its real-time control. The technical challenge of this study is thus to integrate *in situ* non-invasive optical sensors, fundamental kinetic, reactor, and sensor models with state-of-the-art estimation and model predictive control techniques in order to grow alloy films with precise control over thickness, composition, and uniformity. Precise control allows for the fabrication of novel devices with exact specifications. The individual steps required to achieve this goal are summarized below.

8.1 Model Identification of $Si_{1-x}Ge_x$ Thin Film CVD

The development of an accurate process model is the cornerstone of an effective model predictive controller. This report proposes an elementary chemical mechanism followed by a reduced mechanism that describes disilane and germane decomposition into a $Si_{1-x}Ge_x$ epitaxial film. Reaction rates are given and the model parameters are taken from data given in the literature. Species production rates are combined with a material balance around the reactor to produce the full model. The model predicts the film growth rate and germanium composition given precursor gas flow rates, substrate temperature, and reactor pressure, which are the systems' manipulated variables. The physical model is validated with experimental data.

8.2 Spectroscopic Ellipsometry for Film Thickness and Composition Monitoring

Accurate, real-time measurement of film properties is essential for feedback control. A high-speed spectral ellipsometer is employed to observe and characterize, *in situ*, events that take place at the growing film interface. Ellipsometry is an experimental method that measures the polarization transformation that occurs when a beam of polarized light is reflected from a surface. An on–line spectral ellipsometer is installed and a dynamic sensor model that characterizes the optical properties of the growing film is presented. The sensor model is integrated with the kinetic and process models that describe the reactor and predicts the ellipsometric parameters Ψ and Δ during film growth.

8.3 Development of a Time-Varying State Estimator

Solving the estimation problem is the key step in the control of $Si_{1-x}Ge_x$ chemical vapor deposition because film composition and growth rate cannot be measured directly. They must be inferred from optical measurements. It is the task of the state estimator to infer, or reconstruct the system states by balancing the contribution made by the dynamic process model with that given by the measurement.

An extended Kalman filter is developed that utilizes the process model and the sensor model and estimates uncertain system states given ellipsometric measurements. Application of state estimation theory to spectroscopic ellipsometry is a new contribution of this research. The filter provides state estimates in real time. These measurements are utilized to update the optimization problem solved by the regulator.

A state disturbance model is employed to remove steady-state offset due to the mismatch between the model prediction and reality. This mismatch or bias can arise from nonzero disturbances in process inputs, states, and outputs. For this work two state disturbances are employed. Integrating state disturbances are added to the germane MFC valve position and to the wafer temperature. The temperature disturbance accounts for the variation in the film growth rate. The disturbance added to the germane MFC valve position accounts for the variation in the film composition. Simulations are presented that demonstrate the effectiveness of the extended Kalman filter for various scenarios. The simulations also validate the particular state–disturbance model that was chosen.

8.4 Model Predictive Control Development and Implementation

A model predictive controller is presented that regulates the various reactor variables, such as precursor gas flow rates, substrate temperature, and reactor pressure, in order to grow an aggressive $\mathrm{Si}_{1-x}\mathrm{Ge}_x$ alloy film with precise control over film growth rate and composition. The essence of the MPC controller is to optimize, over the manipulated inputs, forecasts of process behavior. Utilizing the optimal estimate delivered from the state estimator at each sample time as the initial starting point for the prediction incorporates feedback into the controller. The theory for the model predictive controller presented in this work is less than ten years old and has not been implemented on the this type of batch operation.

The model predictive controller is tested by growing aggressive $\mathrm{Si}_{1-x}\mathrm{Ge}_x$ alloy composition profiles in which flow rates of several component gases and the reactor temperature are varied simultaneously in order to achieve the profile of interest. The experimental results presented in this work provide the first demonstration of feedback control using online optical film measurements to grow aggressive alloy composition profiles in which flow rates of several component gases and reactor temperature must be varied simultaneously in order to achieve the profile of interest. The films grown utilizing feedback from the optical sensor are compared to the films grown using open–loop recipes, which is the current industrial practice. These films are compared quantitatively utilizing off-line characterization techniques, such as auger spectrometry and secondary–ion–mass–spectrometry (SIMS) analysis.

In one experiment, the controller is able to successfully reject a large temperature disturbance. The ellipsometer detects the error, the state estimator correctly identifies the temperature disturbance, and the regulator compensates. A separate experiment is presented that shows the limitations of the controller, motivating the necessity of a two–wavelength optical sensor. Figure 8.1 shows the two–wavelength senor and controller that is envisioned. The ellipsometric parameter Δ that corresponds to a "short" wavelength attenuates rapidly and sees the composition variation at the surface of the film. Δ corresponding to a "long" wavelength penetrates the entire film an carries information about the film growth rate. The model is able to assist in choosing these wavelengths. The controller rejects growth rate variation by regulating the substrate temperature and rejects the composition variation by manipulating the precursor gas flow rates.

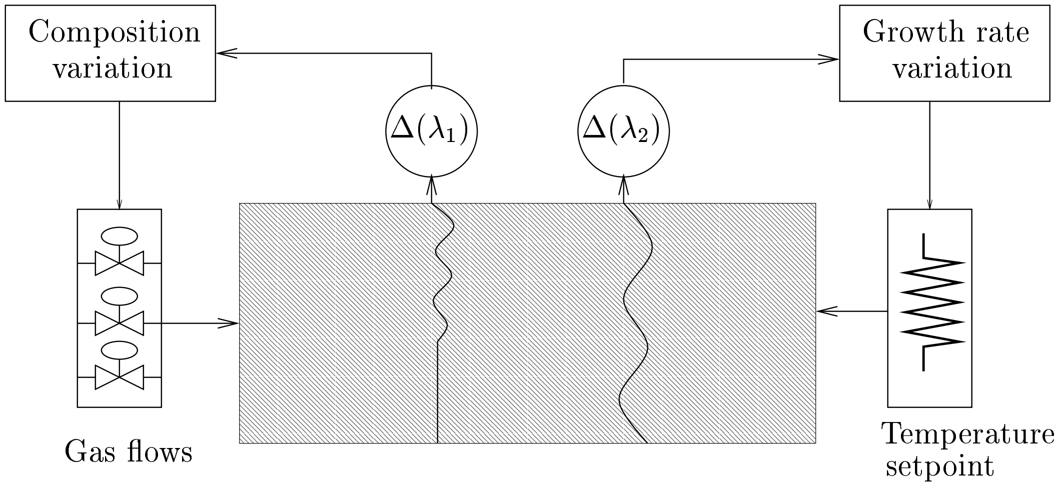

Figure 8.1: Two–wavelength sensor and controller

8.5 General Design Method

This dissertation has outlined a general design method that may be applied to other deposition or etch process with feedback coming from an optical sensor. The steps are given below.

1. A dynamic model of the process must first be developed. The model presented in this work was based on first principles. Fundamental models require a great deal of time and effort to produce. However, the intuition that a physical model provides is worth the cost of development.

2. A dynamic model of the sensor that will be used for feedback must also be developed. Again, a fundamental model was presented in this work. The fundamental model of the sensor allowed for design decisions to be made and tested before the sensor was employed.

3. A state disturbance model must be employed to remove steady–state offset due to mismatch between the model prediction and reality. Disturbances that have the most direct bearing on the regulated outputs are the most effective. For this work two state disturbances were employed. Integrating state disturbances were added to the germane MFC valve position and to the wafer temperature. The temperature disturbance accounted for the variation in the film growth rate. The disturbance added to the germane MFC valve position accounted for the variation in the film composition.

4. Based on the process model and sensor model, a time–varying, non-linear state estimator can now be employed. Given a model and a sensor measurement, the estimator can infer film growth rate and composition, which will be utilized for closed–loop control.

5. Given an estimate of growth rate and composition, a regulator can be employed. The regulator drives the estimate of the system states to desired targets. Utilizing the optimal estimate from the state–estimator introduces feedback into the controller.

8.6 Future Work

The techniques presented in this work to estimate and control $Si_{1-x}Ge_x$chemical vapor deposition are not limited to just silicon and germanium. The general design method outlined above can be applied to other deposition systems that have different chemistries, such as gallium arsenide. The estimation and control techniques may also be applied to other microelectronics processing steps, such as doping, oxidation, and etching. Fundamental models can be readily developed for these other processes. Integrating these models with on–line optical sensors and with the estimation and control algorithms presented in this work yields a complete systems framework that allows for closed–loop control of the processes.

Process control applied to microelectronics processing is in its infancy. The author is encouraged by the results presented in this work and looks forward to designing and implementing advanced control strategies to other microelectronics processes.

Appendix A

Substrate Temperature Modelling and Control

Uniform temperature distribution across the substrate during growth is necessary to grow films with uniform thickness. The temperature should be uniform during both steady-state and transient situations. Uniform temperature should also be achieved for a range of operating conditions.

A.1 Modelling and Design of New Boron Nitride Heater

The previous substrate heater consisted of 4 linear quartz-halogen lamps enclosed in a molybdenum box powered by a single phase 120 volt source. The lamps heated the substrate radiatively as shown in Figure A.1. The performance of this system was evaluated using an instrumented wafer, shown in Figure A.2, consisting of a silicon wafer with several thermocouples embedded in different positions. Figure A.3 illustrates the performance of the previous substrate heater design, which produced a center to edge wafer temperature difference of 30° C. This large difference necessitated a new heater design.

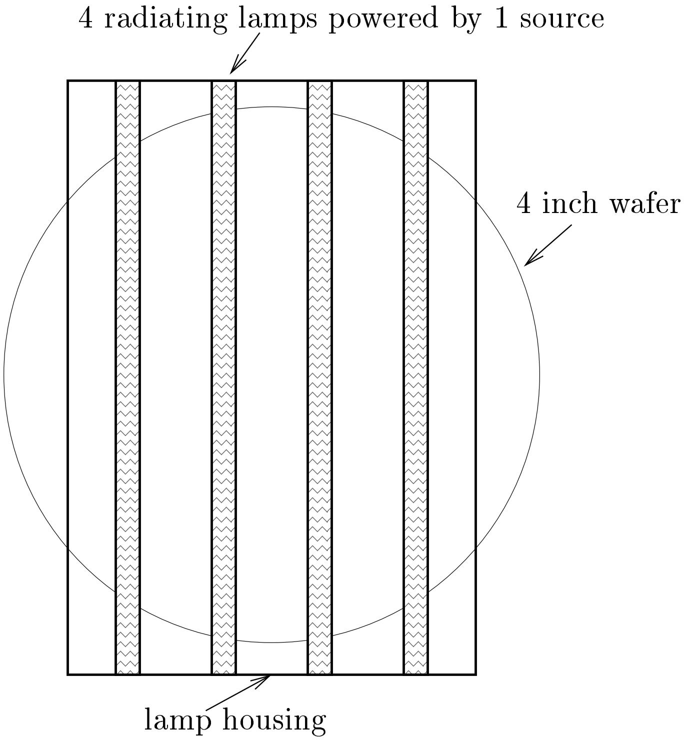

Figure A.1: Previous heater design

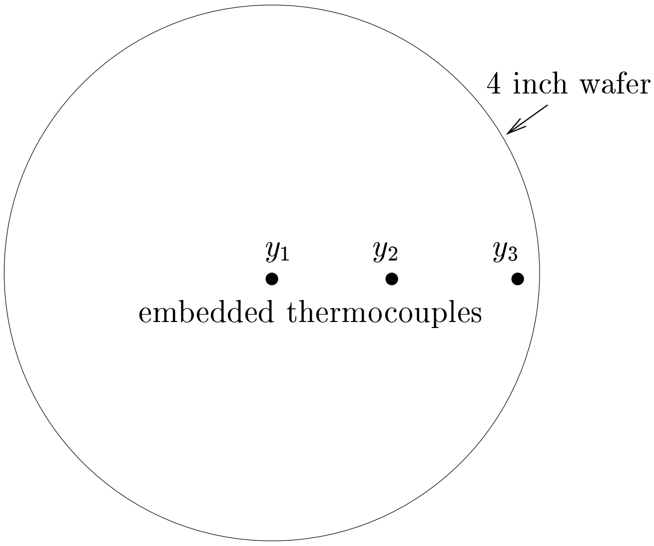

Figure A.2: Instrumented wafer used to measure substrate temperature uniformity

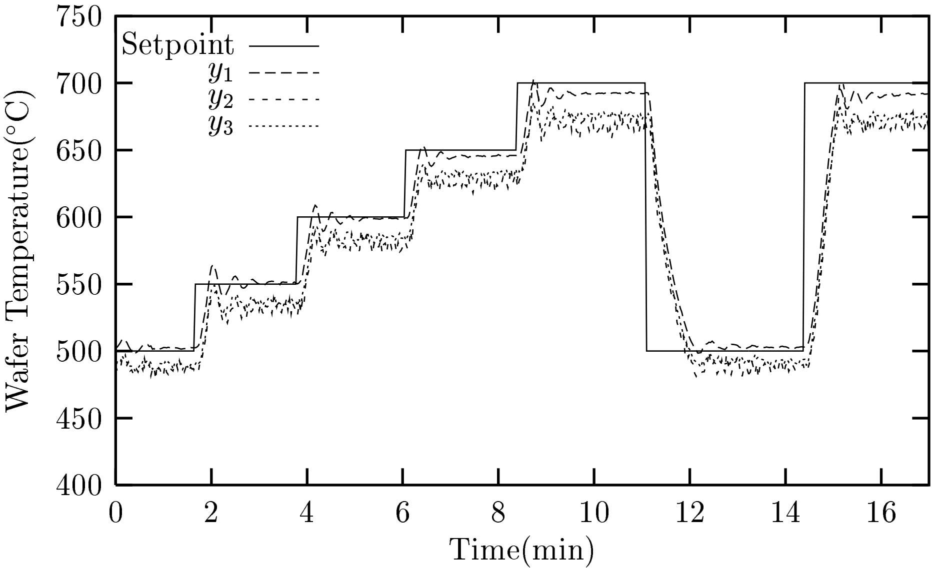

Figure A.3: Temperature profiles using previous heater design

The new design consists of two independently-controlled concentric heating zones, shown in Figure A.4. The inner zone has a 4 inch diameter and the outer zone extends 1 inch past the inner zone. This outer zone was designed to compensate for radiative losses from the edge of the wafer to the cooled reactor wall. Each zone is controlled independently via two 120 volt power sources.

An energy balance on the wafer yields, in cylindrical coordinates [13]:

$$\rho_s C_p \frac{\partial T_s}{\partial t} = \frac{1}{r}\frac{\partial}{\partial r}\left(rk\frac{\partial T_s}{\partial r}\right) + \frac{\partial}{\partial z}\left(k\frac{\partial T_s}{\partial z}\right) \tag{A.1}$$

With boundary conditions:

$$\frac{dT_s}{dr} = 0, \qquad r = 0,\ z \in [0, L]$$

$$-k\frac{dT_s}{dr} = \alpha_{\mathrm{Si}}\sigma\left(T_c^4 \epsilon_{\mathrm{w}} F_{\mathrm{e-w}} + T_{\mathrm{h}_2}^4 \epsilon_{\mathrm{h}}\left(1 - F_{\mathrm{e-w}}\right)\right) + \epsilon_{\mathrm{s}}\sigma T_s^4, \qquad r = R,\ z \in [0, L]$$

$$-k\frac{dT_s}{dz} = \sigma\left(\epsilon_{\mathrm{Si}} T_s^4 - \alpha_{\mathrm{s}}\epsilon_{\mathrm{w}} T_c^4\right), \qquad r \in [0, R],\ z = L$$

$$-k\frac{dT_s}{dz} = \sigma\left(\epsilon_{\mathrm{Si}} T_s^4 - \alpha_{\mathrm{Si}}\epsilon_{\mathrm{h}} T_{\mathrm{h}_1}^4\right), \qquad r \in [0, R],\ z = 0.$$

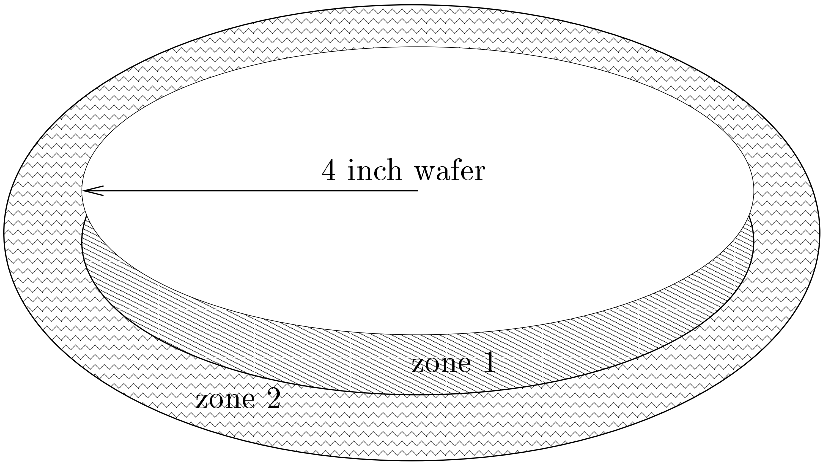

Figure A.4: New boron-nitride heater design

in which α_s and ϵ_s are the abosorptivity and emmisivity of silicon respectively, and ϵ_w and ϵ_h are the emmisivities of the reactor wall and the boron-nitride heater, respectively. The parameter F_{e-w} represents the view factor between the wafer edge and the wall. The temperatures T_{h_1} and T_{h_2} are the inner and outer heater temperatures, respectively, and T_c is the chamber wall temperature. The boundary conditions represent symmetry at the origin, flux from the wafer edge, flux from the wafer top, and flux from the wafer bottom, respectively.

Since $L \ll R$, $\frac{\partial^2 T}{\partial z^2} \approx 0$ the z boundary conditions are incorporated as generation and consumption terms in the energy balance.

$$\underbrace{\rho_s C_p \frac{\partial T_s}{\partial t}}_{\text{accumulation}} = \underbrace{\frac{1}{r}\frac{\partial}{\partial r}\left(rk\frac{\partial T_s}{\partial r}\right)}_{\text{conduction}} - \underbrace{\sigma\left(\epsilon_\mathrm{s} T_s^4 - \alpha_\mathrm{s}\epsilon_\mathrm{w} T_c^4\right)}_{\text{radiation to wall}} - \underbrace{\sigma\left(\epsilon_\mathrm{s} T_s^4 - \alpha_\mathrm{s}\epsilon_\mathrm{h} T_{\mathrm{h}_1}^4\right)}_{\text{radiation from heater 1}} \quad \text{(A.2)}$$

with boundary conditions

$$\begin{aligned} \tfrac{dT_s}{dr} &= 0, \qquad r = 0 \\ -k\tfrac{dT_s}{dr} &= \underbrace{\left(\epsilon_\mathrm{s}\sigma T_s^4 - \alpha_\mathrm{s}\sigma T_c^4 \epsilon_\mathrm{w} F_\mathrm{e-w}\right)}_{\text{edge to wall}} + \underbrace{\left(\epsilon_\mathrm{s}\sigma T_s^4 - \alpha_\mathrm{s}\sigma T_{\mathrm{h}_2}^4 \epsilon_\mathrm{h}\left(1 - F_\mathrm{e-w}\right)\right)}_{\text{edge to heater 2}}, \qquad r = R \end{aligned}$$

C_p and k for silicon are given by [16]:

$$\begin{aligned} C_p &= 1.06 \times 10^3 - \tfrac{1.04\times 10^5}{T_s} & [=] \quad \left(\frac{\mathrm{J}}{\mathrm{kg\ K}}\right) \\ k &= 50.5\left(\ln T_s\right)^2 - 734.0\left(\ln T_s\right) + 2.69 \times 10^3 & [=] \quad \left(\frac{\mathrm{W}}{\mathrm{m\ K}}\right). \end{aligned}$$

Equation A.2 was solved by the method of orthogonal collocation [69, 96]. Collocating the radial region with orthogonal polynomials yields a vector of ordinary differential equations with length equal to the number of collocation points, which was solved with the differential-algebraic equation solver DASSL [3, 17, 78].

Figure A.5 illustrates the wafer temperature profile with only the inner zone operating at 800°C. The simulation predicts a center to edge difference of 3°C, far less than the 30°C produced with the linear lamp arrangement. The wafer temperature difference can be reduced completely with both heater zones operating independently as shown in Figure A.6.

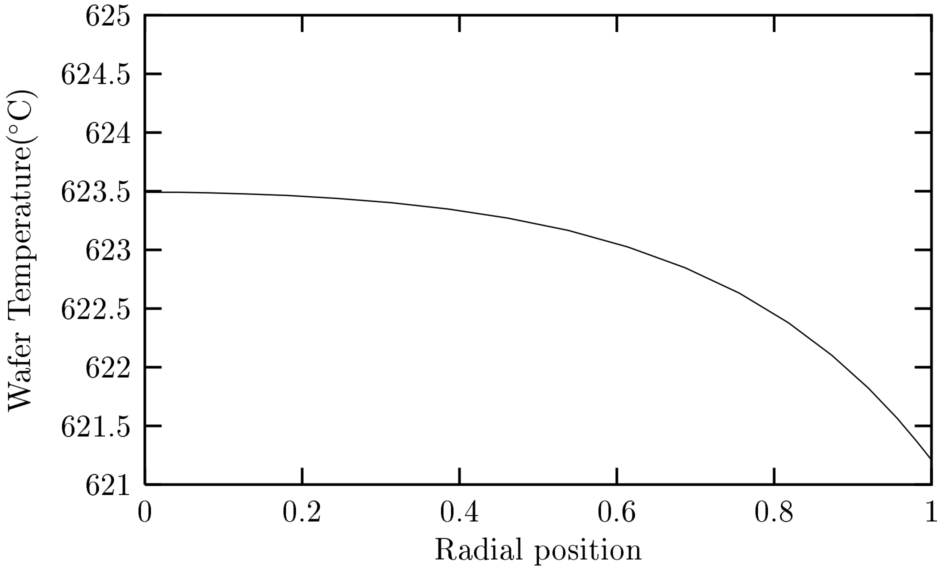

Figure A.5: Steady-state simulation with inner zone operating at $T_{\mathrm{h}_1} = 800$°C and no outer zone heating

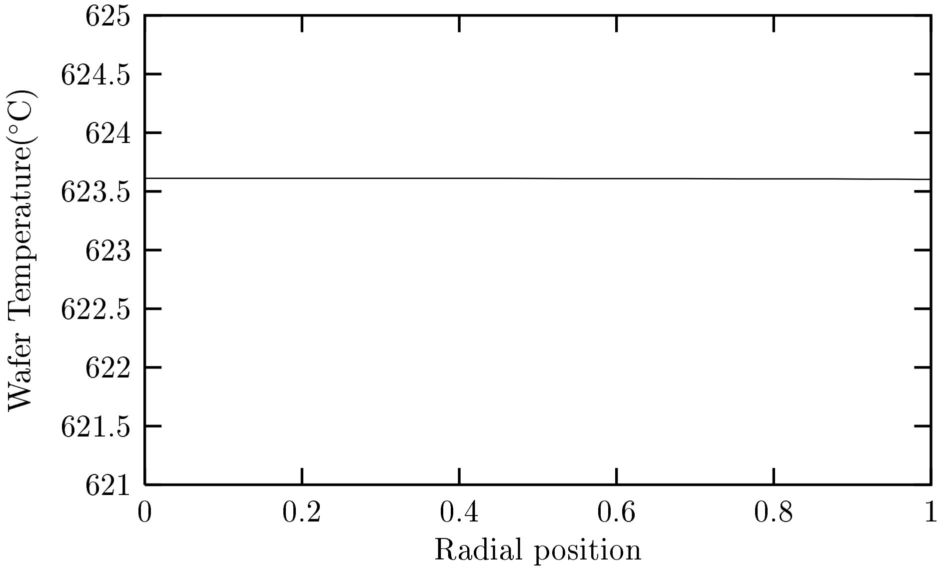

Figure A.6: Steady-state simulation with the inner zone operating at $T_{\mathrm{h}_1} = 800°\mathrm{C}$ and the outer zone operating at $T_{\mathrm{h}_2} = 700°\mathrm{C}$

A.2 Closed-Loop Wafer Temperature Control

In order to achieve uniform film growth, a model-based control strategy that regulates wafer temperature during deposition was implemented. A linear model was empirically identified correlating temperature outputs to power inputs sent through the boron-nitride heater described previously. Existing linear model predictive control (LMPC) theory based on an infinite horizon linear quadratic regulator [19, 73, 83] was implemented to regulate wafer temperature. This controller successfully reduced center to edge wafer temperature difference to less than 2–3°C. Figures A.7 and A.8 show the closed-loop regulation of wafer temperature. Offset free tracking was demonstrated over a temperature range of 550–700°C. Closed-loop response time was on the order of 40 seconds. Powers to the heaters saturated at either full on or full off after large set point changes. The model predictive control scheme handled these constraints.

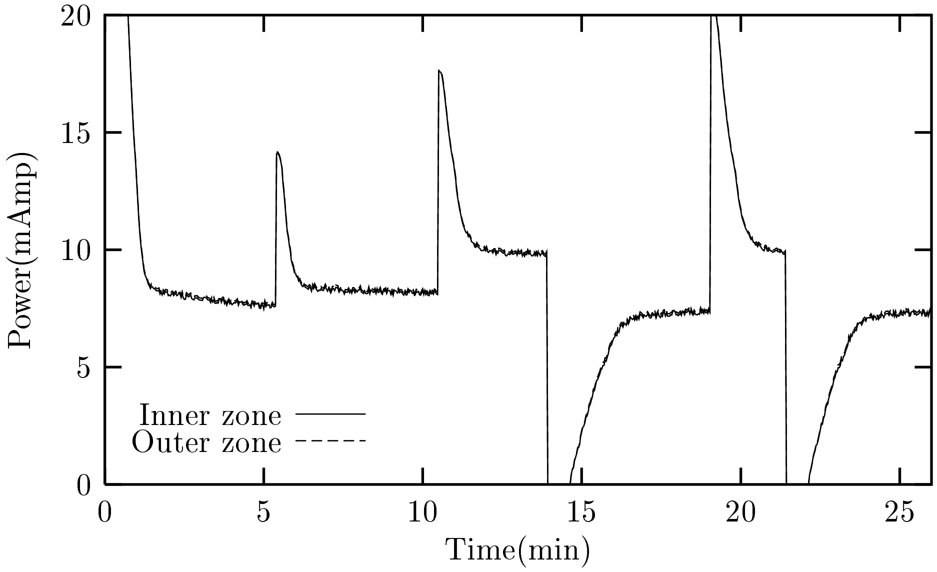

Figure A.7: Closed-loop heater powers

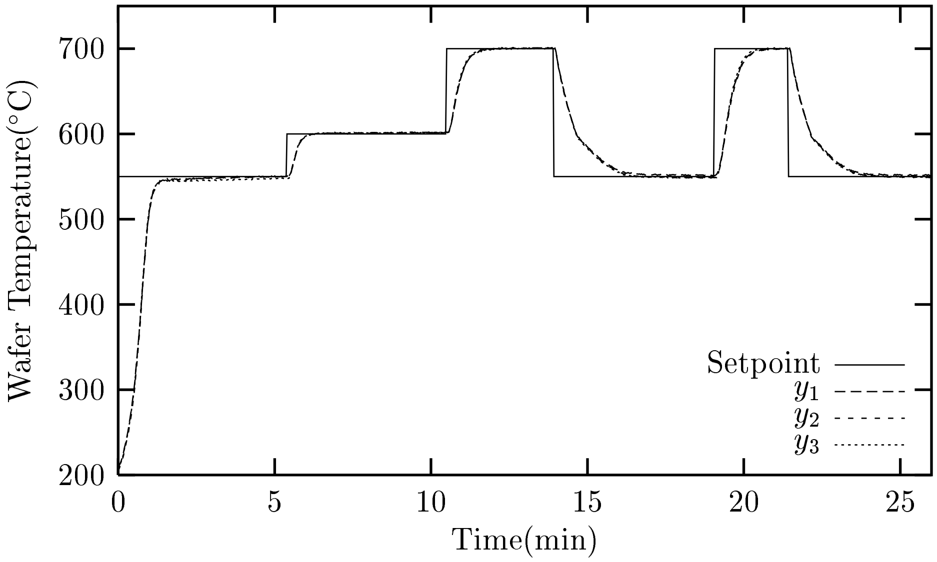

Figure A.8: Resulting closed-loop substrate temperature response

Bibliography

[1] O. Archer, E. Bigan, and B. Drevillon. Improvements of phase modulated ellipsometry. *Review of Scientific Instruments*, 60(1):65–77, 1989.

[2] R.J. Archer. *Manual on Ellipsometry.* Gaertner Scientific Corporation, Chicago, 1968.

[3] Uri N. Ascher and Linda R. Petzold. *Computer Methods for Ordinary Differential Equations and Differential-Algebraic Equations.* SIAM, Philadelphia, 1998.

[4] D.E. Aspnes. Effects of component optical activity in data reduction and calibration of rotating–analyzer ellipsometers. *J. Opt. Soc. Am.*, 64(6):812–819, 1974.

[5] D.E. Aspnes. Optimizing precision of rotating–analyzer ellipsometers. *J. Opt. Soc. Am.*, 64(5):639–646, 1974.

[6] D.E. Aspnes. Minimal–data approaches for determining outer–layer dielectric responses of films from kinetic reflectometric and ellipsometric measurements. *J. Opt. Soc. Am.*, 10(5):974–983, 1993.

[7] D.E. Aspnes. Optical approaches to determine near–surface compositions during epitaxy. *J. Vac. Sci. Technol.A.*, 14(3):960–966, 1996.

[8] D.E. Aspnes, W.E. Quinn, M.C. Tamargo, M.A.A. Pudensi, S.A. Schwarz, M.J.S.P. Brasil, R.E. Nahory, and S. Gregory. Growth of $\mathrm{Al_xGa_{1-x}As}$ parabolic quantum wells by real–time feedback control of composition. *Appl. Phys. Lett.*, 60(10):1244–1246, 1992.

[9] D.E. Aspnes and A.A. Studna. High precision scanning ellipsometer. *Applied Optics*, 14(1):220–228, 1975.

[10] R.M.A. Azzam and N.M.Bashara. *Ellipsometry and Polarized Light.* North Holland, Amsterdam, 1977.

[11] G. Bauer and W. Richter. *Optical Characterization of Epitaxial Semiconductor Layers.* Springer Verlag, 1996.

[12] John C. Bean. Silicon-based semiconductor heterostructures: Column IV bandgap engineering. *Proceedings of the IEEE*, 80(4):571–587, 1992.

[13] R. Byron Bird, Warren E. Stewart, and Edwin N. Lightfoot. *Transport Phenomena.* John Wiley & Sons, New York, 1960.

[14] Max Born and Emil Wolf. *Principles of Optics.* Cambridge University Press, Cambridge, UK, 1998.

[15] T. Bramblett, Q. Lu, T. Karasawa, M. Hasan S. Jo, and J. Greene. Si(001)2x1 gas-source molecular-beam epitaxy from Si_2H_6: Growth kinetics and boron doping. *Journal of Applied Physics*, 76(3):1884–1888, 1994.

[16] T. Breedijk, T. F. Edgar, and I. Trachtenberg. Model-based control of rapid thermal processes. In *Proceedings of the American Control Conference*, pages 907–911, Baltimore, Maryland, June 1994.

[17] K. E. Brenan, S. L. Campbell, and L. R. Petzold. *Numerical Solution of Initial-Value Problems in Differential-Algebraic Equations.* Elsevier Science Publishers, New York, 1989.

[18] A. E. Bryson and Y. Ho. *Applied Optimal Control.* Hemisphere Publishing, New York, 1975.

[19] John C. Campbell. *Modelling, Estimation, and Control of Sheet and Film Forming Processes.* PhD thesis, University of Wisconsin–Madison, 1997.

[20] Steven C. Chapra and Raymond P. Canale. *Numerical Methods for Engineers.* McGraw-Hill Book Company, New York, New York, 1988.

[21] Weize Chen, Richard Westhoff, and Rafael Reif. Determination of optical constants of strained $Si_{1-x}Ge_x$ epitaxial layers in the spectral range of 0.75–2.75 eV. *Appl. Phys. Lett.*, 71(11):1525–1527, 1997.

[22] J. Comfort and R. Reif. Chemical vapor deposition of epitaxial silicon from silane at low temperatures. *Journal of The Electrochemical Society*, 136(8):2386–2398, 1989.

[23] Brian Cunningham, Jack Chu, and Shah Akbar. Heteroepitaxial growth of ge on (100) Si by ultrahigh vacuum, chemical vapor deposition. *Appl. Phys. Lett.*, 59(27):3574–3576, 1991.

[24] E. J. Davison and H. W. Smith. Pole assignment in linear time-invariant multivariable systems with constant disturbances. *Automatica*, 7:489–498, 1971.

[25] W.M. Duncan, S.A. Henck, J.W. Kuehne, L.M. Lowenstein, and S. Maung. High–speed spectral ellipsometry for in situ diagnostics and process control. *J. Vac. Sci. Technol.B.*, 12:2779, 1994.

[26] G.R. Fowles. *Introduction to Modern Optics.* Dover, New York, 1975.

[27] P. M. Garone, J. C. Sturm, P.V. Schwartz, S. A. Schwarz, and B. J. Wilkens. Silicon vapor phase epitaxial growth catalysis by the presence of germane. *Appl. Phys. Lett.*, 56(13):1275–1277, 1990.

[28] S. Gates and C. Greenlief. Kinetics of surface reactions in very low-pressure chemical vapor deposition of Si from SiH_4. *Appl. Phys. Lett.*, 58(25):2963–2965, 1991.

[29] S. Gates, C. Greenlief, D. Beach, and P. Holbert. Deposition of silane on Si(111)-(7x7) and Si(100)-(2x1) surfaces below $500°C$. *Journal of Chemical Physics*, 92(5):3144–3153, 1990.

[30] S. Gates, C. Greenlief, S. Kulkarni, and H. Sawin. Surface reactions in Si chemical vapor deposition from silane. *J. Vac. Sci. Technol.A.*, 8(3):2965–2969, 1990.

[31] S. Gates and S. Kulkarni. Hydrogen coverage during Si growth from SiH_4 and Si_2H_6. *Appl. Phys. Lett.*, 60(1):53–55, 1992.

[32] Arthur Gelb, editor. *Applied Optimal Estimation.* The M.I.T. Press, Cambridge, Massachusetts, 1974.

[33] F. Glowacki and Y. Campidelli. Single wafer epitaxy of Si and SiGe using UHV-CVD. *Microelectronic Engineering*, 25:161–170, 1994.

[34] D.W. Greve. Growth of epitaxial germanium–silicon heterostructures by chemical vapor deposition. *Material Science and Engineering*, B18:22–51, 1993.

[35] O.S. Heavens. *Optical Properties of Thin Solid Films.* Dover, 1991.

[36] Michael A. Henson and Dale E. Seborg. *Nonlinear Process Control.* Prentice Hall PTR, Upper Saddle River, New Jersey, 1997.

[37] Francis B. Hildebrand. *Advanced Calculus for Applications.* Prentice-Hall, Inc., Englewood Cliffs, New Jersey, 2nd edition, 1976.

[38] M. Hiroi, K.Koyama, T.Tatsumi, and H. Hirayama. Intensity oscillations in reflection high-energy electron diffraction during disilane gas source molecular beam epitaxy. *Appl. Phys. Lett.*, 60(14):1723–1725, 1992.

[39] J. Holleman, A.E.T. Kuiper, and J.F. Verweij. Kinetics of low pressure chemical vapor deposition of polycrystalline germanium–silicon alloys from $\mathrm{SiH_4}$ and $\mathrm{GeH_4}$. *Journal of The Electrochemical Society*, 140(6):1717–1722, 1993.

[40] C. Hong, C. Park, and H. Kim. Structure and crystallization of low-presure chemical vapor deposited fims using $\mathrm{Si_2H_6}$ gas. *Journal of Applied Physics*, 71(11):5427–5432, 1992.

[41] D.A.O. Hope, C. Pickering, R.T. Carline, W.Y. Leong, and D.J. Robbins. Real–time control of layer thickness in LPCVD $\mathrm{Si_{0.88}Ge_{0.12}}$ HBT structures. *Thin Solid Films*, 294:18–21, 1997.

[42] Roger A. Horn and Charles R. Johnson. *Matrix Analysis.* Cambridge University Press, 1985.

[43] H. Ishii, Y. Takahashi, and J. Murota. Selective Ge deposition on Si using thermal decomposition of $\mathrm{GeH_4}$. *Appl. Phys. Lett.*, 47(8):863–865, 1985.

[44] O.L.R. Jacobs. *Introduction to Control Theory.* Oxford, New York, New York, 1993.

[45] S. Jang and R. Reif. Temperature dependence of $\mathrm{Si_{1-x}Ge_x}$ growth using very low pressure chemical vapor deposition. *Appl. Phys. Lett.*, 59(24):3162–3164, 1991.

[46] S. Jang and R. Reif. Effects of hydrogen and deposition pressure on $\mathrm{Si_{1-x}Ge_x}$ growth rate. *Appl. Phys. Lett.*, 60(6):707–709, 1992.

[47] S.M. Jang, K. Liao, and R. Reif. Chemical vapor deposition of epitaxial silicon–germanium from silane and germane. *Journal of The Electrochemical Society*, 142(10):3513–3527, 1995.

[48] Andrew H. Jazwinski. *Stochastic Processes and Filtering Theory.* Academic Press, New York, 1970.

[49] G. E. Jellison and F.A. Modine. Two channel polarization modulation ellipsometer. *Applied Optics*, 29(7):959–974, 1990.

[50] S. Kobayashi, M. Cheng, A. Kohlhase, T. Sato, J. Murota, and N. Mikoshiba. Selective germanium epitaxial growth on silicon using CVD technology with ultra–pure gases. *Journal of Crystal Growth*, 99:259–262, 1990.

[51] Y. Koide, S. Zaima, N. Ohshima, and Y. Yasuda. Growth processes in the intial stages of deposition of Ge films on (100) Si surfaces by GeH_4 source molecular beam epitaxy. *Journal of Crystal Growth*, 99:254–258, 1990.

[52] K.W. Kolasinski, W. Nessler, A. deMeijere, and E. Hasselbrink. Hydrogen adsorption on and desorption from Si: Considerations on the applicability of detailed balance. *Phys. Rev. Lett.*, 72(9):1356–1359, 1994.

[53] T.F. Kuech. Chemical vapor deposition for epitaxial growth. In H. Bernhard Pogge, editor, *Electronic Materials Chemistry*, pages 83–125. Marcel Dekker, 1996.

[54] Huibert Kwakernaak and Raphael Sivan. *Linear Optimal Control Systems.* John Wiley and Sons, New York, 1972.

[55] R. Lange, K.E. Junge, S. Zollner, S.S. Iyer, A.P. Powell, and K. Eberl. Dielectric response of strained and relaxed $Si_{1-x-y}Ge_xC_y$ alloys grown by molecular beam epitaxy on Si(001). *Journal of Applied Physics*, 80(8):4578–4586, 1996.

[56] Frank L. Lewis. *Optimal Estimation.* John Wiley and Sons, New York, 1986.

[57] C. Li, S. John, E. Quinones, and S. Banerjee. Cold wall ultrahigh vacuum chemical vapor deposition of doped and undoped Si and $Si_{1-x}Ge_x$ epitaxial films using GeH_4 and Si_2H_6. *J. Vac. Sci. Technol.A.*, A14(1):170–183, 1996.

[58] S.H. Li, P.K. Bhattacharya, R. Malik, and E. Gulari. Molecular beam epitaxial growth of $Si_{1-x}Ge_x$/ Si pseudomorphic layers using disilane and germanium. *J. Electronic Mat.*, 22(7):793–795, 1993.

[59] M. Liehr, C.M. Greenlief adn M. Offenberg, and S.R. Kasi. Equilibrium surface hydrogen coverage during silicon epitaxy using SiH_4. *J. Vac. Sci. Technol.A.*, A8(3):2960–2964, 1990.

[60] D. Lin, E.Hirshorn, T.Chiang, R.Tsu, D.Lubben, and J.Greene. Scanning tunneling microscopy studies of disilane adsorption and pyrolytic growth on Si(100)-2x1. *Phys. Rev. B*, 45:3494–3498, 1992.

[61] S.G. Lipson, H.Lipson, and D.S. Tannhauser. *Optical Physics.* Cambridge, 1995.

[62] D. Lubben, R. Tsu, T. Bramblett, and J. Greene. Mechanisms and kinetics of Si atomic layer epitaxy on Si(001)2x1 from Si_2H_6. *J. Vac. Sci. Technol.A.*, 9(6):3003–3011, 1991.

[63] R. Malik, E. Gulari, S.H. Li, and P.K. Bhattacharya. Modelling growth of $Si_{1-x}Ge_x$ epitaxial films from disilane and germanium. *Journal of Applied Physics*, 73(10):5193–5196, 1993.

[64] J.S. Meditch. *Stochastic Optimal Linear Estimation and Control.* McGraw-Hill Book Company, New York, New York, 1969.

[65] B. Meyerson. UHV/CVD growth of Si and SiGe alloys:chemistry, physics, and device applications. *Proceedings of the IEEE*, 80(10):1592–1608, 1992.

[66] B. Meyerson, K.Uram, and F. LeGoues. Cooperative growth phenomena in silicon/germanium low-temperature epitaxy. *Appl. Phys. Lett.*, 53(25):2555–2557, 1988.

[67] B.S. Meyerson. Low-tmperature silicon epitaxy by ultrahigh vacuum/chemical vapor deposition. *Appl. Phys. Lett.*, 48:797, 1986.

[68] B.S. Meyerson, B.A. Scott, and R. Tsui. Experimental and chemical kinetic modelling study of silicon CVD from monosilane and disilane. *Chemtronics*, 1:150–155, 1986.

[69] M. L. Michelsen and J. Villadsen. A convenient computational procedure for collocation constants. *The Chemical Engineering Journal*, 4:64–68, 1972.

[70] Stanley Middleman and Arthur Hochberg. *Process Engineering Analysis in Semiconductor Device Fabrication.* McGraw-Hill Book Company, New York, New York, 1993.

[71] Scott M. Mokler. Silicon and silicon-germanium gas source epitaxial growth from silicon and germanium hydrides. *Critical Reviews in Surface Chemistry*, 4(1):1–47, 1994.

[72] Kenneth R. Muske. *Linear Model Predictive Control of Chemical Processes.* PhD thesis, The University of Texas at Austin, 1995.

[73] Kenneth R. Muske and James B. Rawlings. Model predictive control with linear models. *AIChE Journal*, 39(2):262–287, 1993.

[74] B. Ning and J. Crowell. Investigation on the growth rate enhancement by Ge during SiGe alloy deposition by chemical vapor deposition. *Appl. Phys. Lett.*, 60(23):2914–2916, 1992.

[75] Edward Palik. *Handbook of optical constants of soilds.* Academic Press, Orlando, 1985.

[76] Edward Palik. *Handbook of optical constants of soilds II.* Academic Press, San Diego, 1991.

[77] Edward Palik. *Handbook of optical constants of soilds III.* Academic Press, San Diego, 1998.

[78] Linda Petzold. Differential/algebraic equations are not ODE's. *SIAM Journal on Numerical Analysis*, 3(3):367–384, September 1982.

[79] C. Pickering. Correlation of in situ ellipsometric and light scattering data of silicon–based materials with post–deposition diagnostics. *thinsolfil*, 206:275–282, 1991.

[80] C. Pickering and R.T. Carline. Dielectric function spectra of strained and relaxed $\mathrm{Si_{1-x}Ge_x}$ alloys. *japplphys*, 75(9):4642–4647, 1994.

[81] M. Racanelli and D. Greve. Low-temperature selective epitaxy by ultra-high-vacuum chemical vapor deposition from SiH_4 and GeH_4/H_2. *Appl. Phys. Lett.*, 58(19):2096–2098, 1991.

[82] M. Racanelli and D. W. Greve. Temperature dependence of $\mathrm{Si_{1-x}Ge_x}$ by ultra-high vacuum chemical vapor deposition. *Appl. Phys. Lett.*, 56(25):2524–2526, 1990.

[83] James B. Rawlings and Kenneth R. Muske. Stability of constrained receding horizon control. *IEEE Transactions on Automatic Control*, 38(10):1512–1516, October 1993.

[84] D.J. Robbins, J.L. Glasper, A.G. Cullis, and W.Y. Leong. A model for heterogeneous growth of $Si_{1-x}Ge_x$ films from hydrides. *Journal of Applied Physics*, 69(6):3729–3732, 1991.

[85] N. Russell and W. Breiland. A surface kinetics model for the growth of $\mathrm{Si_{1-x}Ge_x}$ films from SiH_4/ GeH_4 mixtures. *Journal of Applied Physics*, 73(7):3525–3530, 1993.

[86] N.M Russell and J.G. Ekerdt. Kinetics of hydrogen desorption from germanium-covered Si(100). *Surface Science*, 369(369):51–68, 1996.

[87] M.K. Sanganeria, M.C. Ozturk, G. Harris, K.E. Violette, I. Ban, C.A. Lee, and D.M. Maher. Ultrahigh vacuum rapid thermal chemical vapor deposition of epitaxial silicon onto (100) silicon. *Journal of The Electrochemical Society*, 142(11):3961–3974, 1995.

[88] E. Scheid, J.J. Pedroviejo, P. Duverneuil, M. Gueye, J. Samitier, A. El Hassani, and D. Bielle-Daspet. Silicon deposited by low pressure chemical vapour deposition from Si_2H_6:experiments, modelling and properties. *Material Science and Engineering*, B17:72–76, 1993.

[89] Pierre O.M. Scokaert and James B. Rawlings. Constrained linear quadratic regulation. *IEEE Transactions on Automatic Control*, 43(8):1163–1169, August 1998.

[90] K. Sinniah, M. Sherman, L. Lewis, W. Weinberg, J. Yates, and K. Janda. New mechanisms for hydrogen desorption from covalent surfaces: The monohydride phase on Si(100). *Phys. Rev. Lett.*, 62(5):567–570, 1989.

[91] Robert F. Stengel. *Stochastic Optimal Control: Theory and Application.* John Wiley and Sons, New York, 1986.

[92] Y. Suda, D. Lubben, T. Motooka, and J. Greene. Adsorption and thermal dissociation of disilane(Si_2H_6) on Si(100)2x1. *J. Vac. Sci. Technol.A.*, 8(1):61–67, 1990.

[93] L. Surnev and M. Tikhov. Comparative study of hydrogen adsorption on Ge(100) and Ge(111) surfaces. *Surface Science*, 138:40–50, 1994.

[94] R. Tsu, D. Lubben, T.R. Bramblett, J.E. Greene, D.S. Lin, and T.C. Chiang. Adsorption and dissociation of Si_2H_6 on Ge(001)2×1. *Surface Science*, 280:265–276, 1993.

[95] Sophie Verdonckt-Vandebroek, Emmanuel Crabbe, Bernard S. Meyerson, David L. Harame, Philip J. Restle, Johannes M.C. Stork, and Jeffrey B. Johnson. SiGe channel heterojunction p-MOSFET's. *IEEE Trans. Elec. Dev.*, 41(1):90–100, 1994.

[96] J. V. Villadsen and W. E. Stewart. Solution of boundary-value problems by orthogonal collocation. *Chemical Engineering Science*, 22:1483–1501, 1967.

[97] T.L. Vincent, P.P. Khargonekar, and F.L. Terry. An extended Kalman filter based method for fast in situ etch rate measurements. *Mat. Res. Soc. Symp. Proc.*, 406:87–93, 1996.

[98] Walter T. Welford. *Useful Optics.* The University of Chicago Press, Chicago, 1991.

[99] K. Werner, S. Butzke, S. Radelaar, and P. Balk. Evidence for non-hydrogen desorption limited growth of Si from disilane at very low temperatures in gas source molecular beam epitaxy? *Journal of Crystal Growth*, 136:338–343, 1994.

[100] T.E. Wilke, K.A. Turner, and C.G. Takoudis. Chemical vapor deposition of silicon under reduced pressure in hot-wall reactors. *Chemical Engineering Science*, 41(4):643–650, 1986.

[101] D. I. Wilson, M. Agarwal, and D.W.T. Rippin. Experiences implementing the extended Kalman filter on an industrial batch reactor. *Computers & Chemical Engineering*, 22(11):1653–1672, 1998.

[102] W.W. Woo, S.A. Svoronos, H.O. Sankur, J. Bajaj, and S.J.C. Irvine. In–situ estimation of MOCVD growth rate via a modified Kalman filter. *AIChE Journal*, 42(5):1319–1325, 1996.

[103] Y. Wu, J. Baker, P. Hamilton, and R. Nix. MIRIRS studies of the growth of Si and SiGe alloys from molecular precursors. *Surface Science*, 295:133–142, 1993.

[104] Y.M. Wu and R.M. Nix. Adsorption of hydrogen and disilane on Si(100) and SiGe surfaces. *Surface Science*, 306:59–68, 1994.

[105] G. Zhou and H. Morkoc. Si/SiGe heterostructures and devices. *Thin Solid Films*, 231:125–142, 1993.

Vita

Scott Anderson Middlebrooks, son of Bobby Lynn and Ruth Caroline Middlebrooks, was born in Galveston, Texas on October 16, 1968. When he was five his family moved to Hattiesburg, Mississippi. In May, 1986 he graduated from nearby Oak Grove High School. That fall he entered the University of Southern Mississippi. He transferred to Texas A&M University in the fall of 1988. He received the degree of Bachelor of Science in Chemical Engineering from Texas A&M in August, 1991. In the fall of 1991 he joined the research group of Roseanne Ford at the University of Virginia where he received the degree of Masters of Science in Chemical Engineering in May, 1993. He then spent nine months working as a process engineer for International Paper in Moss Point, Mississippi. He joined the research group of Dr. James B. Rawlings in January 1994 at the University of Texas at Austin. In August 1995, he moved with Dr. Rawlings from Austin to the Chemical Engineering department at the University of Wisconsin-Madison.

Permanent Address: 373 Buccaneer Drive
Hattiesburg, MS 39402

This dissertation was prepared with LaTeX 2_ε[1] by the author.

---

[1] This particular University of Wisconsin complient style was carved from The University of Texas at Austin styles as written by Dinesh Das (LaTeX 2_ε), Khe–Sing The (LaTeX), and John Eaton (LaTeX). Knives and chisels wielded by John Campbell and Rock Matthews.